CORRELATIONS BETWEEN OXIDE STRUCTURE, IRON DISTRIBUTIONS, AND ZIRCONIUM OXIDE GROWTH

by

Yan Dong

A dissertation submitted in partial fulfillment
of the requirements for the degree of
Doctor of Philosophy
(Materials Science and Engineering)
in the University of Michigan
2017

Doctoral Committee:

Associate Professor Emmanuelle Marquis, Chair
Professor Michael Atzmon
Professor Katsuyo Thornton
Professor Lumin Wang

Acknowledgement

The work in this dissertation would not have been possible without the help, support, and dedication of a number of people. First and foremost, I would like to express my most sincere gratitude and appreciation to my advisor Professor Emmanuelle Marquis for her guidance, support and help in every aspect of my study including experimental design, academic paper writing, presentation skills and future career development. She keeps me inspired by her positive perspectives, great passion for academic researches and hard-working attitude.

I am also grateful to my dissertation committee members, Professor Lumin Wang, Professor Michael Atzmon, and Professor Katsuyo Thornton for all of their help during my PhD. Whether it's been through a class I've taken with them, a joint collaboration we've had, or questions they've thought important for me to address, they have shaped my dissertation immensely and I would like to thank them for it. I would also like to thank our collaborator, Professor Arthur Motta at Pennsylvania State University. I have learned a great deal from the collaboration and I would like to thank him for the opportunity and his help along the way.

I would especially like to thank each and every one of my lab mates for their tremendous help, and more importantly their friendships, during these past few years. I would like to specially thank Dr. Yimeng Chen, for being my first lab mentor, for getting me familiarized with atom

probe, FIB, TEM, etc., and for driving me to Toledo in the first two semesters when I did not have a car. Whenever I have questions, I have always been able to rely on our post-doctoral researchers Dr. Mukesh Bachhav, Dr. Allen Hunter, Dr. Lan Yao and Dr. Vicente Araullo-Peters for their generous help and mentorship. I would also like to thank Reshma Mathew, Ellen Solomon, Kevin Fisher, Peng-Wei Chu, Adam McFarland, Craig Shaner, Elaina Anderson, Talia Barth, Kathleen Chou, and Li-Jen Yu, for always being there to help when I've needed them. Many thanks to the EMAL staff members Kai Sun, Haiping Sun, Ying Qi, for the instruments training and invaluable help.

On a more personal note, I would like to thank my parents for their unconditional love and support. I would also like to thank Kenneth Cheng for everything he has done for me. I would not have been able to succeed if it had not been for his encouragement and dedication. Additionally, I would like to thank all the friends who have stayed with me during this long journey. I cherish all the fun and friendship with you.

Table of Contents

List of Acronyms

APT	Atom probe tomography
BWR	Boiling water reactor
EBSD	Backscattered electron diffraction
EDS	Energy dispersive spectroscopy
EELS	Electron energy loss spectroscopy
FIB	Focused ion beam
HAADF	High angle annular dark field
HVE	Hot vacuum extraction
ICF	Image compression factor
ICP-OES	Inductively Coupled Plasma Optical Emission Spectroscopy
PWR	Pressurized water reactor
SEM	Scanning electron microscopy
SPPs	Second phase particles/precipitates
TEM	Transmission electron microscopy
XRD	X-ray diffraction

List of Tables

List of Figures

CHAPTER 1

Introduction

1.1 Background

Zirconium based alloys are widely used as nuclear fuel cladding materials in nuclear power plants because of their low thermal neutron capture cross-section, adequate mechanical behavior and good high temperature corrosion resistance. Yet waterside corrosion and its associated hydrogen pickup remain a major issue for utilizing these alloys in severe fuel duty conditions, especially in pressurized water reactors. Alloys with greater corrosion resistance are required to ensure continued fuel efficiency and reliability as burn-up increases.

1.2 Current Work

This thesis work is supported by DOE Office of Nuclear Energy's Nuclear Energy University Programs. The aim of this work is to contribute to the current understanding on how alloying additions in zirconium alloys could affect the oxidation behaviors, especially the onset of

oxide breakaway, and therefore to inform future design of alloys with greater corrosion resistance.

The work conducted in this project is divided into two parts:

1 – Characterization of oxide scales (including oxide phases, interface morphologies, oxide grain texture, etc.) as a function of corrosion time for different Zr alloys exhibiting very different corrosion rates.

2 – Analysis of solute distributions within the alloys, oxides, and sub-oxide phases.

1.3 Thesis Structure

Chapter 2 introduces the current understanding on the oxidation behaviors of zirconium-based alloys and the open questions that remain to be solved. Alloys and experimental methods utilized in this thesis work are described in Chapter 3. Chapter 4 introduces the composition measurements and solute distributions in the alloys far away from the oxide scale. The analyses of the corroded alloys are presented in Chapter 5-7, which are adapted from published work [1, 2] and a manuscript in preparation. Finally, a summary of the main findings, proposed mechanisms, and suggested future research directions are presented in Chapter 8.

CHAPTER 2

Uniform Corrosion of Zirconium-based Alloys: Literature Review

2.1 Introduction

Zirconium-based alloys are widely used as nuclear fuel cladding materials in nuclear power plants because they possess a unique combination of low thermal neutron capture cross-section, adequate mechanical properties, and reasonable corrosion resistance [3].

Zirconium started to be considered as a promising candidate for fuel cladding in 1950s despite a rough start. Early evaluations indicated that the zirconium samples absorbed too many thermal neutrons, but it was later found that the evaluated "pure" zirconium samples contained 1-5% hafnium (Hf). Consequently, the removal of Hf produced a material of extremely low cross-section and rendered zirconium transparent to neutrons [4].

The oxidation rate of zirconium alloys can be evaluated by measuring the increase in weight due to oxygen incorporation as a function of exposure time. For pure zirconium, the corrosion rate evolves during the corrosion process; it decreases over time as the oxide scale forming on

the surface creates a layer protecting the underlying metal from further oxidation. However, once the passive layer grows to a critical thickness, it may suddenly lose its protective nature, and the corrosion enters a second stage termed “breakaway” or “transition” [4-6]. After transition, the corrosion rate increases dramatically (Figure 2.1) and the oxide layer tends to flake causing the claddings to fail. Because the corrosion rate of pure zirconium in water was too high and exhibited too great a degree of variability for reliable industrial applications, efforts focused on adding alloying additions to delay transition and minimize overall corrosion rate.

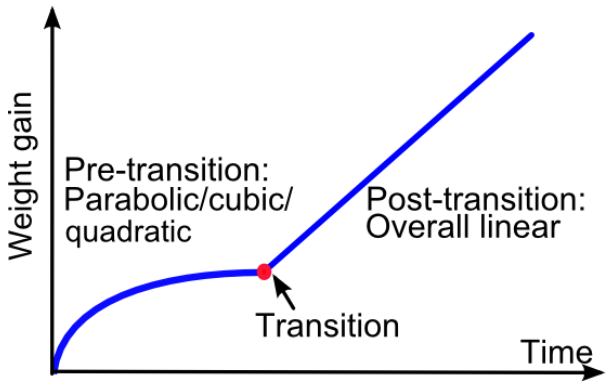

Figure 2.1: A schematic corrosion curve showing oxidation kinetics of pure zirconium

Alloy development proceeded in two alloy systems: Zr-Sn alloys and Zr-Nb alloys or a combination Zr-Sn-Nb. By combining these alloying elements with other elements such as Cr, Fe and Ni, several commercial alloys were developed, including Zircaloys [7, 8], and more recently, ZIRLO [9] and M5 [10], all of which exhibited reasonable corrosion resistance.

Uniform waterside corrosion is one of the principal in-reactor degradation mechanisms of Zr alloys in pressurized water reactor (PWR) environments and is one of the limiting factors of fuel rod design. The intense radiation environment within the core accelerates the degradation of the components by increasing the rate of corrosion and hydride formation [12]. Since economic factors have driven the operation of nuclear power plants to higher coolant temperatures, longer operating cycles, and longer in-reactor residence times, it is of great importance to the future of the nuclear industry to improve the corrosion resistance of Zr-based alloys.

The key to further improvements in corrosion resistance is sought through a more fundamental understanding of the effects of alloying elements and microstructure on the corrosion process. Extensive work has already been performed in this area and has led to fruitful results. A few mechanistic models have been proposed that could explain some of the differences in the corrosion behaviors of different alloys. However, no agreement has been reached on how each factor affects the corrosion process and the current understanding of the corrosion mechanisms is neither clear nor complete.

The goal of this review is to discuss the current state of research on corrosion of zirconium-based alloys. The physical metallurgy of zirconium and its alloys is first introduced, followed by a summary of microstructures of "as-received" materials (section 2.2). The microstructural characterization and microanalysis of oxidized zirconium alloys are discussed in section 2.3.

Then, existing theories of oxidation including oxidation kinetics and breakaway mechanisms are discussed (section 2.4) and linked to alloy microstructures and oxidation kinetics. The impacts of lithiated water, hydrogen absorption, or irradiation effect on corrosion are not included in this review.

2.2 Physical Metallurgy

2.2.1 Pure Zirconium

The equilibrium phase (α) of pure zirconium at room temperature exhibits a hexagonal close packed (HCP) crystal structure (Figure 2.2). The lattice parameters are a = 0.323 nm and c = 0.515 nm, resulting in a c/a ratio of 1.593 [11], which is slightly lower than the ideal ratio of 1.633. Since the zirconium has a hexagonal crystal structure, the physical properties will be different depending on the specific crystallographic orientation.

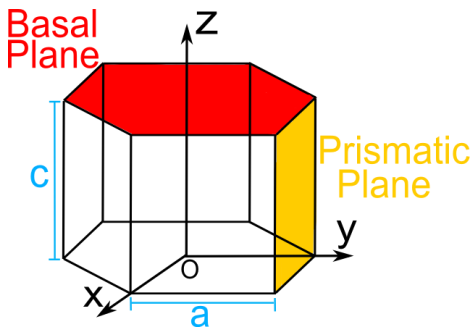

Figure 2.2: Schematic illustration of HCP crystal lattice.

The melting point of pure Zirconium is 1850 ºC and it undergoes a phase transformation at 865 ºC from the low temperature α phase (HCP) to a body centered cubic β phase [12]. By adding different alloying elements, the transition temperature changes and a two phase region is introduced.

2.2.2 Alloying Additions and Common Zirconium Alloys

Alloying elements have been added to the pure zirconium to achieve higher corrosion resistance and mechanical strength. The choice of alloying elements had been done mostly through trial and error, which often requires a tradeoff between corrosion behavior and mechanical properties. In addition to metallurgical considerations, the alloying elements need to have relatively low neutron absorption cross sections. Common alloying elements in zirconium alloys are oxygen (O) tin (Sn), niobium (Nb), iron (Fe), chromium (Cr), and nickel (Ni) [13]. O is added to increase the yield strength. It acts as an α stabilizer, expanding the α region on the phase diagram by forming an interstitial solid solution [14]. Sn is also an α-stabilizer [15]. It was originally added to mitigate the deleterious effects of nitrogen. Adding Sn to zirconium alloys also improves the alloy mechanical properties. Fe, Cr and Ni give a eutectoid decomposition of the β phase, therefore known as "β-eutectoids" [16-18]. The solubility of these alloying elements in α-Zr is low (0.04 at. % for Cr at 860 ºC and 0.02 at %

for Fe at 800 ºC) so that they tend to form intermetallic precipitates distributed within the α-Zr matrix [19]. Nb is a β stabilizer. It forms a complete substitutional solid solution in the high temperature β phase. At temperatures below 600 ºC, only α-Zr and β-Nb precipitates are thermodynamically stable [20].

Table 2.1: Compositions (wt. %) of common zirconium alloys.

Alloys	Sn	Nb	Fe	Cr	Ni	O
Zircaloy-2	1.2-1.7	-	0.07-0.2	0.05-0.15	0.03-0.08	0.10-0.14
Zircaloy-4	1.2-1.7	-	0.18-0.24	0.07-0.13	-	0.10-0.14
Zr-2.5Nb	-	2.4-2.8	<0.15	<0.02	<0.007	0.09-0.13
ZIRLO®	0.9-1.2	0.9-1.13	0.1	-	-	0.09-0.15
E635	1.0-1.3	1.0	0.35-0.4	-	-	0.10-0.14
M5 (Zr-1Nb)	-	0.8-1.2	0.015-0.06	-	-	<0.1
E110	-	0.95-1.05	0.006-0.012	-	-	0.10-0.14

Two primary families of zirconium-based alloys have been developed. Zircaloys (Zr-Sn alloys) were introduced into light water reactors in the 1960s [11, 13], only Zircaloy-2, with Ni additions and Zircaloy-4, with no Ni but a Fe level higher than Zircaloy-2, are still widely in use today. Zircaloy-2 is mainly used in boiling water reactors (BWRs) and Zircaloy-4 is used in pressurized water reactors (PWRs). Zircaloy-4 was developed to mitigate the high Ni-induced hydrogen uptake of Zircaloy-2 that was too high for PWRs. The second alloy family, Zr-Nb alloys, was mostly developed in Russia and Canada and contains 1% or 2.5% niobium and lower amounts of other elements. Other advanced alloys with higher corrosion resistance have also been developed, including low-tin Zircaloy-4 [21], ZIRLO® [9], and M5 [10]. The compositions of common zirconium-based alloys are summarized in Table 2.1.

2.2.3 Material Processing and Resultant Microstructure

The general processing procedures for industrial alloys are as follows [11, 12]:

- Hot forging in the β range.
- Quenching from homogeneous β phase (β-quenching).
- Forging, rolling, or extrusion at intermediate temperatures (between α and β) to expected shape.
- A series of cold rolling steps followed by annealing treatments at intermediate temperatures to restore ductility.

Hot forging in the β phase range leads to the dissolution of all pre-existing precipitates. On cooling, the β phase transforms into the α phase. The transformation is either martensitic or bainitic depending on the cooling rate. For Zircaloys, cooling rates faster than 1000 $K \cdot s^{-1}$ leads to the martensite structure, while the needle-shaped structure is absent if cooling rate are less than 0.5 $K \cdot s^{-1}$. Between these two cooling rate limits, the β to α phase transformation yields a Widmanstätten microstructure that may present either a basket-weave or parallel-plate structures [22]. The basket-weave structure appears as relatively short plates intersecting each other within the parent β-grains. The parallel-plate structure is composed of long plates and grows from the parent β-grain boundaries [23]. Impurities such as C, Si, P

and insoluble impurities act as nucleation sites for α phase, which will likely change the metallographic structure to a basket-weave structure [23, 24].

The annealing treatments restore ductility and the final microstructure consists of equiaxed α-Zr grains and second phase particles both at the grain boundaries and within the grains [25]. The annealing temperature can be reduced to obtain a stress-relief state where complete recrystallization is avoided. Elongated grains and high density of dislocations and fine precipitates give better mechanical properties [26]. The martensitic product of the β→α transformation in Zr-2.5%Nb alloy contains fine twins. Upon tempering, niobium-rich precipitates are nucleated at twin boundaries, α grain boundaries, and homogeneously within the matrix. Upon extended tempering, the niobium content of the precipitates increases until the composition of the β-Nb phase is reached [27]. When quenching is performed in the (α+β) region, two phases form upon annealing: α-Zr and Nb rich β-Zr. β-Zr forms a network around elongated α-Zr grains. Subsequent heat treatment is required to decompose the β-Zr precipitates into α-Zr and discrete β-Nb particles [28, 29].

A cumulative annealing parameter (CAP) is defined to quantify the integrated effects of different processing and heat treatment procedures [30]. The expression for CAP can be written as:

$$CAP = A_i = \sum t_i \exp(-\frac{Q}{RT_i}) \qquad \text{Equation 2.1}$$

where Q_i is the activation energy and t_i and T_i are the time and temperature of each step i. The CAP can vary by several orders of magnitude. The CAP offers a unified way to compare the materials treated at different temperatures and time periods and is a metric to evaluate the sizes second phase particles. However, the CAP fails to describe the effect of cold working on the microstructures and is only valid for treatments that are conducted after the last β quench [30].

2.2.4 Intermetallic Precipitates

Most of the alloying additions are more soluble in the high temperature β-Zr phase (>865 ºC for pure zirconium) than that in α-Zr. The solubility of Fe, Cr, Ni and even Nb is very low in α-Zr. Therefore, these elements tend to form various types of second phase particles (SPPs) depending on the composition and the processing and heat treatment history [28, 31-40]. The intermetallic phases that are observed in common zirconium alloys as well as their basic properties are summarized in Table 2.2.

Other types of intermetallic precipitates have also been observed such as $Zr(Nb, Fe, Cr)_2$ [38], $(Zr, Nb)_2Fe$ [39]and Zr_3Fe [40]. The composition, size, and distribution of the SPPs play an important role on the corrosion resistance of the zirconium alloys [41].

Table 2.2: Most common types of SPPs observed in zirconium-based alloys

SPPs	Crystal Structure	Alloys (that the SPPs are observed)
$ZrFe_2$	Cubic	Zircaloy-4
$ZrCr_2$	Hexagonal and Cubic	Zircaloy-4, Zircaloy-2
Zr2Ni	Tetragonal	Zircaloy-2
$Zr(Fe, Cr)_2$	Hexagonal and Cubic	Zircaloy-4, Zircaloy-2, ZIRLO®
Zr2(Fe, Ni)	Tetragonal	Zircaloy-2
$Zr(Nb, Fe)_2$	Hexagonal	ZIRLO®, M5, E635
β-Nb	Cubic	ZIRLO®, M5

2.3 Microstructural Characterization of Oxidized Zirconium Alloys

2.3.1 Zirconium-Oxygen Phase Diagram

Both α-Zr (hcp) and β-Zr (bcc) are able to dissolve high amounts of oxygen. The oxygen solubility of β-Zr reaches as high as 10.5 at. % oxygen at high temperatures, while the maximum solubility of α-Zr reaches values as high as 28.6 - 35 at. % oxygen (Figure 2.3). At 500 °C, the solubility of oxygen in α-Zr is around 29 at. % [14]. Adding more oxygen leads to the transformation to zirconium dioxide (ZrO_2), the only thermodynamically stable oxide of zirconium. ZrO_2 can manifest itself into three different crystal structures depending on temperature, stress state, and other factors. The crystal structures and symmetry information are listed in Table 2.3.

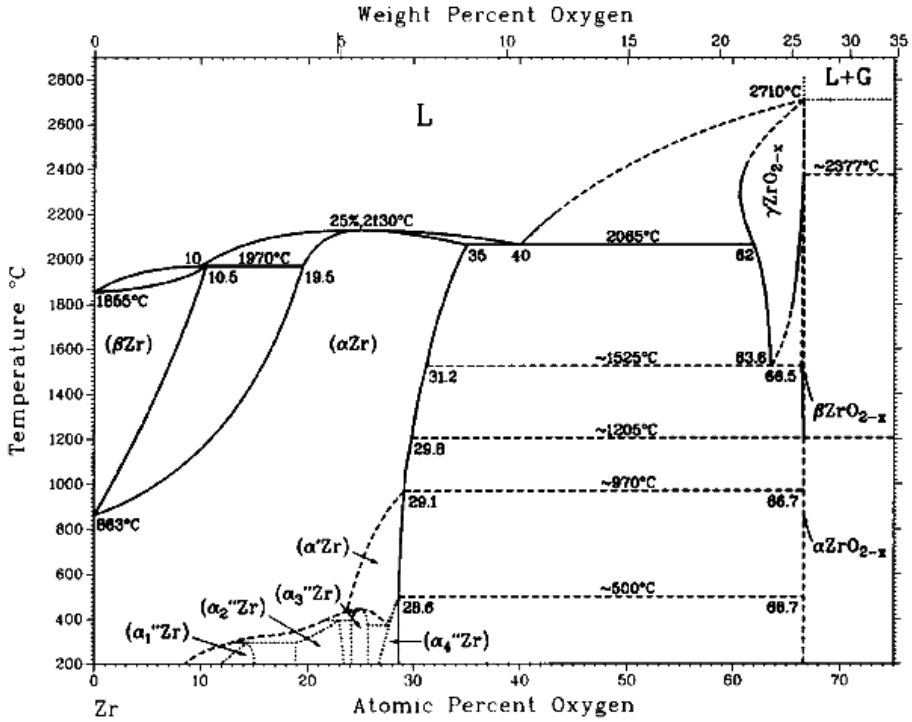

Figure 2.3: Phase diagram for the Zr-O system. Reproduced from [14] with permission.

Table 2.3: Structure information of three types of ZrO_2

Phase	Composition	Crystal Structure	Space group
α- ZrO_2 (or m-ZrO_2)	ZrO_2	Monoclinic	$P2_1/c$
β-ZrO_2 (or t-ZrO_2)	ZrO_2	Tetragonal	$P4_2/nmc$
γ-ZrO_2 (or c-ZrO_2)	ZrO_{2-x}	Cubic	Fmm

Additional metastable ordered phases in Zr are predicted in for lower oxygen content and lower temperatures (α', α_1', α_2' in Figure 2.3) [14], representing various arrangements of oxygen on the interstitial sites of α-Zr. The ordered phase (Zr_6O, Zr_3O, and Zr_2O) have been identified by Arroyave et al. [42] and Puchala et al. [43, 44]. In addition, Puchala et al. also

identified a stable δ-ZrO phase [43, 44]. The δ-ZrO structure is equivalent to the high-pressure ω-Zr phase but has interstitial oxygen ordering.

2.3.2 ZrO_2 Oxide

The ZrO_2 oxide layer formed on top of an alloy substrate consists of monoclinic ZrO_2 while the presence of tetragonal ZrO_2 has been occasionally observed [45]. In the pre-transition regime, the oxide layer is compact and contains very few pores and micro-cracks. Most grains in pre-transition oxide are columnar, while equiaxed grains appear after the transition occurs. The post-transition oxides exhibit higher porosity, more interconnected cracks, and sometimes a periodic multilayer structure. The periodicity in oxide grains morphology has been correlated to the multiple transitions in the corrosion curves of Zr-Sn based alloys. The observed oxide microstructures are now discussed.

1) Monoclinic ZrO_2 and tetragonal ZrO_2

Monoclinic ZrO_2 (m-ZrO_2) is the predominant phase within the ZrO_2 oxide layer. Tetragonal ZrO_2 (t-ZrO_2) is considered metastable at the temperatures where oxidation process takes place [46]. Since t-ZrO_2 can be stabilized by compressive stresses [47, 48] and small grain sizes [49-51], t-ZrO_2 grains are mostly present near the metal-oxide interface, where the conditions of compressive stress or small grains are likely to be sufficed [45, 52-55].

Observing t-ZrO_2 is difficult using normal imaging techniques such as transmission electron microscopy (TEM) because t-ZrO_2 tends to de-stabilize and transform into monoclinic once free surfaces are created during sample preparation [46]. Therefore, it is probable that the volume fractions of t-ZrO_2 reported in the literature are lower than the actual values. Although the measured volume fractions of t-ZrO_2 are not accurate and vary a lot from alloy to alloy, they are consistent with one another in that the metal-oxide interface possesses higher amount of t-ZrO_2. Results from synchrotron experiments show highest fraction of t-ZrO_2 near the metal interface and gradually decreasing levels away from the interface [56]. This is in agreement with results from Raman spectroscopy [57-59] according to which compressive stresses within the oxide decrease and lead to destabilization of tetragonal phases as corrosion proceeds. Furthermore, lower valence state elements in the oxide are also suggested to play a role in stabilizing the metastable ZrO_2 phase [60].

2) Grain morphology and texture

Both columnar and equiaxed grains have been observed in the oxide layers. Beie et al. [61] observed only columnar grains in the pre-transition oxides but equiaxed grains in the outer part of the oxide layer have been reported by other researchers [62, 63]. Further investigation showed that the tetragonal phase is associated with small equiaxed grains while the columnar grains are mostly monoclinic [62, 63]. In the post-transition oxides, fine equiaxed grains are observed both at the outer part of the oxide and at the oxide-metal interface [64]. The

nucleation of small equiaxed grains at the interface is speculated to indicate the loss of oxide protectiveness [62-64].

The columnar grains grow perpendicular to the oxide-metal interface [65]. The sizes of columnar grains are reported to range from 5 to 90 nm in width and 100 to 500 nm in length [61, 63, 65-67]. Most equiaxed grains are observed on the oxide surface and near the cracks and incorporated second phase particles [45, 65], where the stress level is high enough to stabilize the tetragonal equiaxed grains. The equiaxed grains are much smaller, usually around 5-50 nm in diameter [63, 68].

A few epitaxial orientation relationships have been observed previously through TEM diffraction analysis and high resolution imaging [66, 69, 70] while other work reported the formation of stress favored fiber texture with the $(\bar{3}01)$ to $(\bar{5}01)$ planes aligned parallel to the sample surface [56, 63, 71-73]. Li et al. proposed a two-stage growth model to rationalize the discrepancy in oxide grain orientation [74]. The model speculated that the oxide texture formation process consists of an oxide nucleation process driven by substrate lattice matching and a stress-controlled selective grain growth process.

3) Pores and cracks

Pre-transition oxides are dense with very few pores and cracks. The cracks in pre-transition oxides are small in size and oriented parallel with interface [61, 75]. In post-transition oxides,

however, both lateral and vertical cracks are observed. The vertical cracks can extend from the oxide surface to the middle part of the oxide layer or even to the oxide-metal interface [76, 77]. The cracks aligned laterally and vertically can form an interconnected network to promote the oxidation process [78, 79].

2.3.3 Suboxide at Metal-Oxide Interface

A number of lower stoichiometry oxide phases have been reported in the literature using various techniques including synchrotron radiation diffraction, electron diffraction, electron energy loss spectroscopy (EELS), X-ray energy dispersive spectroscopy (EDS), and atom probe tomography (APT).

The presence of an equiatomic ZrO phase was reported in the early literature in oxidized Zircaloy-2 and was observed by TEM and selected area diffraction [80]. It exhibits a square diffraction pattern with interplanar spacing commensurate with the reported value for the ZrO crystal cell [80]. Recent work using APT, EDS and EELS analysis also demonstrated the presence of a ZrO intermediate layer [67-71]. Further studies of the oxide-metal interface in pre- and post-transition alloys have demonstrated that the ZrO phase is only present in alloys that are at pre-transition stage and disappears after transition [52, 81].

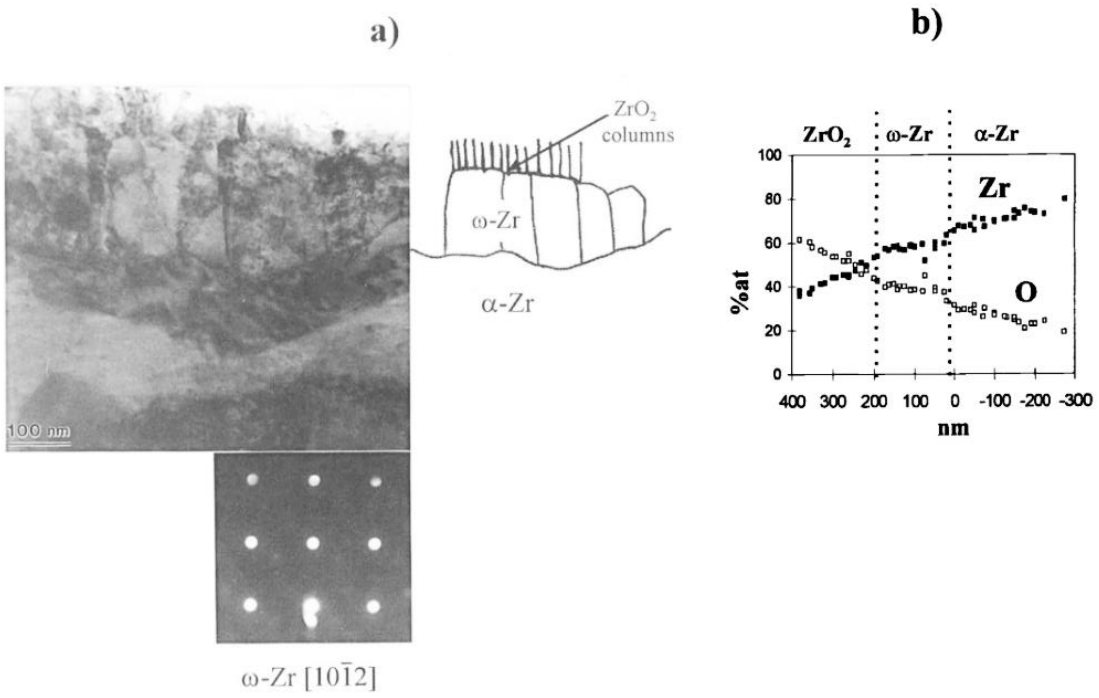

Figure 2.4: TEM examination of a cross-section of the metal-oxide: (a) bright field image exhibiting a band-like region composed of grains bigger than ZrO_2 columns and micro-diffraction pattern of one of the grains; (b) EDX line-scans analyses across the interface. Reproduced from [82] with permission.

Yilmazbayhan et al. reported the formation of wide rectangular grains ahead of the oxide/metal interfaces [63]. These grains showed different properties from the alloy bulk and were identified as the Zr_3O phase [56, 73]. Bossis et al. reported a band-like region, named ω-Zr, present at the interface. The ω-Zr exhibited a hexagonal structure and contained around 40 at. % of oxygen [83] (Figure 2.4). Bossis explained that the oxygen enriched phase may result from some particular local conditions including oxygen content and compressive stresses.

2.3.4 Oxide-Metal Interface Morphologies

SEM examination of interface morphologies after removing the metal beneath demonstrated a "cauliflower-like" interface [84-86]. The interface is reported to go through three stages to form the cauliflower shaped morphology: a diffuse structure, a needle structure and finally a cauliflower structure [85]. The development from a diffuse structure, via a needle structure, to the cauliflower structure is shared by all types of alloys despite the different alloy composition. The process of developing the cauliflower structure will be slower for alloys with higher corrosion resistance [85, 87].

The oxide-metal interfaces show strong variations of morphology. As seen in Figure 2.5, the Zr-0.4Fe-0.2Cr (wt. %) exhibits a homogeneous oxide layer with little thickness variation while the oxide layer formed on Zr-0.5Cr (wt. %) shows extensive lateral cracking and a wavy interface. The oxide layer formed on pure zirconium after breakaway shows an uneven interface with dendrites of oxide advancing into the metal and extensive cracking [73]. The roughness of the interface has been correlated with the corrosion resistance: the alloys with rougher oxide-metal interface are suggested to have higher corrosion rate [76, 84-86, 88].

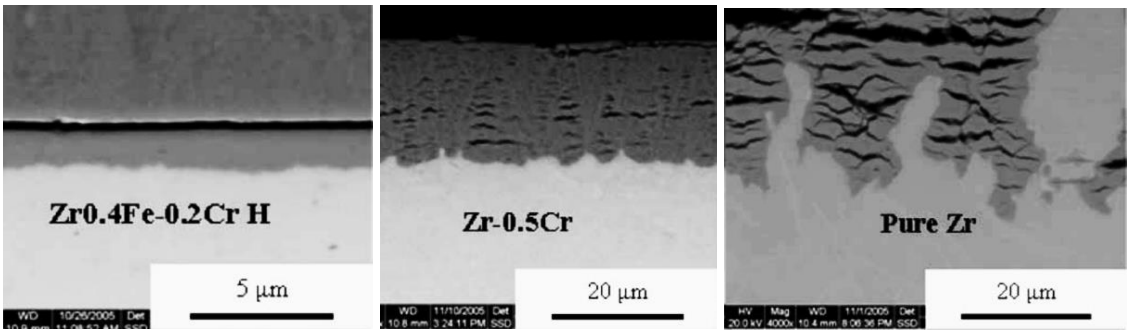

Figure 2.5: Interface morphologies of three zirconium-based alloys. The three alloys exhibited different oxidation kinetics. The images are reproduced from [73] with permission.

2.3.5 Second Phase Particles in the Oxide

Oxidation of second phase particles (SPPs) is not simultaneous with that of the matrix due to the differences in composition and structures between the SPPs and matrix. Electrochemical investigation showed that the intermetallic particles act as cathodes relative to the Zr matrix [41]. It is agreed that the SPPs are incorporated into the oxide as metallic precipitates and will not be oxidized until they are completely surrounded by the oxide [89-97] .

$Zr(Fe,Cr)_2$ is the one of the most prevalent precipitates found in Zircaloys. Upon oxidation, both Fe and Cr in $Zr(Fe,Cr)_2$ diffuse out from the precipitates into the oxide. Fe diffuses faster than Cr so that the Fe/Cr ratio is decreasing with the oxidation time [53, 89, 92, 93]. Precipitation of Fe into Fe rich precipitates with bcc structures has been observed at the SPP/matrix interface. When SPPs are further oxidized, the bcc Fe-rich precipitate will

disappear and leave a depleted zone of Fe near the oxidized SPP [90, 92], indicating the dissolution of Fe into the ZrO_2.

The oxidized SPPs have been found to consist of small nano-crystallites in the early stage of oxidation [92, 93] and later become amorphous. Transformation of oxide grains around SPPs from columnar to equiaxed has also been reported [89]. Oxidation of Zr_2(Fe, Ni) is similar, with Fe diffusing faster than Ni into the oxide [95, 98, 99]. The Zr_2(Fe, Ni) precipitates are oxidized faster than $Zr(Fe,Cr)_2$ [98]. Other precipitates like β-Nb particles in ZIRLO® and Zr-Nb alloys are also found to be oxidized later than the matrix [91, 100, 101]. Once oxidized, the β-Nb particles become amorphous and then dissolve in to the oxide matrix [100].

2.4 Oxidation Mechanisms and Kinetics

2.4.1 Uniform Corrosion and Nodular Corrosion

The corrosion of zirconium alloys, under most conditions, lead to growth of a uniform oxide layer. This type of corrosion is known as uniform corrosion. Another type of corrosion mode is called nodular corrosion, where alloys suffer from highly localized rapid oxidation associated with the formation of white oxide spots is observed [12, 13, 102, 103]. Intermetallic precipitates, zirconium hydrides, and solute depleted regions are the preferential

sites for the formation of nodules [103]. Once nucleated, the oxide nodules are observed to grow in size but remain the same in number [12, 13].

2.4.2 Uniform Corrosion Kinetics

The oxidation of Zr occurs at the metal-oxide interface, accompanied by the reduction of H_2O at the oxide-water interface (Figure 2.6). The oxide growth is implemented by diffusion of both oxygen ions and electrons through the oxide layer. The oxidation kinetics is mostly determined by the ionic transport of oxygen.

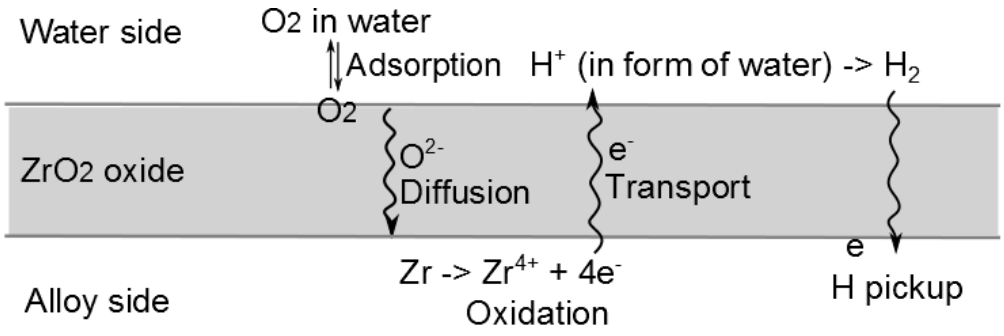

Figure 2.6: Schematic illustration of oxidation process in zirconium alloys.

The oxidation kinetics of uniform corrosion can be described by [12, 104-106]:

$$(\Delta m) = kt^n \qquad \text{(Equation 2.2)}$$

where Δm is the weight gain that reflects the thickness of protective oxide, t is corrosion time, k is a constant that can be calculated by the activation energy of rate-controlling process, and

n is also a constant. The value of n is a constant that determines whether the oxidation kinetics follows linear, parabolic, or else.

The weight gain measured during the corrosion may exhibit four types of distinct behaviors as summarized in Figure 2.7. Some alloys lose protectiveness during the corrosion process, going from a saturating behavior to almost linear kinetics; a few resist for longer times or even remain in the protective regime to the end of autoclave testing. For most zirconium alloys, two regimes that follow different oxidation kinetics can be identified on the weight-gain versus time curve.

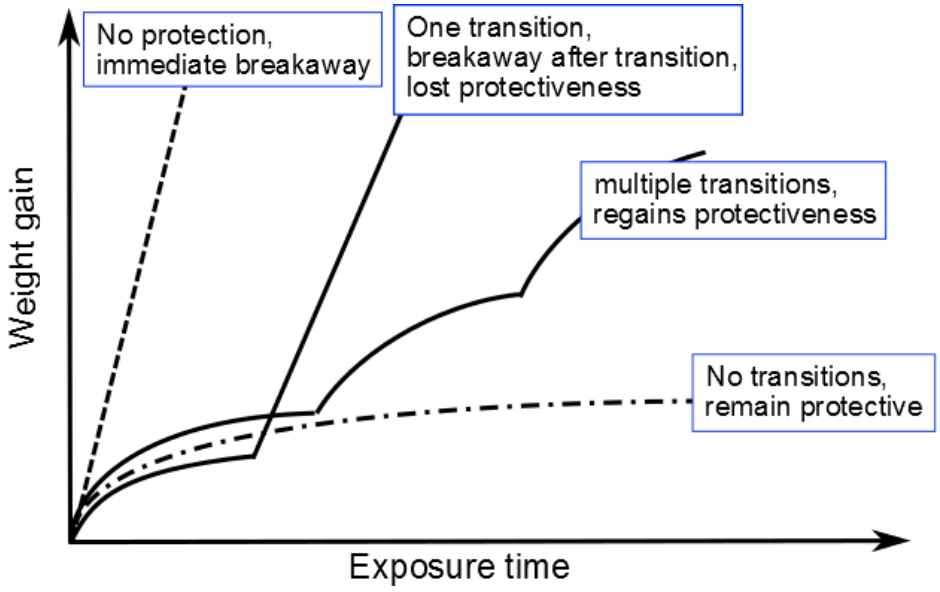

Figure 2.7: Schematic weight gain versus exposure time curve of various types of corrosion kinetics observed in the autoclave corrosion studies of the pure zirconium and zirconium-based alloys.

1) Pre-transition Regime

In the pre-transition regime, the oxidation kinetics follows a parabolic (n=1/2), cubic (n=1/3) or quadratic (n=1/4) relation. If bulk diffusion of oxygen ions is assumed to be the rate-controlling process, the kinetics of oxide growth are parabolic (n=0.5) [12, 107, 108]. Change in oxidation kinetics from parabolic to cubic or quadratic are commonly observed. The deviations are due to contributions from other factors that could affect the diffusion of oxygen ions. Yoo et al. [108] proposed a quantitative model that could explain the transition of kinetics from parabolic to cubic by taking into account the stress gradient throughout the oxide layer. Dawson [106] suggested that the formation of lateral micro-cracks near the metal-oxide interface can act as a diffusion barrier and hence slow down the oxidation. Other proposed contributing factors are the evolution of oxide grains (both grain size and grain shape) and the incorporated precipitates [109-112].

For Zircaloys, the value of n usually ranges from 0.25 to 0.6 depending on the corrosion conditions [112]. Previous studies [113] suggested that the oxidation kinetics tend to follow a cubic law at lower temperature while a parabolic law at higher temperature. The temperature at which the change occurs is approximately corresponds to the phase transformation temperature of ZrO_2 (900 to 1000 °C). Hence it is likely that the change in the n value with temperature is related to the oxide phase transformation [113].

2) Post-transition Regime

Once the thickness of the oxide layer reaches a critical value (usually around 2 um), the kinetic transition occurs with an accelerated kinetics. The oxidation kinetics in this post-transition stage follows a near linear relation in general [109, 114, 115], but the specific modes of transition are different for Zircaloys and Zr-Nb alloys. In Zircaloys, a sharp increase in oxidation rate is observed, followed by a cyclic series of corrosion periods repeating pre-transition growth [114, 116, 117]. Overall, the cyclic growth rate follows a linear dependence. The cycles in the post-transition regime are suggested to represent the growth of successive oxide layers after the formation of the first pre-transition oxide. The transition of oxide growth in Zr-Nb alloys is gentler with no evidence of sharp or clearly defined transition point. The oxidation kinetics exhibits a steady and continuous change from cubic (or parabolic) to linear [118]. Various studies reported that Zr-Nb alloys with proper heat treatment possess higher corrosion resistance compared to Zircaloys [118-123].

2.4.3 Breakaway Mechanisms

The transition in the oxide kinetics in which oxide cannot regain its protectiveness is also known as “breakaway” or “breakdown”. Many studies have attempted to explain the mechanisms for the onset of breakaway transition.

One hypothesis is known as the “mechanical breakaway” [73, 124-127]. The cause for the breakaway is claimed to be built-up stresses in the oxide due to the volume difference between the metal and the oxide. Cracks, especially those vertical to the oxide-metal interface, can be induced once the stress level exceeds a critical value. The formation of a crack network can promote oxidation and contribute to the transition. However care must be exercised as cracks observed in TEM images may also be created during sample preparation. The interconnected porosity induced by oxide phase transformation from t-ZrO_2 to m-ZrO_2 was also speculated to be responsible for the onset of transition [128-130]. The micro-pores and cracks are assumed to be generated by twinning during the phase transformation. The explanation is based upon the observation of a decreasing amount of t-ZrO_2 in the oxide after the transition [45, 131, 132]. Still, there is a lack of experimental support to justify the proposed mechanism, and there is currently no universally accepted explanation for how the transition occurs.

2.5 Microstructural Factors Affecting Alloy Corrosion Resistance

2.5.1 Structures of Oxide Scale

As mentioned in the previous section, the oxide layer grows by the transport of both ionic oxygen and electron transport through the barrier oxide layer. The microstructures of the

protective oxide could determine the diffusion process and hence affect the corrosion kinetics. The oxide grain morphology and texture have also been proven to affect the corrosion behavior. Various studies have reported that oxides in alloys with high corrosion resistance contain a larger portion of columnar grains [68, 86, 133]. Both X-ray diffraction (XRD) [132] and transmission electron microscopy (TEM) [63] analyses have demonstrated a correlation between improved corrosion resistance and stronger oxide texture that contains a higher a portion of well-aligned columnar grains. Previous study by Garner et al. suggested that tetragonal ZrO_2 forms first and then transforms to favorably oriented monoclinic grains [134]. The transformation of columnar grains to equiaxed grains is also proposed to be related with the oxidation transition [45, 53, 65, 89]. The higher corrosion resistance of columnar grains could be explained by smaller oxide grain boundary area associated with columnar grains or by stronger intergranular cohesion between columnar grains [61, 68].

The metal-oxide interface could also affect the corrosion resistance. The suboxide layers formed at the interface could consume the oxygen that could have been used to form ZrO_2 and then slow down the oxide layer advance, or could affect the corrosion kinetics by changing the oxygen concentration gradient across the oxide layer. The presence of these layers have been shown to correlate with the kinetics of oxidation in that the suboxide layers which present in pre-transition oxides will disappear after the transition [52]. The width of the

suboxide layer inversely correlates with the corrosion kinetics [2, 56, 135]. However, it is still unclear whether the thicker suboxide is a cause or an effect of the oxide advance slowdown.

2.5.2 Second Phase Particles (SPPs)

The size and distribution of SPPs are very important contributing factors that could affect the corrosion resistance of zirconium alloys. However, the combination of the size and distribution that leads to optimized corrosion resistance remains controversial. The design of size and distribution of SPPs should be considered differently from alloy to alloy. For corrosion in PWR or water autoclave, most studies showed that precipitates with smaller sizes would result in higher oxidation rate [89, 136-139]. Tejland et al. recently reported that the incorporation of un-oxidized SPPs into the oxide is responsible for the formation of small voids and cracks [140-142]. They further postulated that the number density of SPPs matter more than the size, i.e., a material with more SPPs would also be expected to have more lateral cracks (and thus a poorer corrosion resistance). Therefore large and far apart SPPs are preferred for improved resistance to uniform corrosion. On the other hand, large precipitates would cause depletion of solute elements between precipitates and local stress build-up, which would make the alloy more susceptible to nodular corrosion [143-145]. For Zr-Nb

alloys, on the contrary, uniformly distributed fine precipitates are preferable for optimum corrosion resistance [146].

2.5.3 Alloying Additions

Alloying elements are added to pure Zr to improve the overall corrosion resistance. These alloying elements can be classified as alpha-stabilizers (Sn and Nb) and beta-stabilizers (Fe, Cr and Ni). The content and distribution of alloying elements will affect the corrosion resistance of the alloys in different ways. For example, elements that have higher valance state than Zr^{4+} could consume some of the oxygen vacancies in order to maintain the electric neutrality, and vice versa. Segregation of alloying elements on specific features will change the electron conduction on those sites.

1) Tin

Tin is an α phase stabilizer [9]. It forms substitutional solid solutions in both α and β phases. A number of previous studies have shown an increase in oxidation rate with increasing Sn content increases [147-149]. The cause for this increased oxidation rate, as given by electrochemical impedance measurements, could be that the higher Sn content increases the ionic and electronic conduction of the oxide layer [150]. However, the concentration of Sn should not be excessively reduced since it also has a positive effect on increasing the

mechanical properties such as yield stress and creep resistance [151, 152]. It is believed that there exists an optimized concentration level of Sn, which is reported to be 1.1-1.7 wt. % by Sell et al. [153].

Pecheur et al. [154] observed metallic Sn near the oxide-metal interface and both Sn^{2+} and Sn^{4+} in the oxide, indicating that Sn generates extra vacancies in the oxide layer. Segregation of Sn to the oxide grain boundaries was also reported [155, 156]. The segregation of Sn into what appears to be grain boundaries could lend support to the ideas that Sn changes oxide conductivity as a result of segregation to oxide grain boundaries creating preferential paths for electron conduction [155, 157]. Also, a recent APT study suggested that the Sn stabilized tetragonal ZrO_2 grains transform to monoclinic when the formation of Sn rich particles depletes the ZrO_2 matrix [158].

2) Niobium

Niobium is a β stabilizer [41]. The maximum solubility of Nb in Zr-Nb alloys is 0.6 at. % [39], but this value is much lower in the Zr-Nb-Fe-O ternary system [32]. Nb forms a solution at low concentrations and hence produces good corrosion resistance. Nb tends to form precipitates in the matrix above a certain concentration [24].

3) Iron, Chromium and Nickel

Fe, Cr and Ni are all considered as "β-eutectoids" [12], because they give a eutectoid decomposition of the β phase as shown in their phase diagrams. At their usual concentration levels, Fe, Cr and Ni are all soluble in β while in α, their solubility is extremely low: 120 ppm for Fe and 200 ppm for Cr at the maximum solubility temperature [19, 159-161]. Fe, Cr and Ni tend to form intermetallic precipitates in the matrix, and the corrosion behavior of alloys is strongly dependent on these second phase particles. Distributions of Fe, Cr and Ni were recently described by APT [162-164], which were much more inhomogeneous than previously expected. Segregation of Fe on grain boundaries and dislocations were also observed. However, the effect of alloying elements distribution on the alloy corrosion resistance is still unclear.

2.6 Summary

Extensive work has been conducted to characterize the microstructures of the oxide phases using various techniques such as TEM, Raman spectroscopy, synchrotron X-ray diffraction and fluorescence. A mixture of monoclinic and tetragonal ZrO_2 has been reported for most alloys, as well as the coexistence of equiaxed and columnar grains. Stronger oxide texture that contains a higher a portion of well-aligned columnar grains correlates to improved corrosion

resistance [63]. The formation of highly orientated tetragonal phase at the oxide front was postulated as the precursor phase leading to the growth of the fiber structure where the [200] direction of monoclinic ZrO_2 lies close to the oxide growth direction [165, 166]. Oxide transition has been associated with several morphological changes (network of cracks, interconnected porosities, etc.) in the oxides undergoing this transition.

The region ahead of the advancing oxide front has been reported to show a complex microstructure with a variety of oxide phases exhibiting lower oxygen content than 66 at.% [63, 81, 83, 134] including ZrO [1, 140, 167, 168], ω-Zr [83], Zr_3O [56, 63, 169], and other oxygen ordered phases [1, 70, 140, 168]. These precursor layers, as yet to be determined, could affect the corrosion kinetics in two principal ways: by using up oxygen that could have been used to form ZrO_2 they slow down the oxide layer advance and by presenting a different material ahead of the advancing oxide they can affect the oxide corrosion kinetics and, possibly the onset of the oxide transition. For example, oxygen could harden the Zr matrix and make it difficult for the metal to be plastically deformed to relieve oxide growth stresses. Since the oxide/metal interface is the place where oxidation happens, it is important to understand what phases are present and how these phases evolve during oxidation.

It has been demonstrated that small differences in the alloying additions can tremendously change the oxidation kinetics (n in Equation 2.2) and the stability of oxide growth. Recent work has shed some lights on the solute distributions near oxide scales [70, 158, 162-164].

However, the observations have not yet translated into a mechanistic understanding of how alloying additions can affect the oxidation kinetics and onset of breakaway transition. The passage of the oxide front will likely alter the solute distributions by either incorporating the solutes into the oxide or reject them to the oxide front next to the advancing oxide. In the first scenario, alloying additions with different valance with Zr^{4+} could change the electron conductivity of the oxide layer. As to the solutes rejected by the oxide front, they can redistribute to defects such as interfaces, dislocations, and grain boundaries and may be able to affect the nucleation of new oxide grains. In either case, solutes can affect the oxidation and should be systematically characterized. To characterize solute distribution, which may exhibit low level of enrichment (a few atomic %) at an extremely fine scale, atom probe tomography (APT) will be the most suitable technique to use.

This thesis research focuses on developing a systematic characterization of the microstructure and microchemistry near oxide scale in zirconium alloys exhibiting different oxidation behaviors. The questions to be addressed include what phases form upon oxidation, how each of the phases grows, and how solutes distribute near the oxide scale. Specifically, by comparing the structure and chemistry in different alloys, we hope to identify the factors that potentially contribute to a slower, more stable growth.

CHAPTER 3

Alloys and Experimental Techniques

3.1 Materials

3.1.1 Model Alloys

The three model alloys studied were pure Zr (crystal bar Zr), Zircaloy-4 (Zr-Sn-Fe-Cr-O alloy), and a Zr-Fe-Cr alloy. The model alloys were selected to investigate the role of alloying on the corrosion behavior of Zr-based alloys. Nominal chemical compositions were measured by ICP-OES (Inductively Coupled Plasma Optical Emission Spectroscopy) given in Table 3.1.

Table 3.1: Chemical composition of selected Zr-based alloy ingots

Alloys		Sn	Fe	Cr	O	C
Pure Zr	(wt. %)	<0.002	0.009	<0.0005	<0.025*	0.014
Zircaloy-4	(wt. %)	1.32	0.19	0.094	0.131	0.015
Zr-Fe-Cr	(wt. %)	<0.002	0.38	0.22	0.112	0.021

* Oxygen value below lowest verifiable calibration point

The fabrication process is illustrated in Figure 3.1. Processing procedures were designed to achieve a recrystallized microstructure (as shown in Figure 3.2) in all three alloys, therefore allowing the roles of specific alloying elements to be visualized and analyzed.

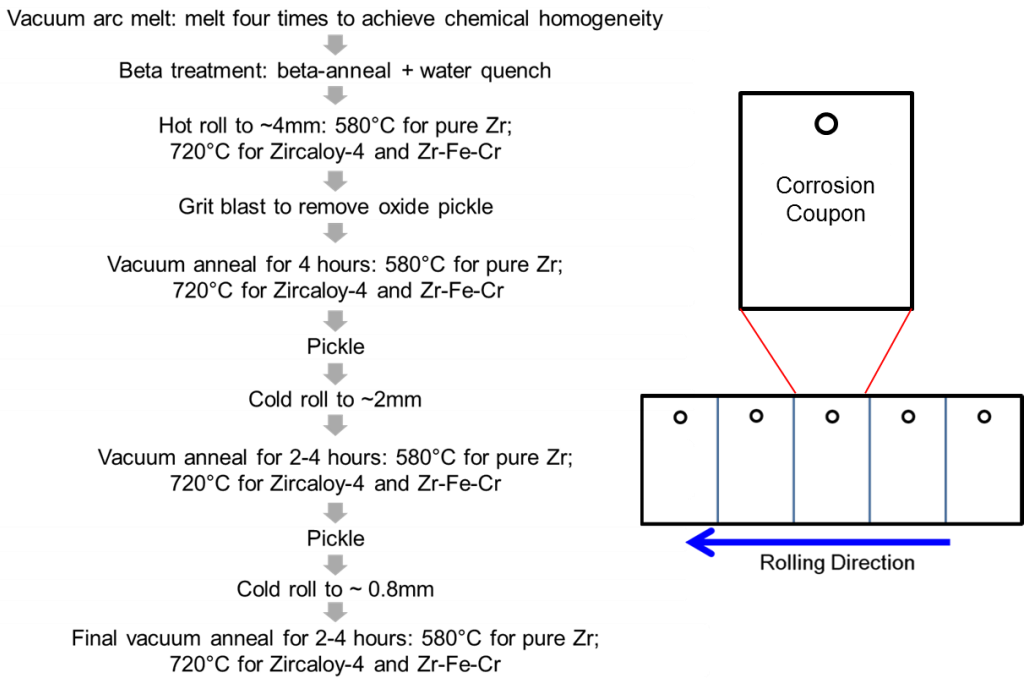

Figure 3.1: Illustration of alloy fabrication process and resulting geometry of sample coupon.

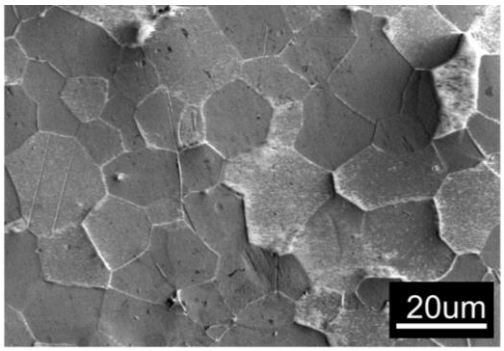

Figure 3.2: SEM image of the surface of pure Zr after 1 day of oxidation illustrating the recrystallized microstructure is still visible.

3.1.2 Autoclave Corrosion Test

The autoclave corrosion tests were conducted by researchers at Pennsylvania State University as part of previous research project [56, 63, 161, 170, 171]. Before the corrosion test, the alloy coupons were ground on 240, 320, 400 and 600 grit silicon carbide papers on both sides and were pickled in a 10% HF- 45% HNO_3- 45% H_2O solution for 5-10 seconds to achieve a flat, clean surface. The model alloys were corroded in water at 360 °C at a pressure of 2708.6 psi (18.7 MPa) following ASTM Practice (G2-88). The corrosion behavior was evaluated by periodically stopping the test, taking samples out of the autoclave, and measuring the weight gain (mg/dm^2). The weight gains are plotted as a function of exposure time (Figure 3.3).

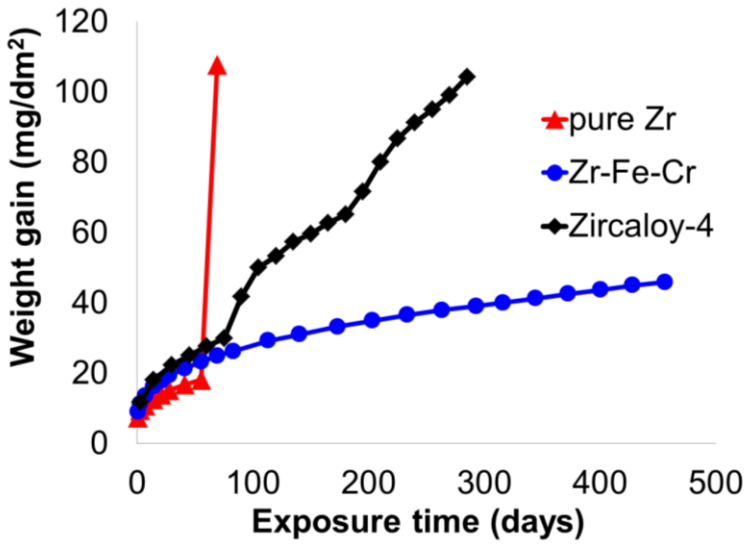

Figure 3.3: Corrosion weight gain-time for studied alloys oxidized in 360 °C water (the graph is re-plotted based on data in [56, 63, 161, 170, 171]).

In operating PWRs conditions, the coolant temperature is approximately 310 °C at a pressure of 2250 psi (15.5 MPa). The 360 °C water autoclave experiments are more severe operating conditions than the ones found in operating PWRs, in terms of temperature and pressure, nonetheless the behavior of the alloys in this environment correlates well with in-reactor behavior [172].

Assuming that all oxygen ingress reacted with Zr to form ZrO_2 oxide (not necessarily true), the oxide thickness were roughly estimated by dividing the weight gain by the density change due to formation of ZrO_2 (~14.7 mg/dm^2). The archived conditions of examined samples are summarized in Table 3.2.

Table 3.2: Corrosion tests conditions of studied alloy samples

Alloys	Exposure time (days)	Weight gain (mg/dm^2)	Estimated oxide thickness (μm)	Oxide Appearance
Pure Zr	1	6.9	0.5	Black
Pure Zr	7	10.5	0.7	Black
Pure Zr	55	10.5*	0.7*	Grey*
Zircaloy-4	60	27.6	1.9	Black
Zircaloy-4	75	41.7	2.8	Black
Zircaloy-4	90	41.7	2.8	Black
Zr-Fe-Cr	7	14.4	1.0	Black
Zr-Fe-Cr	60	24.6	1.7	Black
Zr-Fe-Cr	456	45.6	3.1	Black

*The oxide was undergoing breakaway at some regions, causing some degree of oxide buckling and spallation. The measured weight gain may not be accurate,

3.2 Sample Preparation

3.2.1 Metallography

The initial dimensions of the oxidized coupons were around 20 by 10 by 0.8 mm. The samples were sectioned using a low speed diamond saw to produce samples that could be put into the SEM-FIB dual beam system. One side of the sample was ground and polished using successively finer grind papers and polishing clothes down to 1 μm diamond. The final step was to polish the sample with a mixture of 30% H_2O_2 and 0.05 μm colloidal silica in order to remove the surface damage from previous polishing step.

3.2.2 TEM and APT Sample Preparation

In this thesis research, a FEI Helios 650 Nanolab SEM/FIB was utilized to prepare both TEM lamella and APT needles. The FIB's unique properties allow the analysis specific sample regions without affecting the integrity of the entire sample [173]. The electron transparent foils for TEM analysis were prepared by slightly modify the standard lift-out method [174] (Figure 3.4). A 2 micron thick layer of platinum was first deposited to protect the surface from gallium damage from the ion beam. The stage was then tilted to 52° to dig deeper into the sample surface and then titled back to 3-5° to make a "U"-shaped cut. The tungsten manipulator was used to complete the lift-out once the sample wedge was freed from the bulk.

The lift-out specimen was then carefully glued onto a copper grid using platinum deposited on the base for stability. The stage was then tilted to 51-51.5 degree and 53-53.5 degree to thin the sample from both sides until the foil is less than 200 nm thick and slightly electron transparent. As the final step, 2-5 kV milling was performed on each side to remove any damage from the ion beam.

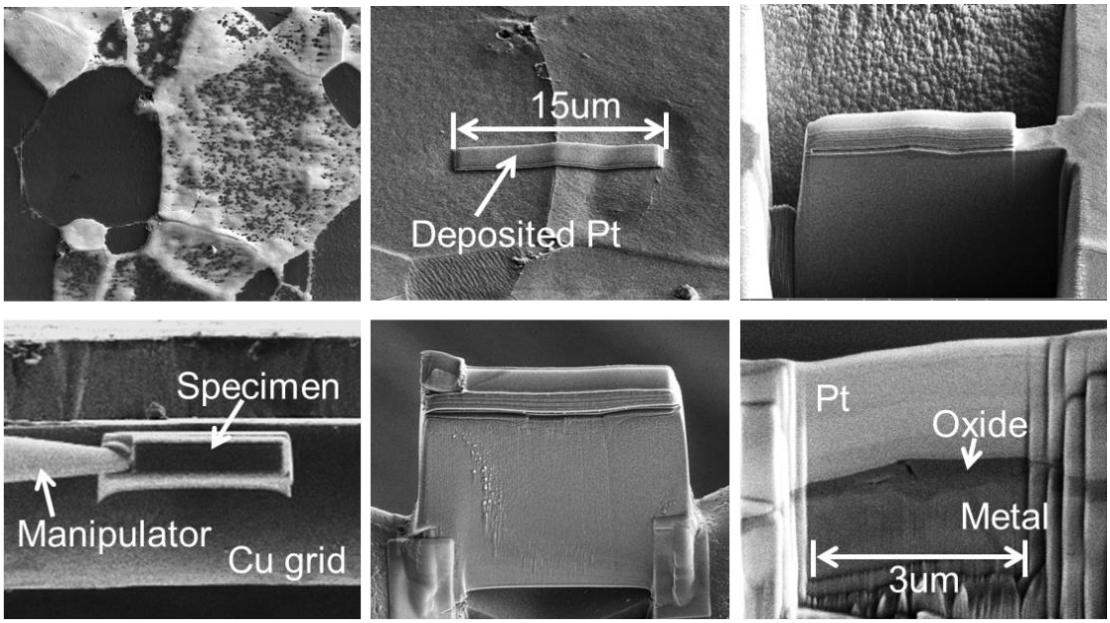

Figure 3.4: Procedures of the FIB-based TEM sample preparation process.

The needle-shaped samples for APT were also prepared using a standard FIB-based lift-out method [175] as illustrated in Figure 3.5. First, a layer of platinum was deposited up to 300 nm depth in order to protect the surface from gallium damage from the ion beam. Two mills angled at 50-60 degrees to the surface were made in order to cut a lift-out specimen wedge. The manipulator was mounted to one side of the sample wedge and then lifted the wedge out

after the other side was cut free from the bulk. The lift-out specimen was then glued onto unsharpened silicon pillar using platinum deposition and then cut free. Annular milling of the tips was then conducted to incrementally reduce the radius of the tip apex to less than 100 nm. As the final step, a 2 kV milling was performed to remove any remaining Pt and to minimize the Ga damage region formed from the ion beam during annular milling.

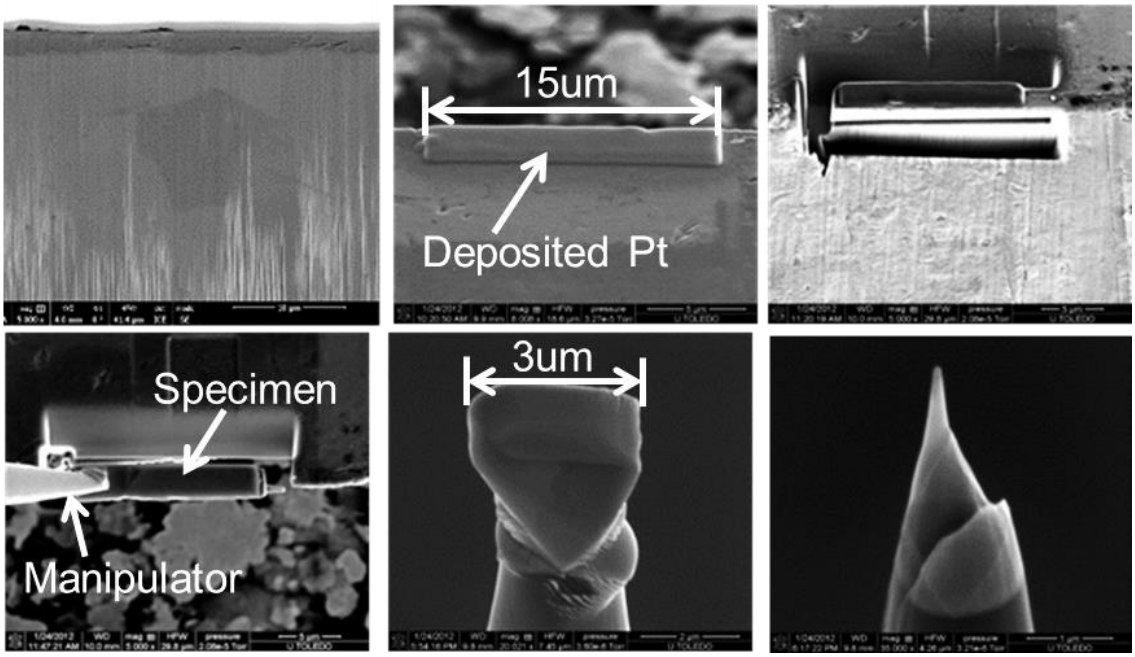

Figure 3.5: Procedures of APT tips preparation using FIB.

APT samples with different orientations with respect to the sample surface were fabricated (Figure 3.6). Needles with interfaces parallel to the needle axis contained more interface region. The needles that contained interfaces perpendicular to the needle axis were beneficial for exploring the oxygen ingress into the metal substrate.

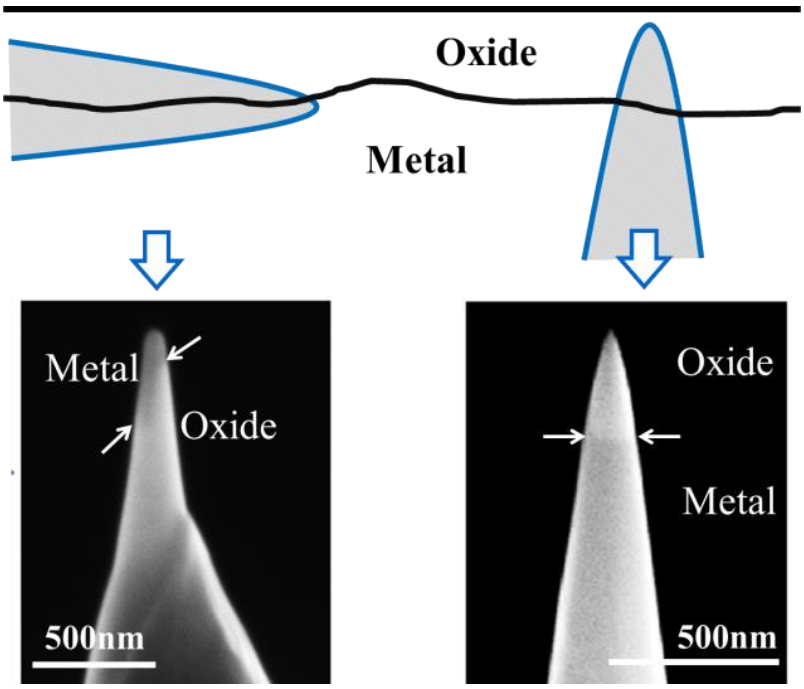

Figure 3.6: Schematic illustration (top) and SEM images (bottom) of the two interface orientations selected for the APT needles.

3) EBSD surface preparation

The EBSD study of oxidized Zr alloys proved difficult because the traditional chemical etching procedure fail to etch the metal and oxide at comparable rates. Thanks to the dual beam SEM/FIB platform, it is possible to conduct EBSD orientation mapping on the FIB created surface. The procedure is illustrated in Figure 3.7. The sample was first mounted on the vertical surface of the 45° pre-tilt holder, where focused ions were utilized to slice away the top layer of the material and create a surface for EBSD. The sample was then mounted on the 45° surface where EBSD data can be collected.

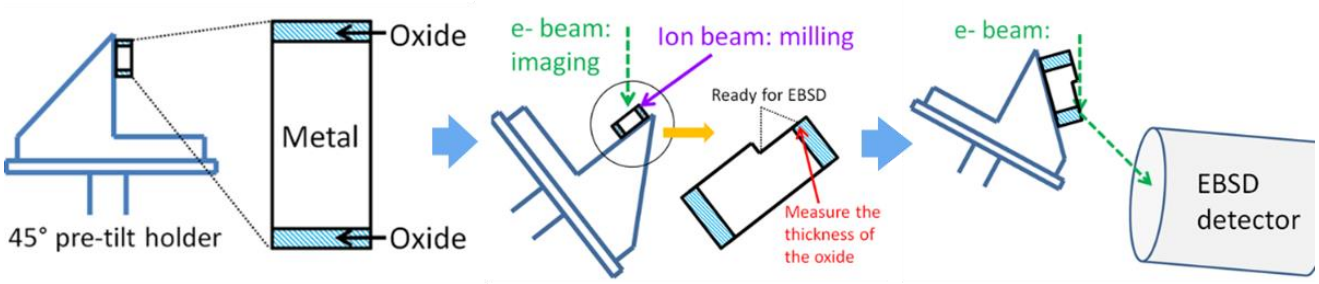

Figure 3.7: Procedures of utilizing FIB to mill the surface for EBSD examination.

3.3 Characterization Techniques

3.3.1 SEM and TEM

SEM is widely used to as a surface technique to characterize the topography and chemistry from specimen's surface to a depth of approximately 1 μm [176, 177]. In this thesis research, oxidized zirconium alloy samples were analyzed using a FEI Helios 650 Nanolab SEM/FIB that operated at 2-30 kV and equipped with an EBSD detector. Two TEMs operated under conventional TEM mode were used to characterize the oxide layers (grain size, shape, morphology) formed on Zr-based alloys through bright-field imaging, dark-field imaging and electron diffraction. The two instruments are a JEOL HREM 3011 that operates at 300 kV and a 200 kV JEOL AEM 2010F.

3.3.2 Atom Probe Tomography (APT)

Atom probe tomography (APT) provides three dimensional atom-by-atom mapping at high spatial and chemical resolution [178-181]. In APT, atoms from the surface of a needle-shaped specimen evaporate as positively charged ion due to applied high electric field. The evaporation field F is defined as the field strength required to evaporate the surface atoms:

$$F = \frac{V}{k_f R} \qquad \text{(Equation 3.1)}$$

Where V is the applied electric potential, R is the radius of curvature of the tip and k_f is a numerical constant.

1) Instrument

In this work, the needle-shaped specimens prepared by FIB were analyzed using a CAMECA LEAP-4000X HR system. Evaporation of atoms in APT can then be achieved by applying either voltage pulses (up to 200 kHz) or femtosecond laser pulses (50 to 500 kHz) on top of a standing voltage and a base temperature. The instrument has a reflectron configuration and a detector efficiency of ~ 37 %.

2) Calibration of Analysis Condition

The base temperature for all the APT analysis was set in the range of 40-50 K, which was reported to be a suitable range by Hudson in a previous APT work on zirconium alloys [162].

Voltage and laser pulse were then applied to the needle-shaped specimen to maintain a specified detection rate. The target detection rates were selected based on the specimen conditions. Lower evaporation rates (0.2 %- 0.5 %, i.e. 0.002-0.005 ions/pulse) were used when the specimen contains microstructural features like interfaces or grain boundaries.

Choosing the appropriate laser pulsing energy is critical in APT analysis as too high laser energy can introduce evaporation artifacts. At higher laser energy, the energy deposited in each pulse is too large for the heat to be dissipated and can lead to an increase in local evaporation rate and therefore reduction in local curvature of the area where laser hit the specimen [182]. The reduction of local curvature (flattening) may be visible as the apparent density increases due to a reduced local magnification. Also, failure to conduct the heat also increase the temperature and can result in surface diffusion of relatively mobile solutes [183].

To study the impact of laser energy, APT datasets that contained roughly 5 million ions were collected at various laser energies between 60 pJ to 150 pJ. A very high incidence of fracture before acquiring sufficient number of ions occurred in specimens analyzed using laser energy below 60 pJ. The analysis was conducted on two Zircaloy-4 APT needles: one was analyzed at 80 pJ, 100 pJ, 120 pJ and 150 pJ; the other one sampled 60 pJ, 70 pJ, 80 pJ, 90 pJ and 100 pJ. The atomic maps viewing from z-direction are summarized in Figure 3.8 and Figure 3.9.

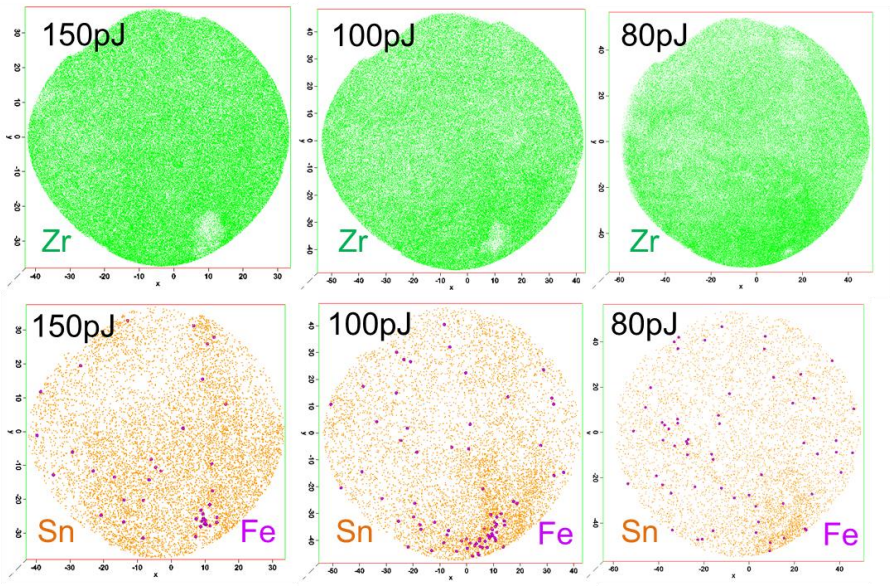

Figure 3.8: 2D atomic maps showing the effect of laser power (150 pJ to 80 pJ) on the observed local distribution of Zr, Fe and Sn ions.

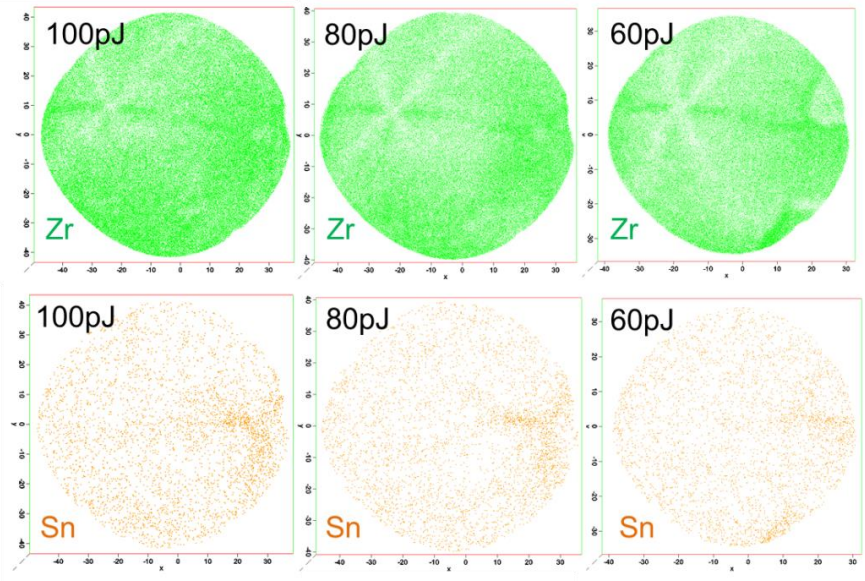

Figure 3.9: 2D atomic maps showing the effect of laser power (100 pJ to 60 pJ) on the observed local distribution of Zr and Sn ions. Fe maps are not shown here as no preferential distribution of Fe can be observed.

As seen in Figure 3.8, when laser energy was above 100 pJ, segregation of Fe could be observed on the bottom right of the 2D atomic maps, indicating the surface diffusion of Fe. The Fe segregated region also showed lower Zr concentration compare to surrounding area. At 80pJ, segregation of Fe was no longer visible. Preferential evaporation of tin was also visible. As the laser energy decreased, the degree of preferential evaporation decreased and eventually became minimal at 60 pJ (Figure 3.9), accompanied by occurrence of crystallographic poles on the Zr maps. Further decrease in laser energy significantly increased the incidence of sample fracturing.

In this thesis work, laser energies between 60 pJ and 80 pJ were selected. The evaporation field F (F in Equation 3.1) at the APT tip apex could be estimated by measuring the ratio of ions detected at different charge states. At laser energy between 60 pJ to 80 pJ, zirconium mainly evaporated as Zr(II) with a small amount of Zr(III) and Zr(I). The Zr(III)-to-(Zr(I)+Zr(II)+Zr(III)) is plotted as a function of laser energy and roughly fitted to the theoretical Kingham curve [184] in Figure 3.10. For the specimen tested, varying the laser energy from 60 pJ to 80 pJ yielded a field strength between 25 V/nm to 26.5 V/nm.

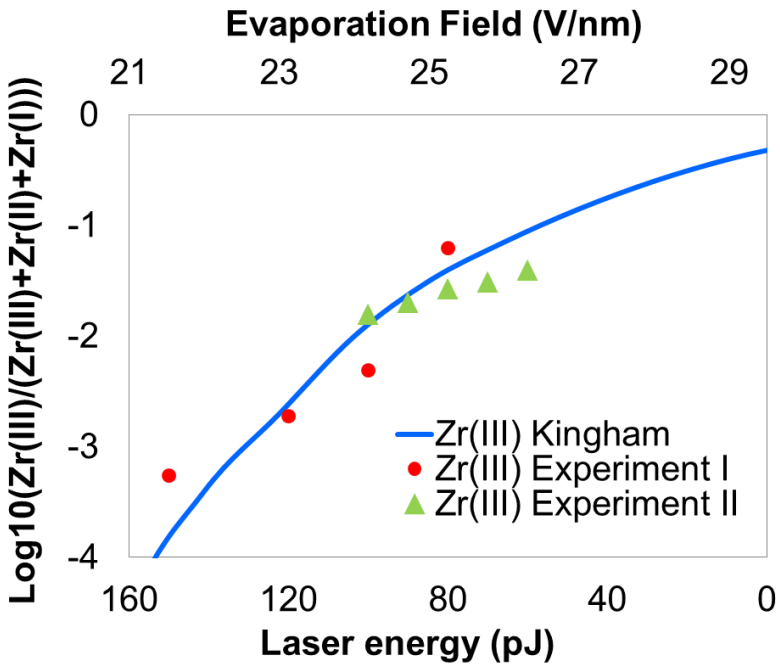

Figure 3.10: Estimation of evaporation field as a function of laser energy. The blue curve is theoretical predication of the field based on charge state ratio (Kingham curve). Red circle and green triangle are experimental observations calculated from APT datasets that obtained at different laser energy. Each experimental data point was calculated from 5 million ions.

3) Reconstruction

Three different methods can be chosen to calculate the radius evolution in the analysis software IVAS: voltage-based reconstruction, shank angle reconstruction, and tip profile reconstruction. The voltage-based reconstruction uses Equation 3.1 so that the tip radius used for reconstruction is strictly based on the total voltage for a given ion. The shank angle based reconstruction assumes specific tip geometry and tip radius is assumed to evolve ion by ion. Alternatively, by obtaining a high quality electron microscopy image prior to APT analysis, a radius evolution function can be determined by placing a series of tracer lines on the actual tip

profile. In this thesis research, the majority of the raw data collected from APT were reconstructed using the voltage-based reconstruction method in IVAS. Three input parameters were used to reconstruct the data into 3D reconstructions: evaporation field F, geometric factor k, and image compression factor ICF. Since the evaporation field is correlated to the geometric factor through Equation 3.1, it was treated as material properties at constant temperature and 26 V/nm was selected for zirconium metal in this study.

Around the pole regions, the resolution was high-enough to image individual atomic planes (Figure 3.11(a)). The poles can be indexed by matching the interplanar spacing and the relative position of the corresponding pole on the stereographic projections. Once the poles are indexed correctly, they can serve as guidance for determining the ICF and k-factor [185, 186], as well as analyzing the crystallographic orientation of microstructural features..

Different values for ICF and k-factor were selected to reconstruct the same APT dataset and the corresponding interplanar spacings are plotted and compared in Figure 3.11. According to Figure 3.11, an ICF between 1.65 and 1.8 and a k factor ranging from 4.8 to 5.2 can give rise to interplanar spacings that are close to calculated value.

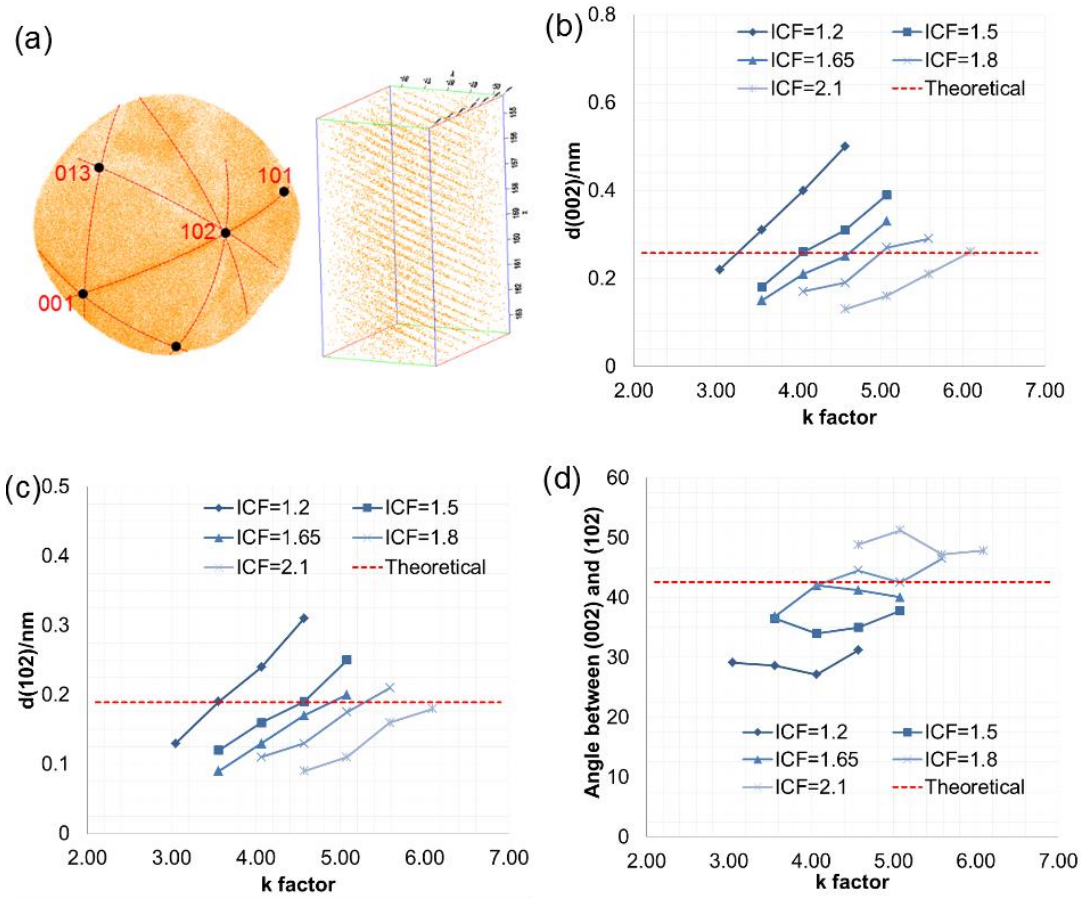

Figure 3.11: (a) 2D atomic Zr map showing the presence of crystallographic poles and 3D map of atomic planes; Measured spacing of (b) (002) plane and (c) (102) plane as a function of k factor at under different ICFs; (d) Measured angle between (002) and (102) planes as a function of k factor at under different ICFs. Evaporation field was set at 26 V/nm.

The evaporation field of ZrO_2 oxide is slightly lower compare to zirconium metal, as evident in the sudden increase in the voltage history when passing through the oxide/metal interface (Figure 3.12(a)). The voltage increase can be used to quickly estimate the evaporation field of ZrO_2. According to Equation 3.1,

$$\mathrm{F} = \frac{V}{k_f R} \quad \rightarrow \quad \mathrm{V} = \mathrm{F} \cdot (k_f R)$$

Set V_2 as the voltage in the metal region, V_1 as the voltage in the oxide region, then at interface:

$$\text{R} = \text{R}_0 \text{ (at interface): } V_2 - V_1 = k_f \cdot R_0 \cdot (F_2 - F_1) \rightarrow \Delta\text{V} = k_f \cdot R_0 \cdot \Delta\text{F}$$

In Figure 3.12(a), set the interface at ion sequence = 4×10^6:

$$\Delta\text{V} = 1156\text{V} = k_f \cdot R_0 \cdot \Delta\text{F}$$

Set k factor to 4.6-5.2 (the range determined previously as shown in Figure 3.14) and R_0 to 80 nm (roughly estimated from SEM image):

$$\Delta\text{F} = \frac{\Delta V}{k_f R} \rightarrow \Delta\text{F} \approx 2.9 \sim 3.2 \text{ V/nm}$$

Since the field strength of metal was estimated to be 26 V/nm, the field of oxide is:

$$\text{F } (ZrO_2) \approx 23 \text{ V/nm}$$

The evaporation field can also be estimated using the TEM image of the APT specimen:

$$\text{V} = \text{F} \cdot \left(k_f R\right) = 4129\ V \text{ , based on voltage history}$$

The radius of curvature was measured 36.5nm as shown in Figure 3.12(b):

$$\text{R} = 36.5 \text{ nm, } k_f = 4.8 - 5.2 \rightarrow \text{F } (ZrO_2) = 21.8 - 23.6 \text{ V/nm}$$

The estimated values using the two methods were consistent with each other.

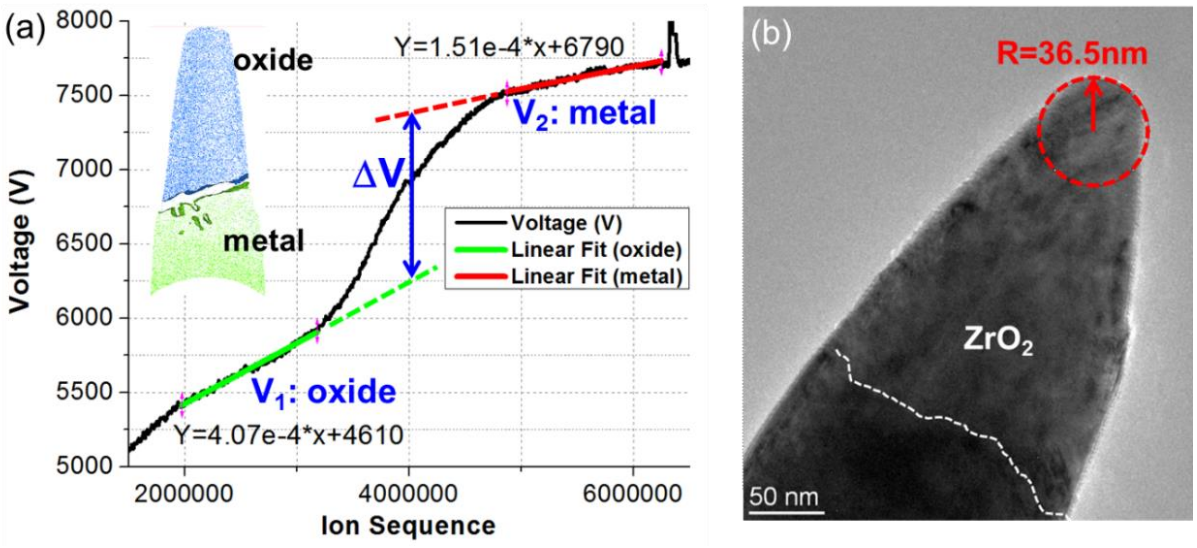

Figure 3.12: (a) voltage history during analyzing the APT specimen shown on the upper left. The voltage history was utilized to estimate the evaporation field of the ZrO_2 oxide. (b) TEM image of the APT specimen. The measured radius R, voltage required to evaporate the ions and the evaporation field calculated from (a) were used to calculate the k factor.

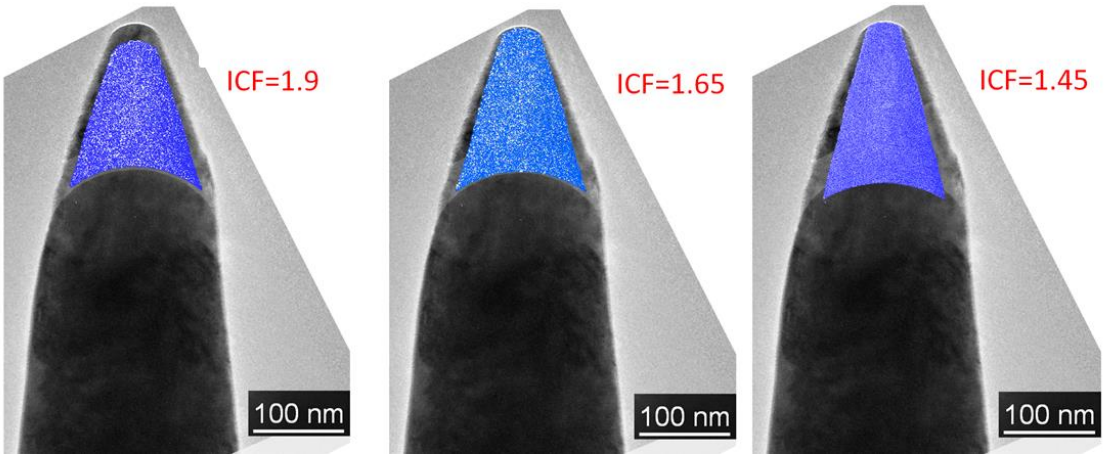

Figure 3.13: APT atomic maps of ZrO_2 oxide reconstructed by using different ICF values. The APT reconstructions are superimposed onto TEM images taken before and after APT experiments to check whether the reconstructions have the correct scale. Evaporation field was set at 23 V/nm and k factor was set at 5.

Setting field at 23 V/nm and k factor at 5, the ICF could be determined by matching the z scale of reconstructed data with the actual amount of materials that has been field evaporated. As seen in Figure 3.13, as ICF increased, the tip was compressed more along the tip axis. An ICF of 1.65 yielded a better match with TEM image.

One of the most important assumptions made here is that all the reconstruction parameters remain constant for a specific APT dataset. However, the shape of the specimen changed at the same time with which atoms were being evaporated, resulting in a change in both k factor and ICF. It is worth noting that the reconstruction parameters selected in the process outlined above were the best estimate given the stated reconstruction algorithm. They might not yield the most accurate representation of the evaporated volume.

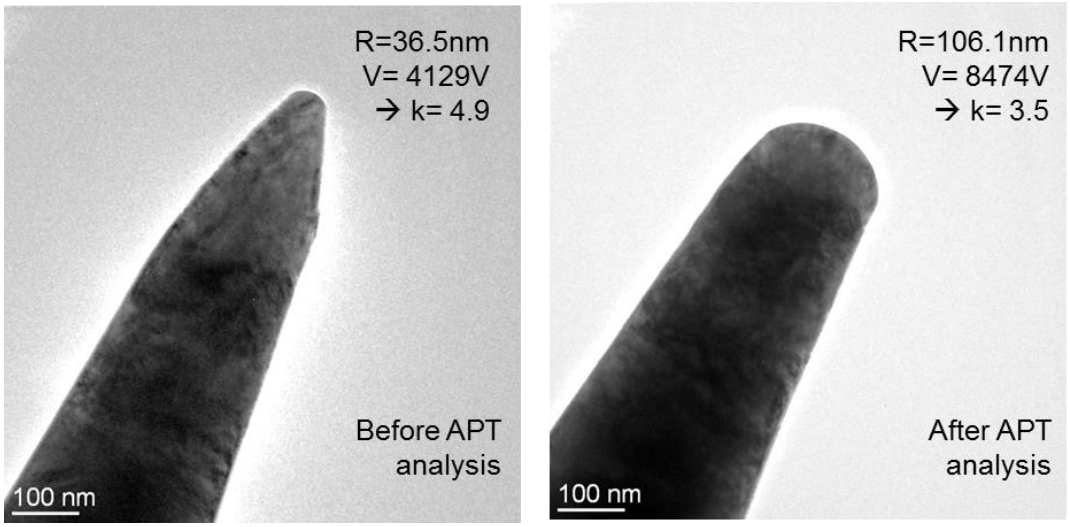

Figure 3.14: TEM images of the same specimen before and after APT analysis. Note that the change of specimen shape causes the change in the value of k factor.

4) Summary

Based on the calibration test, laser energy ranging from 60 pJ to 80 pJ could effectively prevent laser induced artifacts and therefore was selected for running APT experiments on corroded alloy specimens. Reconstructing the obtained APT datasets correctly was a more complicated process. High resolution micrograph or/and crystallographic poles were utilized as useful guidance but those data were not always available. The reference study described in this chapter suggests that the combination of ~26 V/nm as evaporation field, a k factor in the range of 4.6 to 5.2, and an ICF between 1.65 and 1.8 leads to reasonable reconstruction.

However, given the evolution of both specimen geometry and phases (oxide → suboxide → metal) during an APT analysis, the actual values of above parameters will change significantly as more atoms are being evaporated away from the specimen surface. For the results presented in the subsequent chapters, the reconstruction parameters for each dataset were determined individually by slightly modifying the method with additional information on the scale or/and shape of specific microstructural features (e.g. crystallographic planes, spherical clusters).

CHAPTER 4

Alloy Microchemistry

4.1 Overview

Characterization of the bulk metal away from the oxide scales is necessary as it provides a baseline for subsequent analyses on corroded materials. This chapter describes the APT analyses of the chemistry in the starting alloys. All samples were taken at least 100 μm away from the oxide/metal interface. The measured alloy composition and observed alloying element distributions were consistent with what was known from previous studies. The APT study also provided additional observation of Fe segregation to grain boundaries and the presence of Fe and Cr rich nano-precipitates.

4.2 Pure Zr

APT samples taken in the bulk of the alloy, i.e. far away from the oxidized surface (~200 μm), showed a uniform distribution of Cr without any evidence of clusters or indication of

elemental segregation to microstructure features such as grain boundaries or dislocations. Very small amount of Fe was detected in the matrix – note that the detection limit for Fe was about 0.002 at. % (12 wt. ppm). Concentration measurements from the APT datasets matched the Zr and Cr concentrations measured using hot vacuum extraction as shown in Table 4.1.

Table 4.1: Chemical composition of zirconium alloy ingots as measured by hot vacuum extraction (HVE) and matrix composition as measured by APT. Errors of APT measurements are calculated from dataset to dataset variations and counting statistics within each dataset.

		Sn	Fe	Cr	O	C
Pure Zr	HVE (wt.%)	<0.002	0.009	<0.0005	<0.025*	0.014
	HVE (at. %)	<0.002	0.015	<0.002	<0.14	0.11
	APT (at. %)	N.A.	0.002 ±0.001	0.002 ±0.001	0.032 ±0.002	0.008 ±0.001
Zircaloy-4	HVE (wt.%)	1.32	0.19	0.094	0.131	0.015
	HVE (at. %)	1.01	0.31	0.16	0.74	0.11
	APT (at. %)	0.99 ±0.03	0.003 ±0.002	0.015 ±0.010	0.9 ±0.03	0.07 ±0.04
Zr-Fe-Cr	HVE (wt.%)	<0.002	0.38	0.22	0.112	0.021
	HVE (at. %)	<0.002	0.61	0.36	0.63	0.16
	APT (at. %)	N. A.	0.004 ±0.002	0.015 ±0.002	0.68 ±0.002	0.04 ±0.002

* Oxygen value below lowest verifiable calibration point

Small amounts of C, O and Al were also detected. The low Fe concentration measured in the matrix was reasonable since the alloy was in a recrystallized state with a final heat-treatment temperature corresponding to an extremely low solubility of Fe in Zr [187]. The reported

maximum solubility of Fe in α-Zr is 120 wt. ppm (0.02 at. %) at 800 ºC and less than 50 wt. ppm (0.008 at. %) at temperatures lower than 300 ºC [187].

Fe was found to be segregated to grain boundaries, as illustrated in Figure 4.1. Segregation of other elements was not observed on the grain boundaries. It was expected that if APT was to be performed over a representative volume of the microstructure containing regions of high iron concentration the values would match the composition measured by hot vacuum extraction.

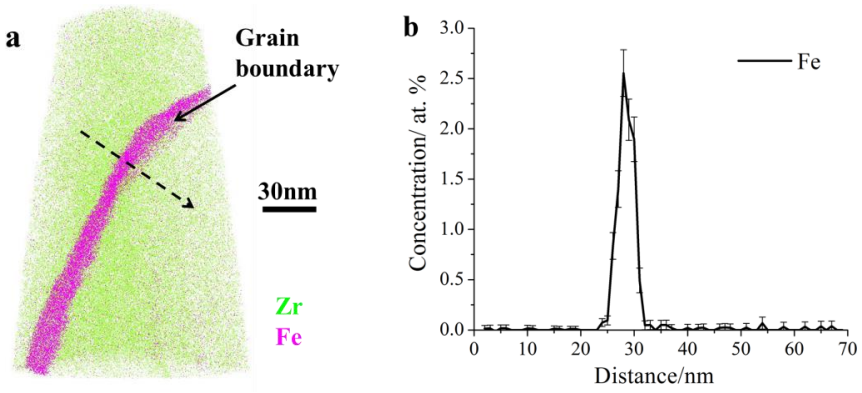

Figure 4.1: Bulk pure Zr: (a) APT reconstruction showing a grain boundary with Fe segregation; (b) concentration profile across grain boundary measured by placing a 10 nm cylinder along the arrow shown in (a).

4.3 Zircaloy-4

Zircaloy-4 contains Sn, Fe and Cr as major alloying elements. Sn was found in solid solution and Fe and Cr mostly in intermetallic precipitates of the type $Zr(Fe, Cr)_2$ [187, 188]. The

matrix Sn concentration was measured from the bulk of the metal far away from the oxide, and calculated from a dataset without grain boundaries and clusters. The Fe and Cr matrix concentrations determined by APT were close to the reported solubility limits (0.04 at. % for Cr at 860 ºC and 0.02 at. % for Fe at 800 ºC [161]), which are much lower than the bulk alloy concentration, since essentially all Fe and Cr were in precipitates.

From previous work [161], the precipitate number density in recrystallized Zircaloy-4 was around 0.7×10^{12} cm^{-3}, and the average spacing between precipitates (usually 0.1-0.3 μm in size) was greater than 1 μm, so their capture in the APT specimens was unlikely. However, some small clusters (~ 5 nm diameter), which would normally be invisible in TEM were occasionally seen by APT, as shown in Figure 4.2(a). The apparent composition of these clusters was obtained from a proxigram analysis based and is 89.3±1.9 at. % Zr, 4.8±1.3 at. % Fe, 5.9±0.7 at. %Cr. However, these numbers were affected by ion trajectory aberrations from the difference in evaporation fields between matrix and clusters, as evidenced by the apparent higher density of ions observed at the position of the clusters [37].

Fe and Sn segregation was observed at grain boundaries (Figure 4.2(b)). A line profile of concentration through the grain boundary in Figure 4.2(c) shows noticeable segregation of Fe (up to 1.5 at. % or an enrichment factor of 5 relative to the alloy bulk and much higher relative to the Fe content in the matrix. A much less marked segregation of Sn was also discerned in the same figure. No segregation of other elements was seen on the grain

boundary. No evidence was seen for solute segregation to dislocations but this may be because of the low dislocation density in the recrystallized material.

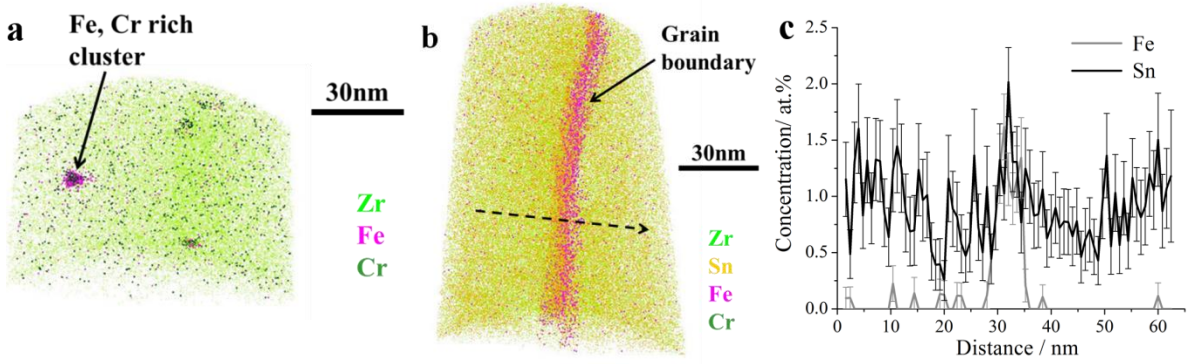

Figure 4.2: Bulk Zircaloy-4: (a) APT reconstruction showing Fe, Cr rich clusters; (b) APT reconstruction showing grain boundary with Fe and Sn segregation; (c) concentration profile across grain boundary measured by placing a 10 nm cylinder along the arrow shown in (b).

4.4 Zr-Fe-Cr

As shown in Table 4.1, the measured matrix concentrations of Cr and Fe in the bulk of the alloy were much lower than the overall alloy composition, likely because most of the Fe and Cr were found in C14 Zr $(Fe, Cr)_2$ Laves phase precipitates [187, 188]. A portion of one such precipitate was caught in one of the needles, as seen in Figure 4.3. The measured atomic composition of 34.50±0.11 at. % Zr-43.68 ±0.10 at. % Fe-21.82±0.08 at. % Cr, was in reasonable agreement with the overall stoichiometry of the Zr $(Fe, Cr)_2$ Laves phase.

Similarly to Zircaloy-4, Fe segregation to grain boundaries was observed to a similar level as in Zircaloy-4 as shown in Figure 4.4 and some Al, O and C are also observed in the matrix.

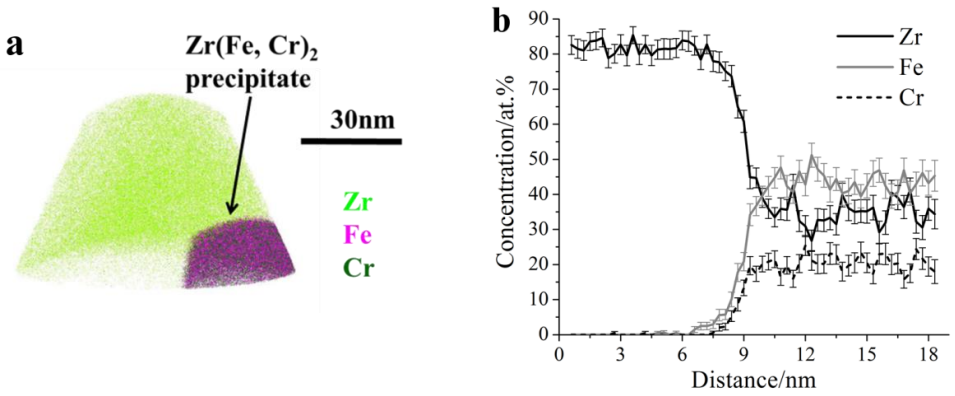

Figure 4.3: Bulk Zr-Fe-Cr: (a) APT reconstruction showing part of an Fe, Cr rich intermetallic precipitate; (b) concentration profile across the precipitate interface.

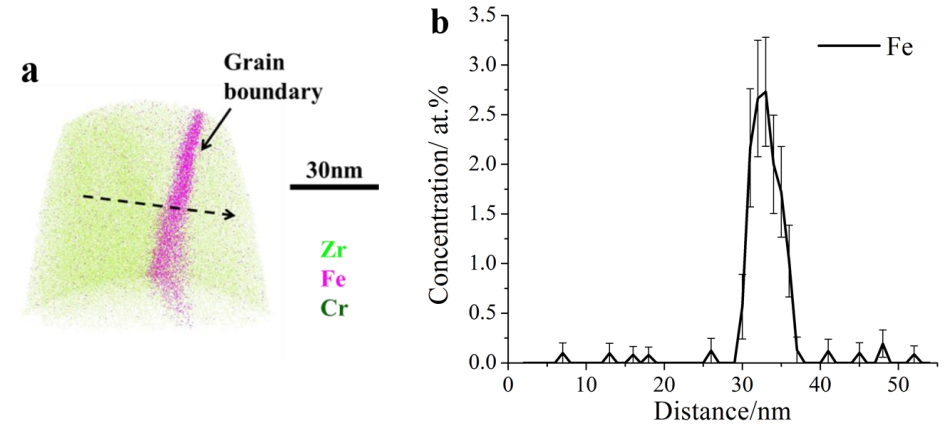

Figure 4.4: Bulk Zr-Fe-Cr: (a) APT reconstruction showing the grain boundary with Fe segregation; (b) concentration profile across the grain boundary measured by placing a 10 nm cylinder along the arrow shown in (a).

CHAPTER 5

Structure and Morphology of Growing Oxide[1]

5.1 Overview

The corrosion rates observed in different alloys were thought to be related to the microstructures of the oxide layers formed in these alloys [61, 68]. As discussed in chapter 2, different suboxide phases were reported to be present at the interface between ZrO_2 oxide and solid solution, including an equiatomic suboxide ZrO [52, 70, 72, 135, 141, 166, 167], an hexagonal ω-Zr [83], an Zr_3O phase [56, 63, 169] and other oxygen ordered phases [1, 70, 140, 168]. However, no agreement has been reached upon what phases are present and how those phases evolve at different stages of oxidation.

[1] The content of this chapter includes the following two articles:
[1] Y. Dong, A. T. Motta, and E. A. Marquis, "Atom probe tomography study of alloying element distributions in Zr alloys and their oxides," Journal of Nuclear Materials, 2013 (442) p. 270-281.
[2] B. de Gabory, Y. Dong, A. T. Motta, and E. A. Marquis, "EELS and atom probe tomography study of the evolution of the metal/oxide interface during zirconium alloy oxidation," Journal of Nuclear Materials, 2015 (462) p. 304-309.

The inconsistent findings reported in the literature could be due to limitations in either chemical or spatial resolution of the experimental techniques. For example, the complex interface morphologies make it difficult to make "edge-on" TEM samples, where the interfaces lie parallel to the incident electron beam. As a result, the concentration profiles measured by EDS or EELS could be the average of two or more phases that are present through the thickness of a TEM sample. APT, on the other hand, allows three dimensional imaging of atom arrangements and therefore should provide a more accurate description of oxide phases.

In this chapter, we studied the structure and morphology of growing oxides at different stages of oxidation. Detailed analyses of the composition and morphology of each oxide layer were obtained from the APT measurements. TEM characterization was utilized to validate the APT analysis and to provide crystal structure information.

5.2 Oxide Phase Sequence

APT specimens were prepared from the oxide and oxide-metal interface regions in the three alloy samples. ZrO_2 formed as a result of the reaction appears as the oxide layer. A series of oxygen-containing sub-oxide phases were observed for all three alloys. These phases were in order from the oxide metal interface:

(i) the equiatomic suboxide ZrO (both slightly sub- and super-stoichiometric, denoted here ZrO_{1+x} and ZrO_{1-x}),

(ii) a saturated solution of constant oxygen content at about 30% O, dubbed $Zr(O)_{sat}$,

(iii) an under-saturated solid solution of O in Zr, the oxygen content of which decreased with distance from the oxide-metal interface.

As stated above, the field evaporation behavior of these phases is drastically different, resulting in characteristic ions being evaporated from each phase. As a result, the phases can be identified both by atomic concentrations and by the nature of the ionic species evaporating from each phase. The latter method was also used to visualize the distribution of phases within needles. For example, it was found in the present study that oxygen was evaporated as O^+, O_2^+, ZrO^{2+}, ZrO^{3+}, ZrO_2^+, ZrO_2^{2+}, ZrO_3^+ with occasional instances of $Zr_2O_2^{3+}$ and $Zr_2O_3^{3+}$ observed. Zr ions (Zr^{2+}, Zr^{3+}) became significant in the $Zr(O)_{sat}$ phase. O_2^+ was only observed in the oxide (ZrO_2) phase, so it was considered a marker for that phase. ZrO_2^+ and ZrO_2^{2+} were present both in the ZrO_2 and observed ZrO_{1+x} phases but absent in the ZrO_{1-x} phase.

5.2.1 Pure Zr

A representative APT dataset from a needle prepared containing the oxide-metal interface of pure Zr is shown in Figure 5.1. A minor fracture occurred as the tip was being analyzed so

that the data before and after the minor fractured were reconstructed separately. An iso-surface with constant Zr concentration is shown in Figure 5.1(a) to show the interface between $Zr(O)_{sat}$ and solid solution. The same iso-surface was used in other figures for the same purpose. The line profile in Figure 5.1(b) was obtained by integrating the contents of a cylinder perpendicular to the interface, as indicated by the arrow in Figure 5.1(a).

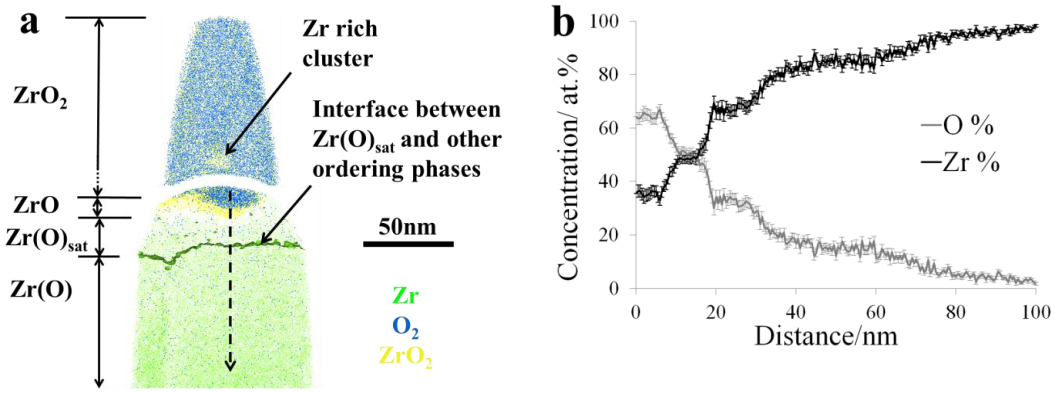

Figure 5.1: Crystal bar Zr oxide region: (a) a 10 nm slice from an APT reconstruction containing the oxide/metal interface; (b) concentration profile measured by placing a 10 nm cylinder along the arrow indicated shown in (a).

The resulting oxygen concentration profile taken along the reconstruction axis, showed that the composition of the top oxide layer was consistent with that of ZrO_2. The sequence of phases followed that outlined above: an intermediate layer observed beneath the ZrO_2 layer with a composition corresponding to ZrO (a ZrO cluster was also observed near the ZrO_2/ ZrO interface but inside the ZrO_2 phase), a saturated solid solution layer with 31- 32 at. % oxygen content, $Zr(O)_{sat}$,and a region of under-saturated solid solution with an oxygen profile

continuously decreasing. The phase diagram has predicted many ordered phases of Zr(O) solid solution, and it was possible that some of these were present at the distance 30 nm (corresponding to Zr_3O) to 50 nm (approx. Zr_4O) considering the slope changes at that location, but their presence remained to be confirmed. The intermediate oxide layers (ZrO and $Zr(O)_{sat}$) in pure Zr were quite thin (less than 20 nm).

5.2.2 Zircaloy-4

The examination of a needle taken from the oxide-metal interface of Zircaloy-4 showed a similar oxide sequence as that seen in pure Zr, but with thicker intermediate layers of ZrO and $Zr(O)_{sat}$. One dataset with the interface perpendicular to the tip axis (vertical) is shown in Figure 5.2. The line profile across the arrow in Figure 5.2(a) is shown in Figure 5.2(b). The ZrO layer was about 50 to 100 nm thick, and the $Zr(O)_{sat}$ was about 100 to 150 nm thick. More detailed examination showed that the ZrO layer actually consisted of two layers with slightly different compositions, slightly above and slightly below stoichiometry. As seen in Figure 5.2(a), in this sample also the region represented by ZrO_{1+x} (in yellow) had a composition slightly rich in O while the region denoted ZrO_{1-x} (in white) was slightly deficient in O.

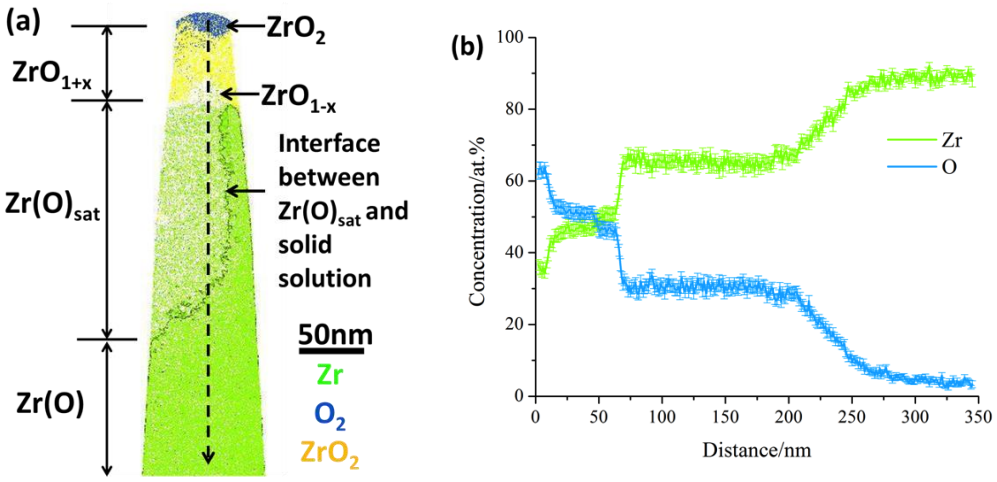

Figure 5.2: Zircaloy-4 oxide region: (a) 10 nm slice from an APT reconstruction; (b) concentration profile measured by placing a 10 nm cylinder along the arrow indicated in (a).

5.2.3 Zr-Fe-Cr

The same sequence of suboxide and oxide phases seen in pure Zr and Zircaloy-4 was observed in the Zr-Fe-Cr alloy. However, the intermediate ZrO layer was much thicker (at least 300 nm) than seen in pure Zr and Zircaloy-4. The needle used for APT analyses fractured before reaching the solid solution region. One of the reconstructed datasets is shown in Figure 5.3(a). A concentration profile of this Zr rich region is shown in Figure 5.3(b).

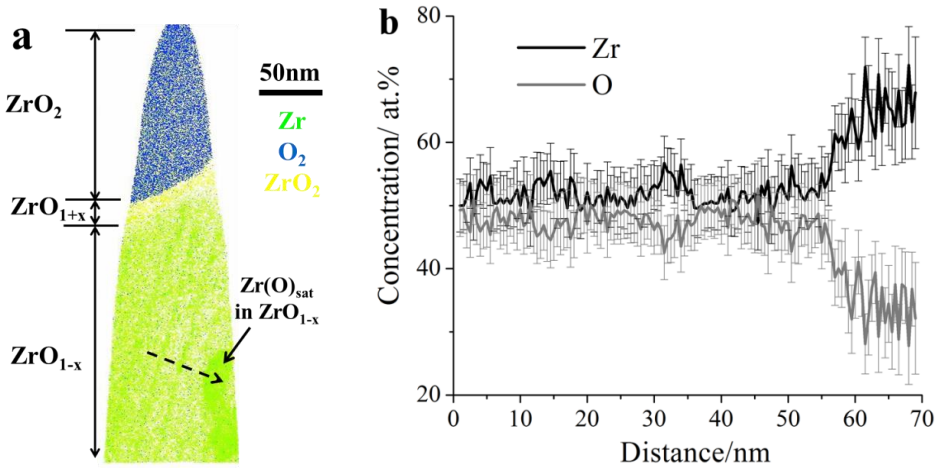

Figure 5.3: Zr-Fe-Cr oxide region: (a) 10nm slice from an APT reconstruction showing the presence of different oxide phases; (b) concentration profile measured by placing a 10 nm cylinder along the arrow indicated in (a).

5.2.4 Field Evaporation Behavior of the ZrO Layer

As observed by APT, the ZrO phase consisted of two layers that were slightly sub- and super-stoichiometric, denoted ZrO_{1-x} and ZrO_{1+x}. The ZrO_{1+x} phase was very thin in most cases (< 20 nm). The interface between ZrO_{1+x} and ZrO_{1-x} always followed the morphology of the ZrO_2/ZrO_{1+x} interface. Observing an oxide phase with a slightly lower O concentration than expected such as ZrO_{1-x} is common in APT analyses, however, observing a super stoichiometric oxide (ZrO_{1+x}) is more surprising. The morphology of this phase suggests that it could be an artifact resulting from the application of an electric field. The field present in the insulator led to O migration to the interface and reaction of the O ions with the conductive layer that lied beneath.

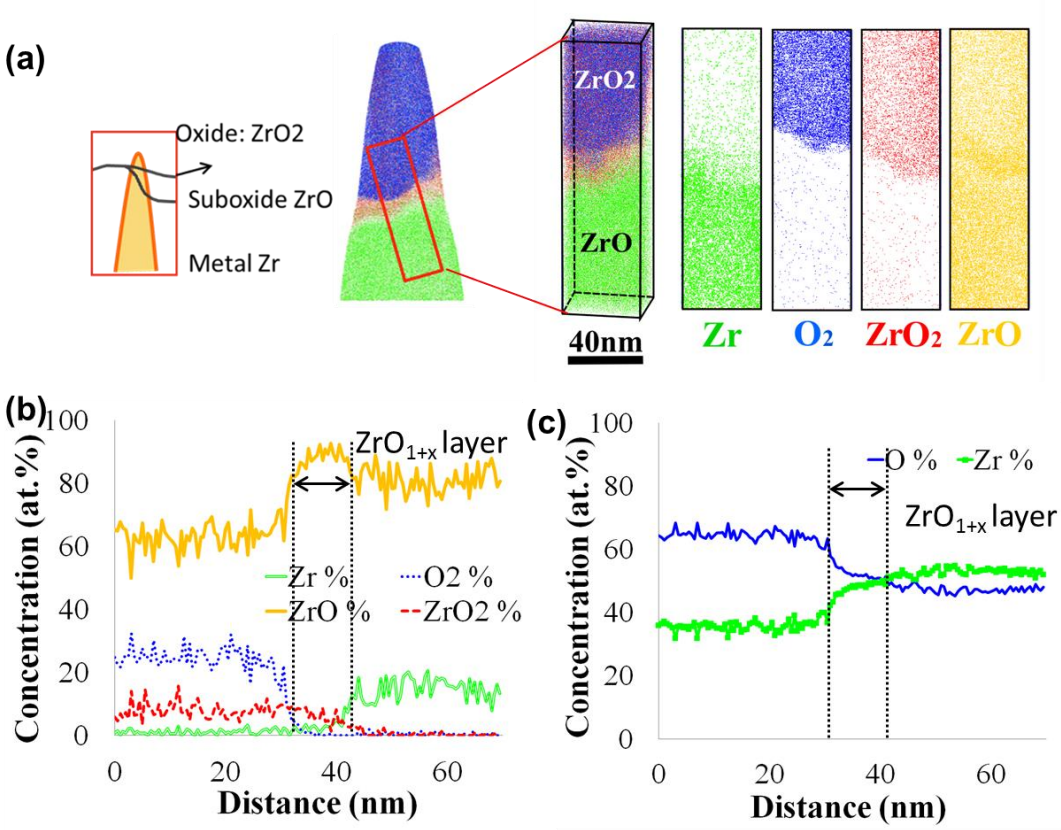

Figure 5.4: (a) 3D atomic maps and 10 nm slices of the APT reconstruction that has ZrO_2 oxide sitting on top of metal; (b)-(c): concentration profiles of (b) ionic species and (c) Zr and O atoms that illustrate the presence of the ZrO_{1+x} layer.

A definite evidence for such an artifact comes from the absence of the ZrO_{1+x} layer when the APT samples were prepared "upside down" so that the "metallic" layer, in this case, ZrO, sit on top of the oxide ZrO_2 as illustrated in Figure 5.5(a). We note that we experienced considerable difficulty analyzing such samples due to the easy fracture of these specimens. Having demonstrated that such ZrO_{1+x} layer was an artifact in some cases, we do not completely exclude that such layer may exist in some location.

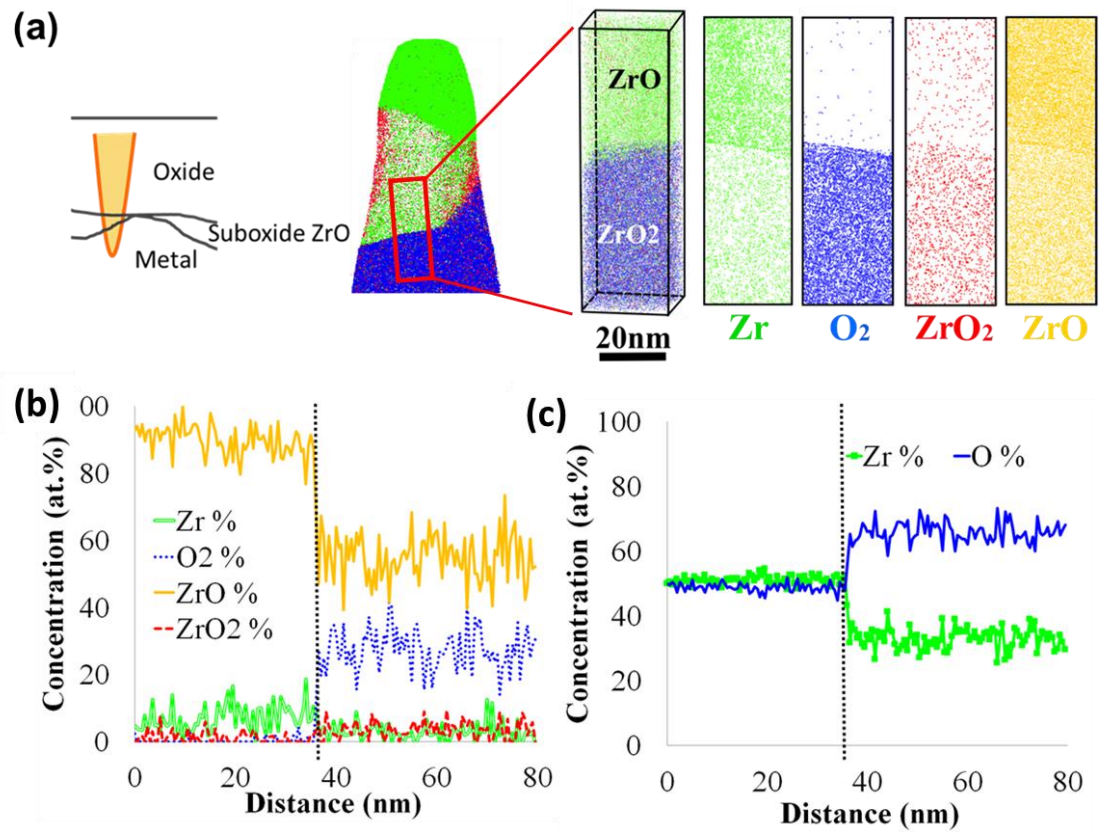

Figure 5.5: (a) 3D atomic maps and 10 nm slices of the APT reconstruction that has ZrO suboxide sitting on top of ZrO_2 oxide; (b)-(c): concentration profiles of (b) ionic species and (c) Zr and O atoms show that the ZrO_{1+x} layer is no longer present.

5.2.5 Crystal Structure of Suboxides

To further determine the crystal structures of the suboxide phases, TEM electron diffraction analysis was conducted on both ZrO and $Zr(O)_{sat}$ phases. As shown in Figure 5.6, grains of ZrO and $Zr(O)_{sat}$ were tilted to low index zone axes, where diffraction patterns were recorded. The diffraction patterns were indexed by calculating the interplanar spacing and the angles

between different crystallographic planes. The grains were tilted to at least two other different zone axes to ensure the indexing is correct.

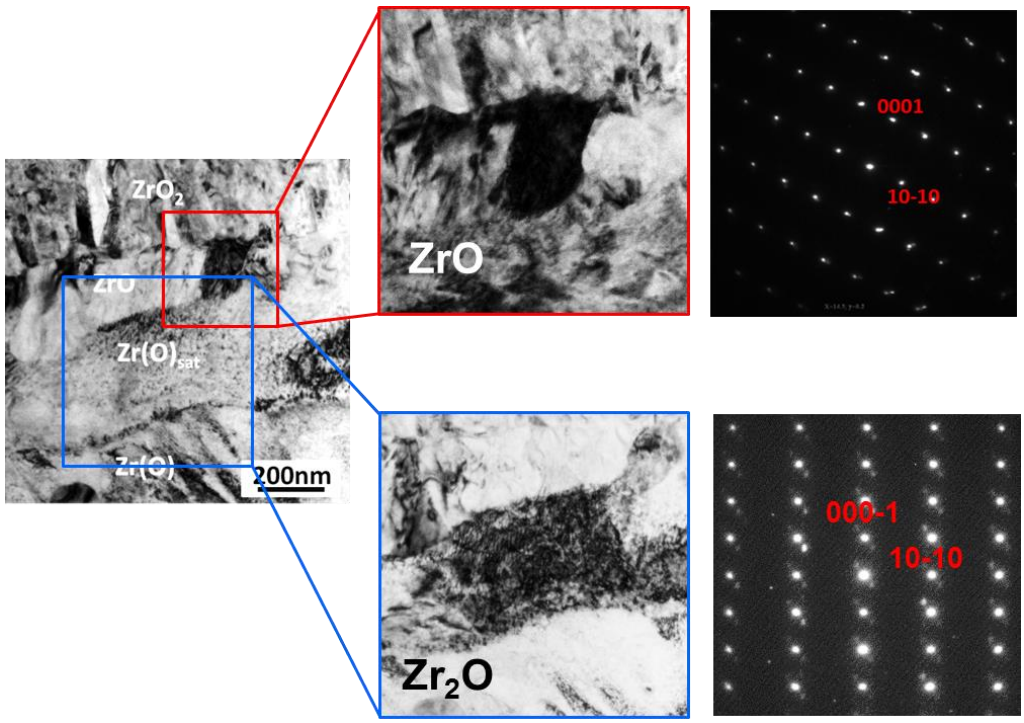

Figure 5.6: TEM bright field images and electron diffraction analysis demonstrating the crystal structures of ZrO and $Zr(O)_{sat}$ suboxide.

According to the diffraction analysis, ZrO exhibited a HCP structure ($P\bar{6}2m$, a = 0.5285 nm, c = 0.3179 nm), which matched the prediction from DFT calculation [43]. In the predicted ZrO structure, any three oxygen atoms that share a Zr neighbor all have their polar axes pointing in different directions. The particular structure could result in strong interactions between the distortions of nearby oxygen and therefore lead to higher stability compared to other possible structures. $Zr(O)_{sat}$, having a stoichiometry close to Zr_2O, adopted the same

parent HCP crystal structure with α-Zr. However, extra diffraction spots indicated the possible ordering of oxygen atoms in the HCP lattice.

5.3 Evolution of Oxide Morphology

While the sequence of phases is similar in the three alloys, the layer thicknesses were quite different from one alloy to another and also showed significant differences at different stages of oxidation. In addition, local variation of layer thicknesses was observed along the oxide/metal interface.

5.3.1 Early Stage of Oxidation

In the initial stage of oxidation (7 days), oxide formed on pure Zr and Zr-Fe-Cr exhibited similar morphologies. As shown in Figure 5.7, the ZrO phase was not present everywhere between the ZrO_2 and $Zr(O)_{sat}$ phases. Instead, small plates of ZrO started to form at the interface between ZrO_2 and $Zr(O)_{sat}$, aligning themselves parallel with each other and growing deeper into $Zr(O)_{sat}$. Crystallographic analysis showed that the ZrO plates nucleated on the $(11\bar{2}0)$ planes of $Zr(O)_{sat}$.

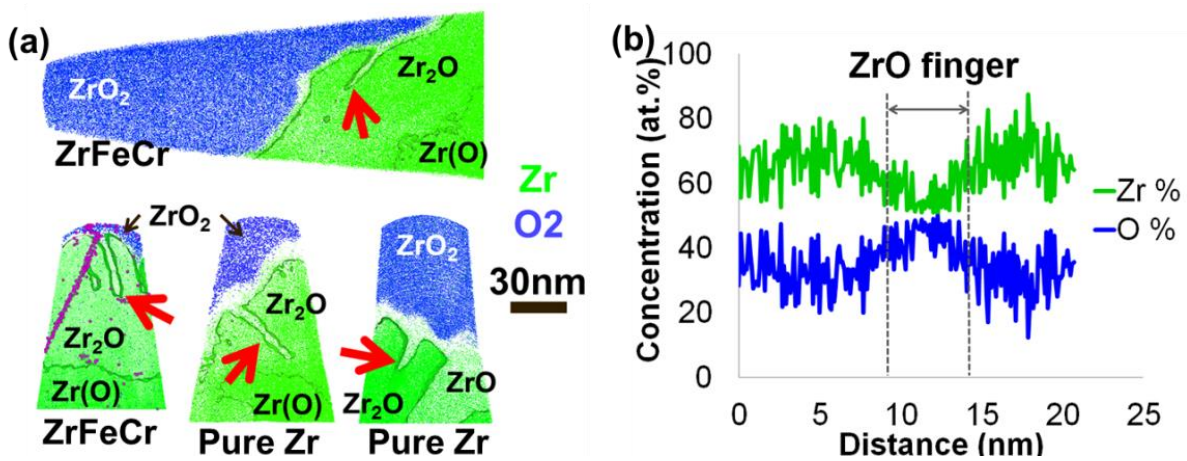

Figure 5.7: (a) 10 nm slices taken from four APT reconstructions showing the nucleation of ZrO plates at the $ZrO_2/Zr(O)_{sat}$ interface; (b) Zr and O concentration profile measured by placing a 10 nm cylinder across the ZrO plate.

5.3.2 Pre- and Post-transition Morphology

At the selected pre-transition time, the ZrO_2/ZrO interface was relatively flat while the interface between ZrO and $Zr(O)_{sat}$ was uneven. The thickness of the ZrO layer varied from 0 to over 80 nm, showing broad semi-elliptical regions of ZrO advancing into a region of $Zr(O)_{sat}$ (Figure 5.8(a)). The $Zr(O)_{sat}$ layer was generally thicker (150-200 nm wide) but also exhibited varied thickness along the oxide/metal interface.

At transition, no ZrO phase was observed (Figure 5.8(b)). However, considering the small volume sampled in the APT specimen, we cannot completely rule out the presence of ZrO layer. After the transition, ZrO phase started to be visible again at the $ZrO_2/Zr(O)_{sat}$ interface

(Figure 5.8(c)), exhibiting similar morphology with early stage samples. This difference in the presence of ZrO phase was likely related to the rate of advance of the oxide front. When the rate of advance was high, any plates and fingers of ZrO which served as precursors of a $Zr(O)_{sat} \rightarrow ZrO$ transformation were quickly consumed by the advancing front, resulting in no ZrO phase was observed at transition. After the transition, the oxidation slowed down and the ZrO phase started to grow again.

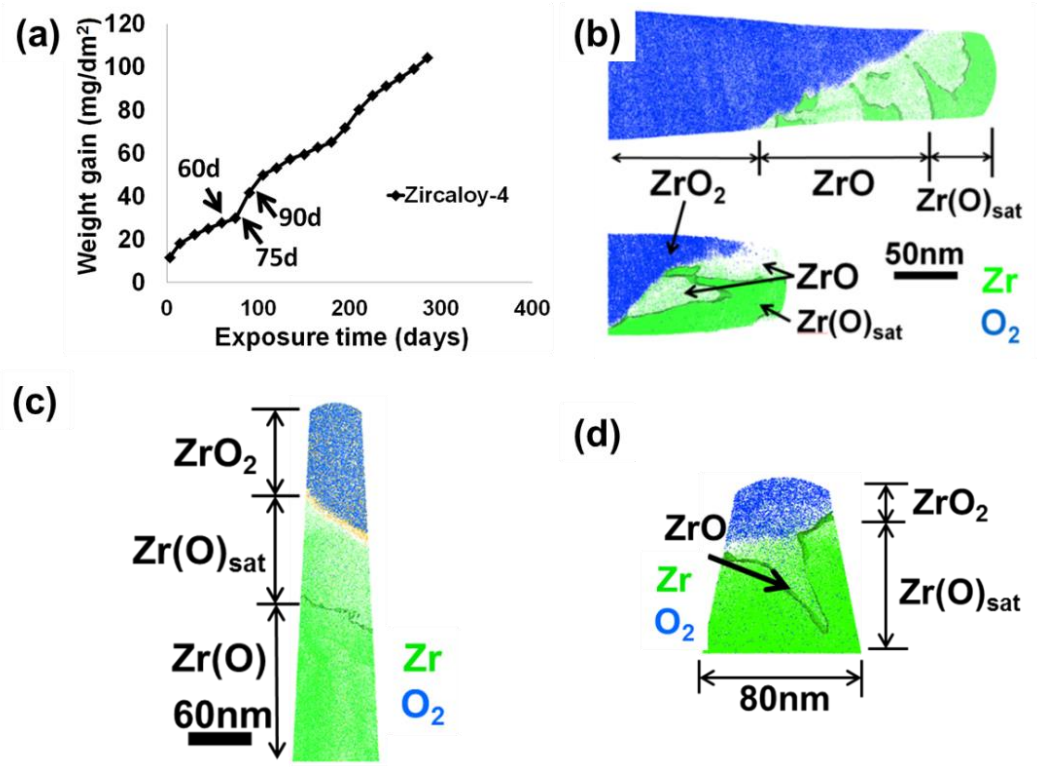

Figure 5.8: (a) Corrosion weight gain curve of Zircaloy-4 where the selected alloy samples are indicated by the arrows; (b)-(d) 10 nm slices taken from three APT reconstructions of (a) 60 days (pre-transition), (b) 75 days (almost at the transition) and (c) 90 days (after the first transition) Zircaloy-4.

5.3.3 Long Term Stable Oxide

In the stable Zr-Fe-Cr alloy, the oxide phase morphology evolved differently compared to pure Zr and Zircaloy-4. After nucleation, the ZrO phase continued growing wider and deeper and eventually formed a continuous layer as shown in Figure 5.9(c) and Figure 5.9(d).

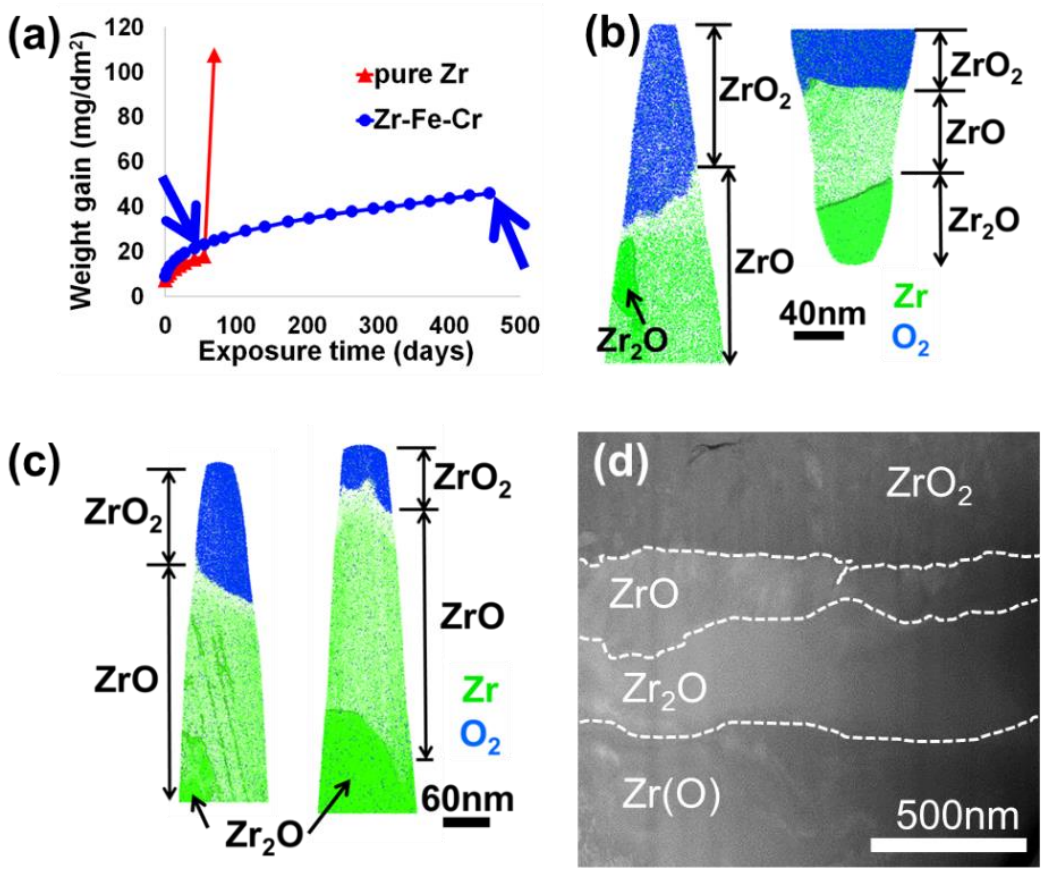

Figure 5.9: (a) Corrosion weight gain curve where the selected alloy samples are indicated by the arrows; (b)-(c): 10 nm slices from APT reconstructions showing the presence of different oxide phases and interface morphologies in (b) 60 days and (c) 456 days Zr-Fe-Cr alloy; (d) STEM-HAADF image from 456 days Zr-Fe-Cr showing the developed suboxides.

5.4 Discussion

5.4.1 Oxide Phases

Oxide evolution in the three alloys showed some similarities. All oxide layers examined showed precursor phases of various oxygen contents. The sequence of phases observed from the oxide water interface to the metal was the same in all alloys, starting with ZrO_2 (corresponding to the traditional oxide layer, which went from the oxide/water interface to the oxide/metal interface), followed by a sequence of suboxide phases in order, as summarized in Figure 5.10.

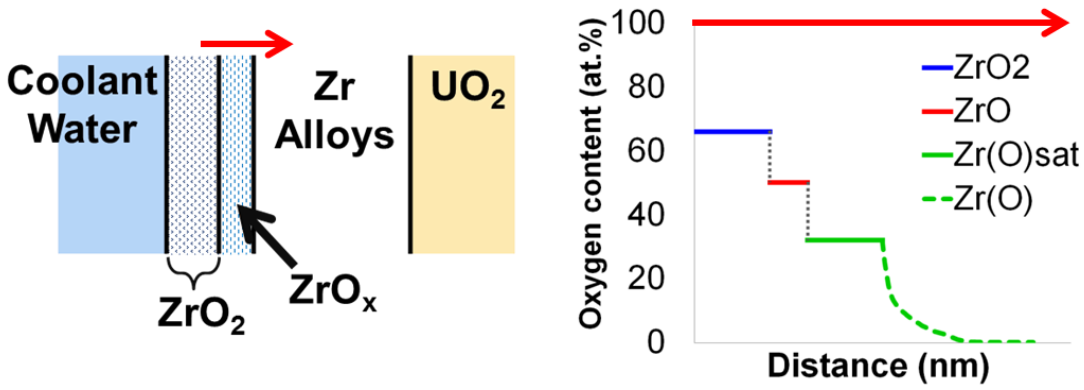

Figure 5.10: Illustration of the oxide phases formed at oxide/metal interface of oxidized Zr alloys and corresponding concentration profiles measure from the water side to alloy side.

The present results were in broad agreement with the literature. Using atom probe tomography and electron energy loss spectrometry (EELS), Hutchinson et al. [81], Ni et al. [70, 167], Hudson [162, 163], and Preuss et al. [52] reported the presence of a ZrO equiatomic

layer on corroded ZIRLO, Zircaloy-2 and Zircaloy-4. Both a FCC (NaCl) crystal structure [66, 135] and a HCP structure [166] have been reported for ZrO. The ZrO layer was not detected in a previous study using microbeam synchrotron radiation diffraction study [56], likely due to insufficient spatial resolution. The presence of the $Zr(O)_{sat}$ layer was observed by Ni et al. [167] and previous examinations by TEM and synchrotron radiation showed a 30% oxygen layer (Zr_3O) ahead of the oxide scale, with different thicknesses in Zircaloy-4, Zr-2.5Nb and ZIRLO [56, 63, 171]. The presence of an ω-Zr phase with 40 at. % O [83] ahead of the oxide front was also reported.

The Zr-O phase diagram at the temperatures and compositions of interest would predict the observation of an equilibrium between a supersaturated solution of oxygen in hcp α-Zr (about 30 at.% O) with monoclinic ZrO_2 [14]. Additional metastable ordered phases in Zr were predicted for lower oxygen content and lower temperatures, representing various arrangements of oxygen in the interstitial sites of the hcp structure. Recent calculations [42] also predicted stable low oxygen ordered phases (Zr_6O and Zr_3O) - which the authors suggested were highly hypothetical - for temperatures below 300 and 350 °C. They also predicted the existence of a line compound Zr_2O ordered phase stable to higher temperatures which does not appear in the phase diagram in Ref [42]. Recent first-principle calculations identified a stable ZrO phase and determined that a phase with a Zr_2O stoichiometry (and thus close to the $Zr(O)_{sat}$ phase predicted by the phase diagram as the solubility limit of O in Zr)

formed by oxygen ordering within the hcp Zr sublattice with a range of oxygen concentration [43].

The present observations with the sequence of $Zr(O)_{sat}$, ZrO, and ZrO_2, could therefore correspond to thermodynamic equilibrium of the two-component Zr-O mixture above the stability range of the low oxygen ordered phases, with $Zr(O)_{sat}$. We should note, however, that because phase formation and evolution at the oxide front in the present conditions is governed not only by thermodynamics but also by kinetics, the studies mentioned above provide only a qualitative guideline of what could be observed.

5.4.2 Oxide Morphology

The layer thicknesses were quite different from one alloy to another and change significantly at different stages of oxidation. Pure Zr exhibited the thinnest ZrO and $Zr(O)_{sat}$ layers, both of which do not thicken over time. Zircaloy-4 had distinct layers of ZrO and $Zr(O)_{sat}$ of thicknesses of the order of 100 nm at pre-transition regime but largely disappear when transition happens. The evolution of oxide phase morphologies in Zircaloy-4 is summarized in Figure 5.11.

For the pre-transition samples, the sub-oxides were of variable thicknesses and did not form continuous layers. The layer of ZrO observed by APT varied in thickness from 0 to over 80

nm with semi-elliptical morphologies. The $Zr(O)_{sat}$ layer was thicker (150 to 200 nm wide). However significant variations of the width were also observed and this layer may not be continuous along the oxide/metal interface. At transition, the ZrO layer almost disappeared. Small ZrO plates were occasionally observed in post-transition Zircaloy-4. The oxygen-saturated layer was not as wide as in the pre-transition samples (~ 30-60 nm) and the oxygen concentration decreased steeply into the metal (10 at. % 100 nm away from the oxide/metal interface). In the Zr-Fe-Cr alloy, once the ZrO phase nucleated, it continued growing wider and deeper to eventually form a continuous layer (Figure 5.12).

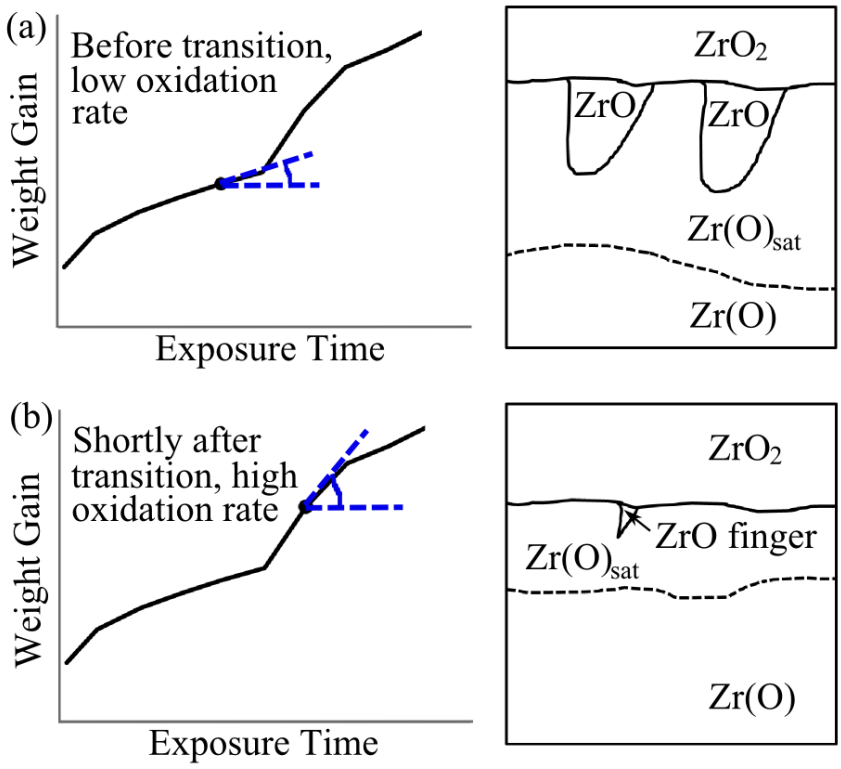

Figure 5.11: Schematic illustration of oxygen containing phases present at metal/oxide interface in (a) pre-transitioned (b) post-transitioned samples.

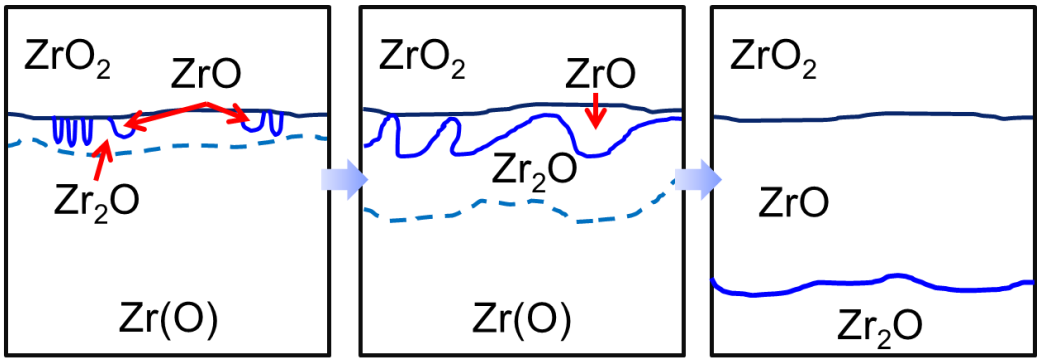

Figure 5.12: Schematic illustration of oxide phases evolution in the Zr-Fe-Cr alloy.

The present results were in broad agreement with the literature. The observed ZrO phase was reported by Ni [70] using atom probe tomography and electron energy loss spectrometry (EELS) and by Hu [134] and Garner [166] using transmission backscattered electron diffraction. The large thickness variation of ZrO layer agreed with Tejland's work [140, 168] and added more evidence that the transition happens locally along the interface. By comparing the thickness of suboxide phases, we found that the lower the corrosion rate (derivative of the weight gain curve) at the point where the sample was collected, the thicker the suboxide layer, or alternatively, the more oxygen can diffuse ahead of the oxide.

The question about how the oxygen that diffused ahead of the main oxide front and formed the intermediate phase observed affected the corrosion behavior of the material remained. Clearly the fact that some oxygen was used to form the layers, rather than forming stoichiometric ZrO_2 would cause a slight slowing down of oxide formation. However, this effect was small, since the total oxygen content in these layers was small compared to the

overall oxygen content in the stoichiometric oxide. Also, since the sequence of phases appeared to depend mostly on the stage of corrosion, it is likely that these layers were *consequences* rather than *causes* of the pre-transition corrosion behavior. Concerning the oxide transition, as the oxide grew, stresses accumulated, which may be partly relieved by plastic deformation of the metal. Since the oxygen could harden the metal region next to the oxide front, the plasticity of the Zr matrix may be hampered, which would make the accommodation of stresses induced into the matrix by oxide growth (normally done by plastic deformation usually by creep) more difficult. Thus the presence of the oxygen rich layers could accelerate stress accumulation in the oxide and thus accelerate in turn the onset of the oxide transition or possibly cause corrosion breakaway.

5.5 Summary

In this chapter, both TEM and APT were utilized to study the structure and morphology of different oxide phases that were present at the interface. Oxide formation in the three alloys showed similarities. The sequence of phases observed from the oxide water interface to the metal was the same in all alloys, starting with ZrO_2 (corresponding to the traditional oxide layer, which went from the oxide water interface to the oxide metal interface), followed by a sequence of suboxide phases. The slight variation in O concentration in ZrO could be a field

evaporation artifact during APT data collection, but we do not completely exclude that the ZrO_{1+x} layer may exist in some locations. While the sequence of phases was similar in the three alloys, the layer thicknesses were quite different from one alloy to another and from one stage of the corrosion process to another. In general, the lower the corrosion rate (derivative of the weight gain curve) at the point where the sample was collected, the thicker the suboxide layer, or alternatively, the longer oxygen can diffuse ahead of the oxide. This may be interpreted by considering that the ZrO_2 scale consumed the suboxide layers as it advanced, therefore the faster the oxide growth, the thinner the suboxide scale.

CHAPTER 6

Oxide Texture Development

6.1 Overview

It is believed that the oxide fails when the stress accumulated in the oxide causes interconnected cracking and porosity [47, 63, 73, 134, 166, 189]. The formation of growth stress is due to the volume difference between the oxide and the metal from which the oxide is formed [190]. In the case of the ZrO_2 oxide layer growing on top of Zr, the compressive stress in the oxide is induced by the differences between the surface areas that the metal ion occupies in the oxide and in the substrate. Hence stress is minimized when oxide grains align $(\bar{6}01)$ (close to (200)) planes close to the oxide metal interface, referred as "fiber texture", a texture in which the unit cell of ZrO_2 occupies smallest area at the metal/oxide interface [165]. The fiber texture was reported in a variety zirconium alloy system where $(\bar{3}01)$ to $(\bar{5}01)$ planes are aligned in parallel to the alloy surface [56, 63, 71-73] whereas other researchers observed a few epitaxial orientation relationships between oxide and metal grains [66, 69, 70].

Yet how the oxide develops its texture and whether the texture evolution is playing a role in affecting oxide kinetics remains unclear.

In this chapter, the texture evolution of pure Zr and the Zr-Fe-Cr alloy was examined by a multiscale characterization approach combining SEM, FIB, and TEM. The oxide growth in pure Zr was unstable; resulting in penetration of oxide dendrites along metal grain boundaries and loss in oxide protectiveness. The Zr-Fe-Cr alloy, on the other hand, exhibited stable oxide growth and no breakaway during the whole duration of the test (500 days). The observed differences in oxide grain texture between two alloys could shed lights on how the oxide grain texture impacts the protective character of oxide phases and onset of oxide breakaway.

6.2 Oxide Texture at Early Stage of Oxidation

6.2.1 Oxide/Metal Interface

At the initial stage of oxidation, the oxide layer on pure Zr and the Zr-Fe-Cr alloy both showed grain-to-grain variations in thicknesses. Faster ingress of the oxide front along grain boundaries was observed in pure Zr but not in the Zr-Fe-Cr alloy (Figure 6.1). A higher number of cracks were present in pure Zr than the Zr-Fe-Cr alloy.

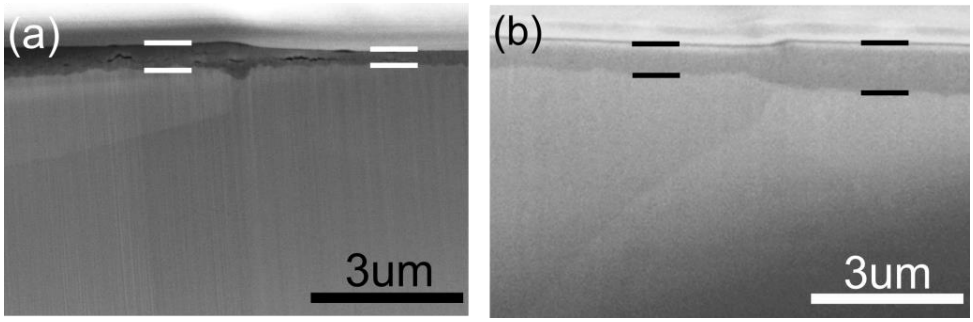

Figure 6.1: SEM images of (a) 1 day pure Zr and (b) 7 days Zr-Fe-Cr alloy showing the grain to grain variation in oxide thickness. Preferential oxidation along grain boundary was only visible in pure Zr in (a).

The orientation dependence of the ZrO_2 oxide thickness was evaluated by combining dual beam milling/imaging and EBSD orientation mapping technique. We collected over 40 sets of orientation and thickness data on pure Zr oxidized for 1 day and 7 days, Zircaloy-4 oxidized for 7 days and Zr-Fe-Cr alloy oxidized for 7 days. The thickness of the ZrO_2 oxide layer above each grain was measured separately from the SEM images (Figure 6.2(a)). Considering the local variation of oxide layer, six to eight point measurements were taken from oxide formed on top of each grain. The measurements were taken in the middle part of the grain to avoid the effects from grain boundary oxidation. We note that the oxide measured here is only ZrO_2 as the sub-oxides were not visible in the SEM images. The crystallographic orientation of each grain was quantified by measuring angle between the [0001] direction of metal grain and the oxide growth direction (which was perpendicular to the oxide/metal interface) from the EBSD data as illustrated in Figure 6.2.

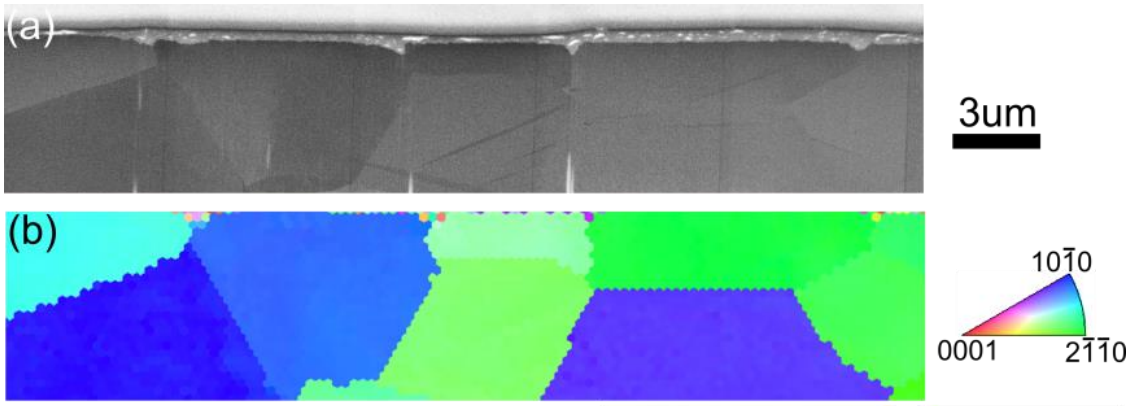

Figure 6.2: (a) SEM image and (b) inverse pole figure (IPF) map that illustrate the correlation between oxide (ZrO_2) thickness and orientation of metal grain beneath.

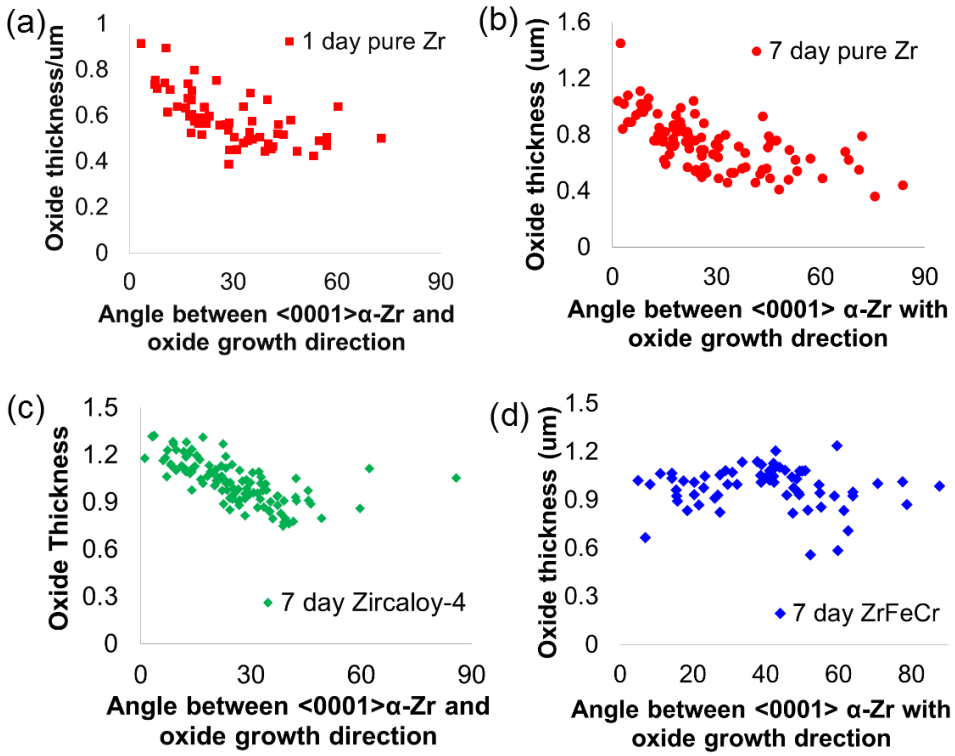

Figure 6.3: ZrO_2 oxide thickness plotted as a function of substrate grain orientation. In (a) 1 day pure Zr, (b) 7 days pure Zr and (c) 7 days Zircaloy-4, the oxide was thicker when the (0001) plane of alloy matrix was more parallel to the oxide/metal interface; whereas the oxide thickness was independent of metal grain orientation in (d) 7 days Zr-Fe-Cr alloy.

The orientation dependence of the ZrO_2 oxide thickness is shown in Figure 6.3. In pure Zr and Zircaloy-4, the oxide thickness increased when advancing along metal grains that have basal planes aligned more parallel to the oxide/metal interface, while the oxide growth rate in the Zr-Fe-Cr alloy appeared to be independent of orientation.

6.2.2 Oxide Formed on Pure Zr

The general morphology of the oxide layer on pure Zr oxidized for 1 day is illustrated in Figure 6.4. The oxide layer consisted of a very thin layer of equiaxed grains (30 to 80 nm thick) and underlying columnar grains. The equiaxed grains were 10-30 nm in diameter. The columnar grains, separated by large horizontal cracks, are around 20-50 nm wide and 100-150 nm long. Vertical cracks were observed on the surface of the oxide formed on top of metal grain boundaries (Figure 6.5).

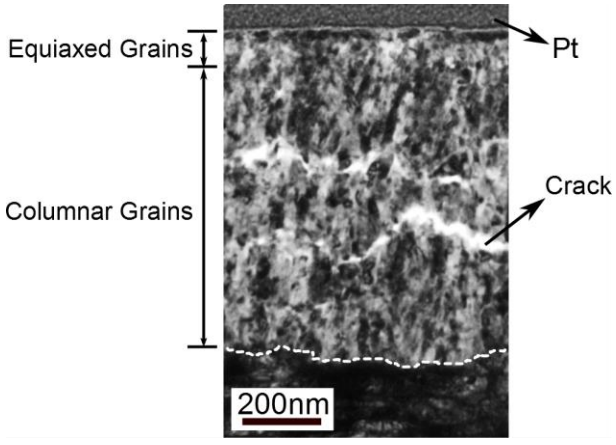

Figure 6.4: TEM bright field image of the oxide layer formed in 1 day pure Zr.

To examine the oxide texture, we tilted the metal grains to their $[\bar{1}2\bar{1}0]$ zone axes and recorded the electron diffraction patterns of the metal grains and oxide grains. Interestingly, even though the oxide layer consisted of a large numbers of nano-sized grains, the majority of the grains showed very similar orientation, producing a spot diffraction pattern as shown in Figure 6.5. Both equiaxed and columnar grains shared the same orientation relationship with underlying metal grain, where the $(10\bar{1}1)$ plane of α-Zr formed a ~5 ° angles with (002) plane of the monoclinic ZrO_2. No tetragonal ZrO_2 was observed in the foil examined.

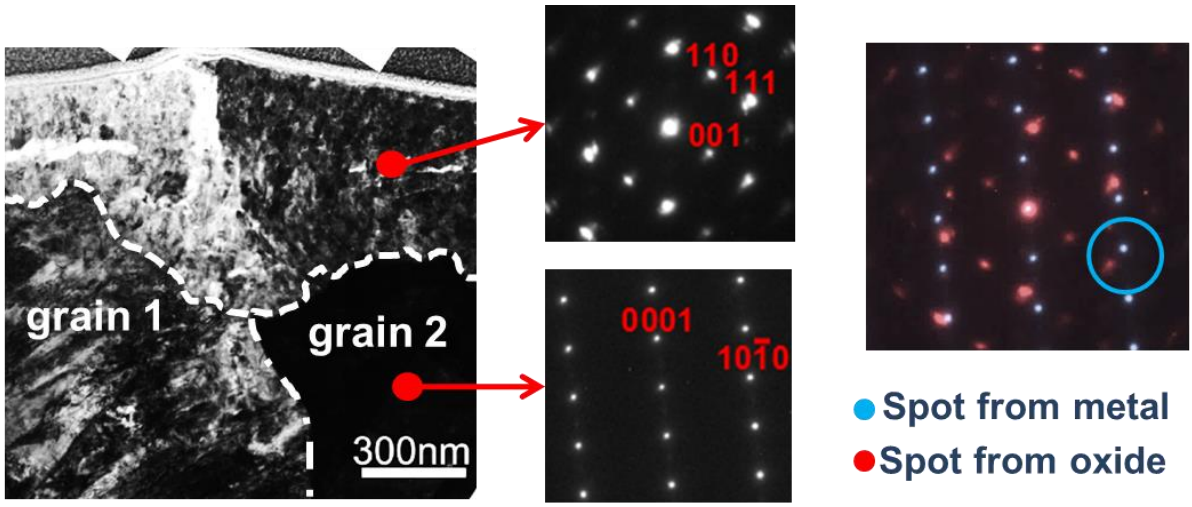

Figure 6.5: TEM bright field image and electron diffraction patterns showing the orientation relationship between oxide and metal grains in 1 day pure Zr.

The oxide grains in pure Zr oxidized for 7 days exhibited same grain morphology. The same orientation relationship between monoclinic ZrO_2 and Zr metal was observed near surface while additional orientation relationships were occasionally found when moving selective aperture toward oxide/metal interface:

$$(10\bar{1}1)_{\alpha-Zr} \parallel (\bar{1}11)_{m-ZrO2}$$

$$(10\bar{1}1)_{\alpha-Zr} \parallel (111)_{m-ZrO2}$$

$$(10\bar{1}1)_{\alpha-Zr} \parallel (200)_{m-ZrO2}\ or\ (020)_{m-ZrO2}$$

Note here that the d-spacing of (200) and (020) was too close to each other to be distinguished by electron diffraction.

6.2.3 Oxide Formed on the Zr-Fe-Cr Alloy

The oxide grains formed on the Zr-Fe-Cr alloy were cohesive with much fewer cracks visible in TEM image (Figure 6.6). Similar with pure Zr, both small equiaxed grains and columnar grains were observed. The layer of equiaxed grains extended from 150 to 300 nm in thickness, which were much thicker compared to the equiaxed grain regions formed in pure Zr. The oxide grain texture in the Zr-Fe-Cr alloy also varied from that in pure Zr. The equiaxed grains that nucleated at the beginning formed a few orientation relationships with metal underneath. One of the orientation relationships we have identified was

$$(10\bar{1}1)_{\alpha-Zr} \parallel (200)_{m}\ or\ (020)_{m}$$

The orientation relationship was visible in Figure 6.6 and was consistent with the orientations identified in pure Zr oxidized for 7 days. Other than monoclinic phase, tetragonal ZrO_2 grains were occasionally observed in the layer of equiaxed grains.

When oxide grew thicker, columnar grains started to dominate. The oxide grains changed their crystallographic orientation as oxide advanced further into the metal, aligning $[200]_m$ poles parallel to the oxide growth direction regardless of the orientation of the underlying metal grain. The diffraction spot of $(200)_m$ was not visible in Figure 6.6, likely a result of the tilting condition not satisfying the Bragg condition for $(200)_m$ planes. However, the orientation of $(111)_m$ plane indicated that the $[200]_m$ direction in this case should run parallel to the oxide growth direction.

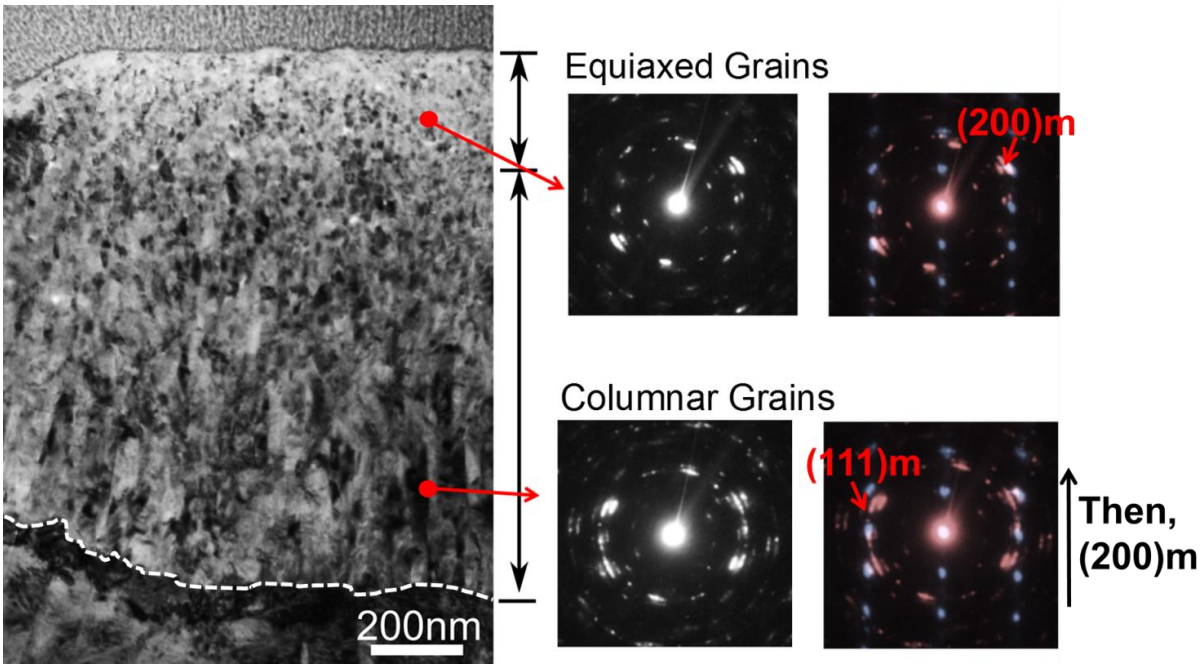

Figure 6.6: TEM bright field image and electron diffraction patterns showing the evolution of grain texture of oxide formed on 7 days Zr-Fe-Cr alloy.

6.3 Long term oxidation

6.3.1 Oxide/metal interface

In the long term oxidized pure Zr (55 days), the oxide layers still showed significant variations in thickness from grain to grain. The SEM image in Figure 6.7(a) also reveals that the oxide ingress along grain boundaries observed in pure Zr oxidized for short times developed into oxide dendrites that were penetrating farther along metal grain boundaries. Large horizontal cracks were also developed in the oxide layer of pure Zr.

In the Zr-Fe-Cr alloy that was oxidized for 55 days, the differential grain-to-grain growth was no longer present. The oxide/metal interface became relatively flat. No faster growth of oxide along metal grain boundaries was visible in SEM image (Figure 6.7(b)).

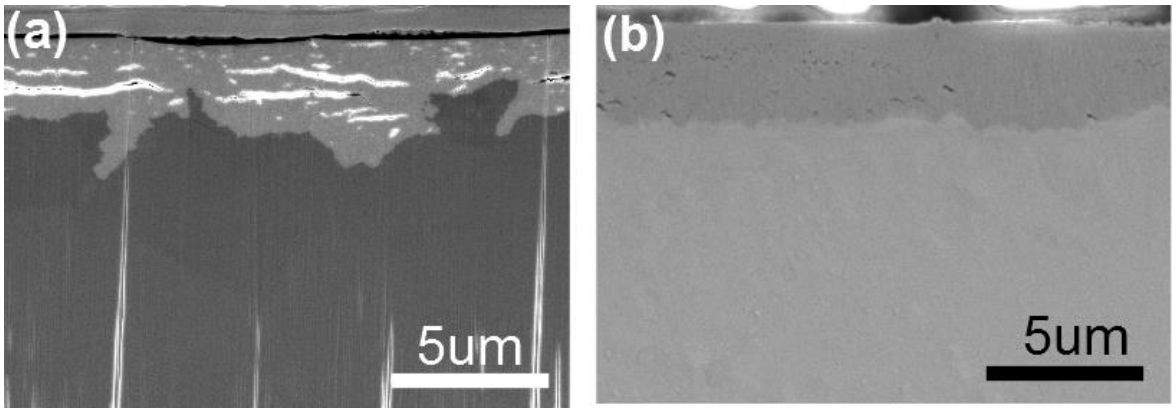

Figure 6.7: SEM images (a) 55 days pure Zr and (b) 55 days Zr-Fe-Cr showing the different oxide/metal interface morphology.

6.3.2 Oxide Texture

The oxide texture in the alloy samples oxidized for long time (>55 days) was characterized by the XRD pole figures as shown in Figure 6.8. The formation of the fiber structure in the Zr-Fe-Cr alloy was confirmed by XRD pole figures as shown in Figure 6.8(c) and Figure 6.8(d). In pure Zr, the intensity distribution of (200) and $(\bar{1}11)$ poles was different from that in fiber texture. Also, high intensity regions of (200) and $(\bar{1}11)$ poles were overlapped, which indicated the orientation relationships observed were partially maintained.

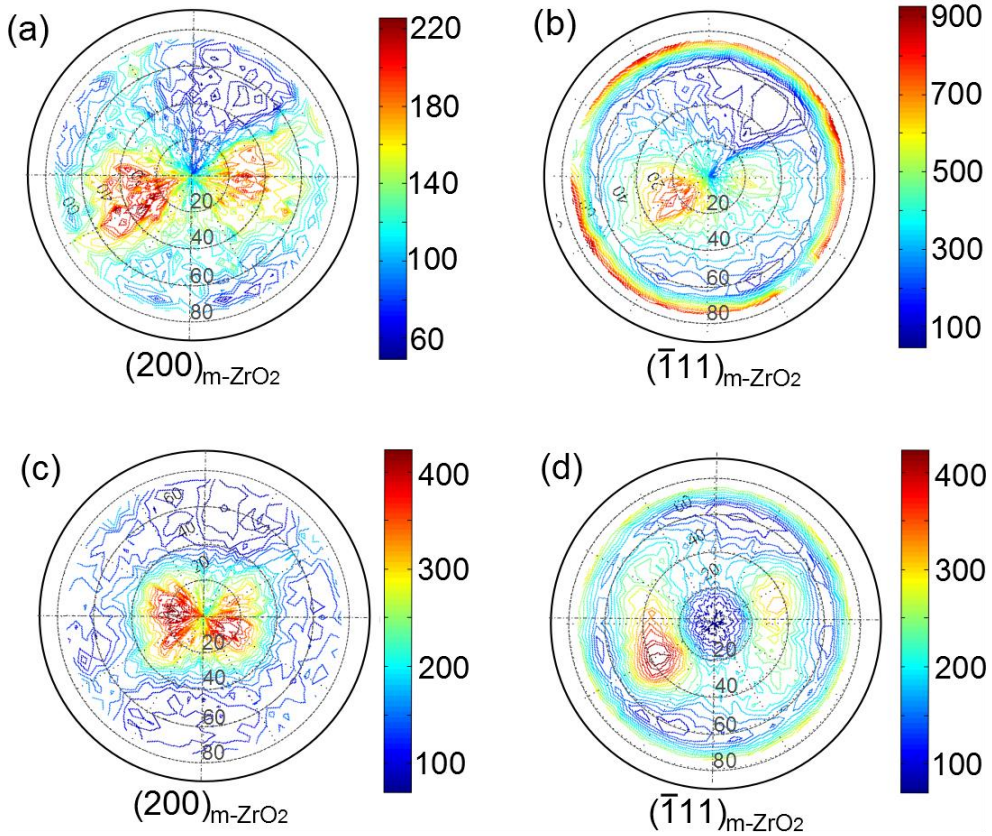

Figure 6.8: XRD pole figures of (a) $(200)_{m\text{-}ZrO2}$ and (b) $(\bar{1}11)_{m\text{-}ZrO2}$ poles of 55 days pure Zr; (c) $(200)_{m\text{-}ZrO2}$ and (d) $(\bar{1}11)_{m\text{-}ZrO2}$ poles of 456 days Zr-Fe-Cr alloy.

Three regions with different grain morphologies were identified in the TEM image of the Zr-Fe-Cr alloy oxidized for 456 days (Figure 6.9): a layer of small equiaxed grain (150 to 300 nm thick), a layer of small, short columnar grains (300 to 500 nm thick) and well aligned long, large columnar grains. The equiaxed grains exhibited orientation relationships with the metal substrate, as discussed in section 6.2.3. In the smaller, shorter columnar grain region, the oxide grain orientation gradually transitioned to the fiber texture. The oxide grains in this region were 20 to 50 nm wide and 100 to 250 nm long. The large columnar grains, which were on average 30 to 80 nm wide and 400 to 500 nm long, exhibited a fully developed fiber texture.

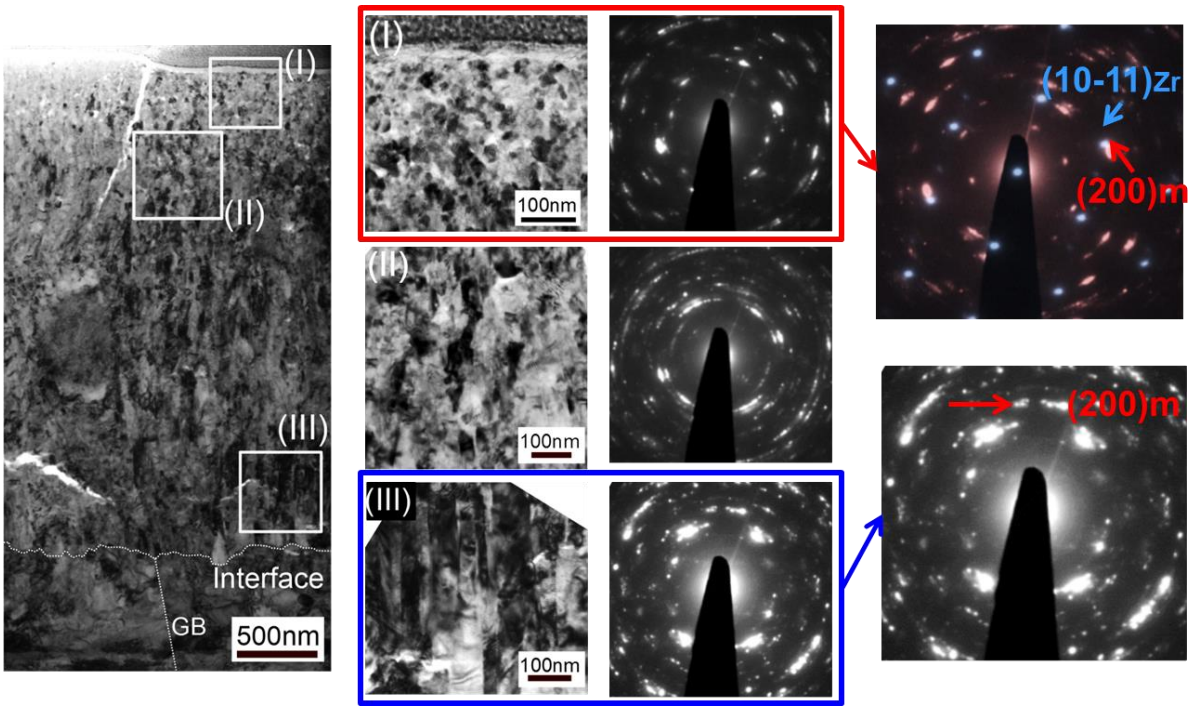

Figure 6.9: TEM bright field image and electron diffraction patterns showing the evolution of grain morphology and grain orientations of the oxide formed on 456 days Zr-Fe-Cr alloy.

6.4 Discussion

We observed an increase in the ZrO_2 oxide thickness when the basal plane of the metal grains was more parallel to the oxide/metal interface in pure Zr while the growth rate in the Zr-Fe-Cr alloy appeared to be independent of orientation. The difference can be rationalized by the preferred crystallographic orientation between Zr and ZrO_2 in pure Zr. The grain texture and grain morphology of oxide layer formed on the two alloys are schematically illustrated in Figure 6.11. In both alloys, the oxide layer consisted of surface equiaxed grains and underlying columnar grains. A thicker layer of equiaxed grains was present in the Zr-Fe-Cr alloy.

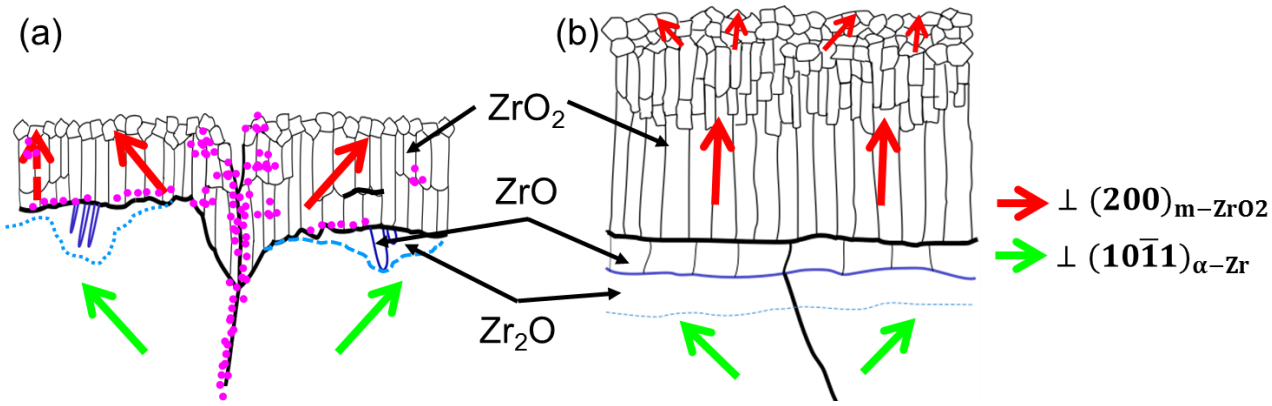

Figure 6.10: Schematic illustration of grain morphology and texture of oxide developed in (a) pure Zr and (b) the Zr-Fe-Cr alloy.

In pure Zr, oxide grains formed a well-defined orientation relationship with underlying metal grain at the early stage of oxidation. The orientation relationship might introduce variations in growing stress for oxide that form on top of different metal grains and therefore give rise to

different oxide thickness. The orientation relationship were maintained at least for the top ~700 nm with additional orientation relationships starting to occur when the oxide grew thicker, producing a lower portion of oxide grains that had preferred orientation [56, 63, 71-73] in the sample oxidized for long time. Because the oxide grains formed preferential orientation with respect to metal grain, the oxide grain boundaries above metal grain boundaries were likely to be high angle grain boundaries, which were more susceptible to oxygen ingress and led to the formation of oxide dendrites along the metal grain boundaries.

In the Zr-Fe-Cr alloy, oxide grains formed a few possible orientation relationships with the underlying metal at the beginning and quickly adopted a fiber texture where the [200] of monoclinic ZrO_2 lied close to the oxide growth direction. The evolution of oxide grain orientation agreed to the two-stage growth model proposed by Li et al. [165] and the fiber structure was consistent with previous work on similar alloys [56, 63, 71-73]. Since the loss of protectiveness of the oxide has been demonstrated to be highly correlated with stress developed within the oxide [47, 63, 73, 134, 166, 189], the fiber texture could minimize the stress accumulated in the oxide layer and therefore was more preferred texture for improved corrosion resistance.

The difference in oxide texture indicated that the oxide nucleation and growth in the two alloys may be governed by different mechanisms. Previous study by Garner et al. suggested that tetragonal ZrO_2 formed first and then transformed to favorably oriented monoclinic

grains [134]. Since it was reported that Fe and other transition metals stabilize the tetragonal phase [56, 93], it was possible that the tetragonal phase was less likely to form in pure Zr due to lack of alloying elements as observed by Kim el al. [191]. Unfortunately, observation of the tetragonal phase through TEM has proven difficult as tetragonal grains relax to the monoclinic phase during the preparation of electron transparent TEM foils [65].

6.5 Summary

This chapter presented the observations of oxide grain texture and grain morphology in pure Zr and the Zr-Fe-Cr alloy. The observed oxide texture was different in the two alloys, which can be correlated with differences in the oxide growth.

- In pure Zr, nano-sized oxide grains formed an orientation relationship with underlying metal grains. As a result of the preferential orientation, the oxide grain boundaries formed above a metal grain should be low angle grain boundaries while the oxide grain boundaries on top of a metal grain boundary were high angle grain boundaries. The formation of significant high angle oxide grain boundaries could make the metal grain boundary more susceptible to oxygen ingress and eventually led to the formation of oxide dendrite.

- In the Zr-Fe-Cr alloy, where oxide growth was stable, oxide grains quickly adopted a fiber texture where the (200) plane lied close to oxide/metal interface.

It appeared that the fiber texture was beneficial to a more stable oxide growth, as in the Zr-Fe-Cr alloy. However, the reason why the two alloys developed different oxide textures remained unclear. Previous work speculated that tetragonal ZrO_2 is likely to be the precursor for the fiber structure [134, 149]. Given that the tetragonal phase can be stabilized by alloying elements, the alloying elements present near oxide/metal interface may play a role on the oxide texture development. The distribution of solutes will now be evaluated.

CHAPTER 7

Solute Distributions near the Oxide Scale[2]

7.1 Overview

Alloying elements are added into pure Zr to improve the overall corrosion resistance. Previous work speculated that elements have lower valance state (such as Fe^{2+} or Fe^{3+}) than Zr^{4+} could generate extra oxygen vacancies and accelerate the electron transport [192]. However, it failed to explain why the Zr-Fe-Cr alloy with higher Fe concentration exhibited a much more stable oxide growth compared to pure Zr. The solute distributions may affect the oxide growth in two possible ways:

(i) Solutes incorporated into growing oxide can generate/consume oxygen vacancies and affect the electron conduction and oxygen ingress;

[2] The content of this chapter includes the following article:
[1] Y. Dong, A. T. Motta, and E. A. Marquis, "Atom probe tomography study of alloying element distributions in Zr alloys and their oxides," Journal of Nuclear Materials, 2013 (442) p. 270-281.

(ii) Solutes rejected from oxide front can redistribute to different microstructural sites and affect the nucleation of new grains formed at the oxide front.

In this chapter, we primarily investigated the distribution of Sn, Fe, and Cr in the regions next to oxide front and within the oxide layer. To characterize the solute distribution, which may exhibit low levels of enrichment (a few atomic percent) at an extremely fine scale, APT is the most suitable technique to use. Considering that one APT needle can only sample a very small volume from the alloy, APT specimens were prepared from several regions on the alloy sample to ensure good statistics.

7.2 Solute Distribution next to the Oxide Front

The distribution of alloying elements in the metal region next to the oxide, where significant oxygen diffusion had occurred, was different from that in the bulk of the material. This is reasonable since the phase equilibria should be altered by the presence of oxygen.

7.2.1 Pure Zr

Within the suboxide and solid solution regions, Fe was found to segregate to the interface between ZrO_2 and underlying suboxides/solid solution, to linear features (possibly

dislocations), and to grain boundaries in $Zr(O)_{sat}$ and the solid solution region. Two APT reconstructions that exhibited markedly different Fe enrichment at interface and near oxide front were selected and compared in Figure 7.1. It was evident from the atomic mapping that the amount of Fe segregation at interface varies significantly when moving along the interface, ranging from zero to up to 1.5- 2 at. % (Figure 7.1 (a),(b) and (d)).

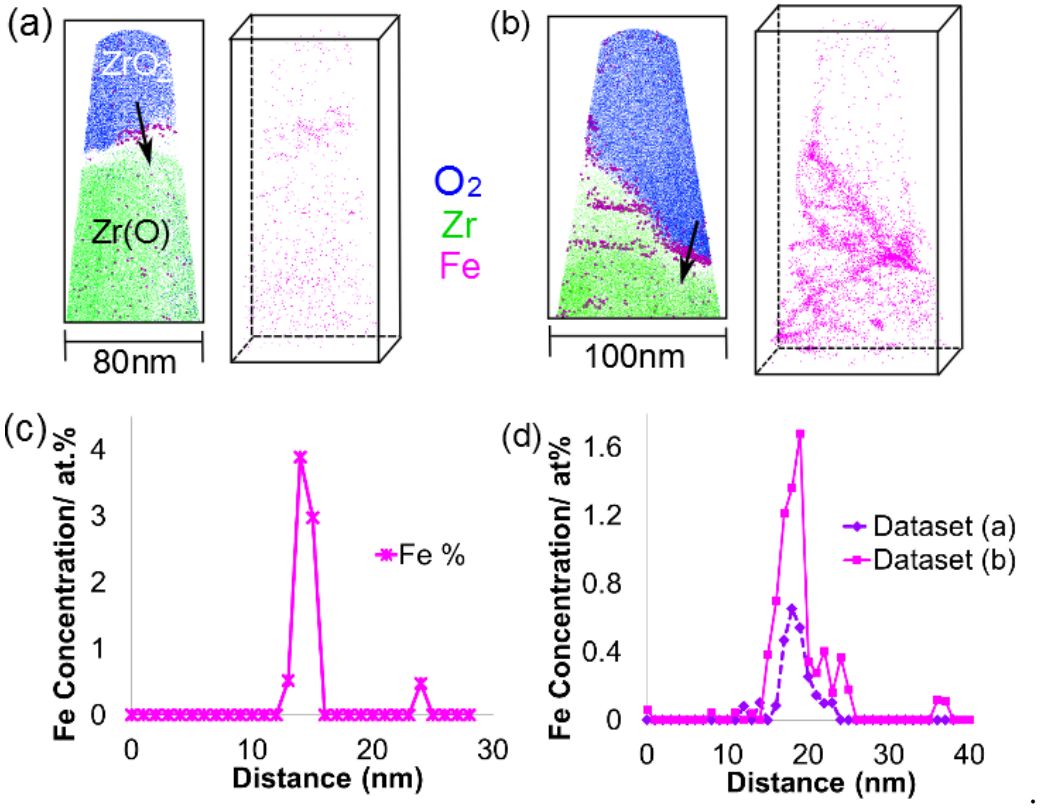

Figure 7.1: Pure Zr near oxide region: (a) and (b) present 10 nm slices (left) and 3D Fe maps (right) from two representative APT datasets that illustrate the Fe distribution; (c) Fe concentration profile measured by placing an 10 nm cylinder across an observed Fe-decorated dislocation in (b); (d) Fe concentration profile measured by placing 10 nm cylinders along the arrows indicated in (a) and (b).

High density of Fe decorated dislocations were observed in the suboxide and solid solution regions in Figure 7.1(b); whereas no dislocations were visible in Figure 7.1(a). Since Fe has very limited solubility in α-Zr, the Fe concentration in the solid solution were utilized to assess the total amount of Fe enrichment on dislocations. As seen in Table 7.1, Fe concentration in solid solution of pure Zr varied markedly from dataset to dataset, ranging from below detection limit (0.003 at. %) to 0.065 at. %

Table 7.1: Fe concentration (at. %) measured in solid solution and ZrO_2 oxide. Errors were calculated from dataset to dataset variations and counting statistics within each dataset.

	Total # of ions	Fe content in solid solution	Fe content in ZrO_2
Pure Zr	93.5 million	0.02±0.02	0.05±0.05 Matrix: 0.01±0.01 Near GB: 0.14±0.01
Zr-Fe-Cr	76.1 million	0.05±0.02	0.03±0.01

Fe also segregated to the grain boundary in the suboxide $Zr(O)_{sat}$ and solid solution. The amount of segregation, as shown in Figure 7.2(b), was at similar level with the Fe segregation on grain boundaries in the base alloy (far away from the oxide scale). The oxygen level in Figure 7.2(c) was higher at the grain boundary, indicating possible preferential grain boundary oxidation in pure Zr.

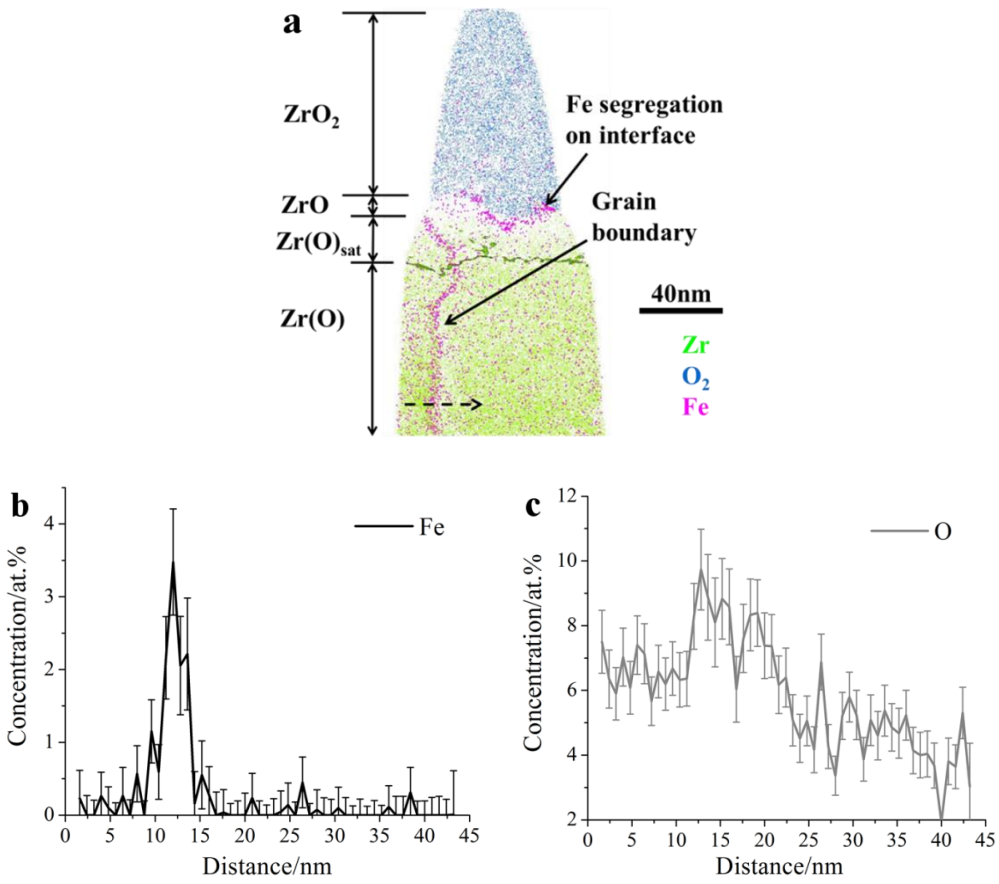

Figure 7.2: Pure Zr near oxide region: (a) 10 nm slice from an APT reconstruction showing the Fe segregation to grain boundary; (b) and (c) concentration profiles measured by placing a 10 nm cylinder across the grain boundary along the dashed arrow indicated in (a).

7.2.2 Zircaloy-4

The distribution of alloying elements in the oxygen rich region of the metal was more complicated in Zircaloy-4 than in pure Zr. In the $Zr(O)_{sat}$ region adjacent to ZrO suboxide, Fe and Cr-rich fine clusters were occasionally observed (Figure 7.3(a), (b)). Fe was also found to

segregate to linear features, possibly dislocations, formed in the region near the oxide metal interface which was plastically deformed by the growing oxide (Figure 7.3(a)).

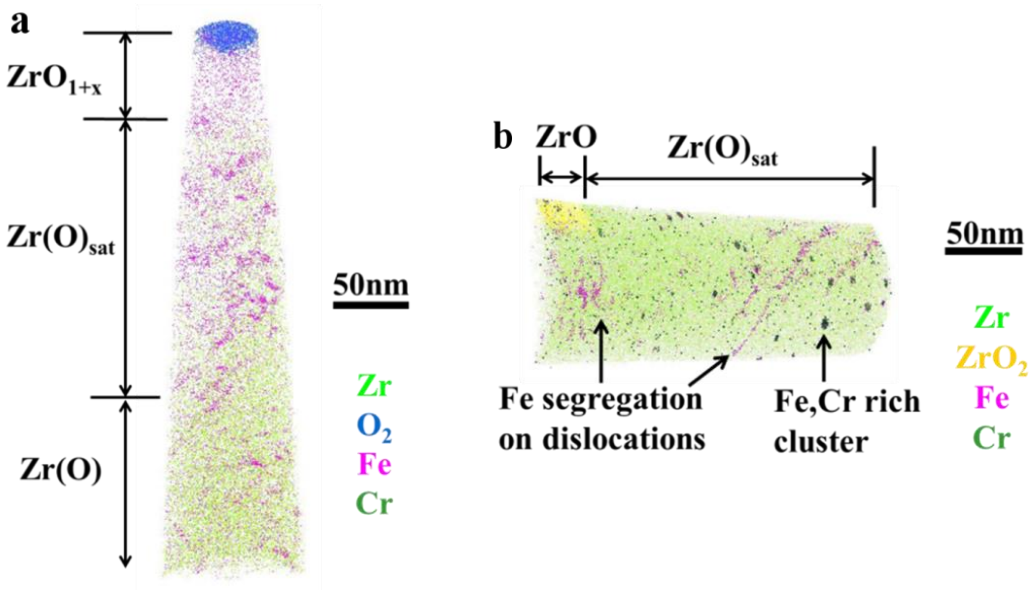

Figure 7.3: Zircaloy-4 near oxide region: (a)-(b) 3D atomic maps of two representative APT reconstructions that illustrate the Fe segregation at dislocations in $Zr(O)_{sat}$ and solid solution and Fe, Cr rich clusters in $Zr(O)_{sat}$.

Segregation of Sn was observed between ZrO and the saturated solid solution $Zr(O)_{sat}$. The segregation to the $Zr(O)_{sat}$/ZrO interface was strongly dependent on the local curvature of the interface. As illustrated in Figure 7.4, higher levels of Sn were observed in the region between the ZrO fingers, indicating a rejection of Sn from the suboxide.

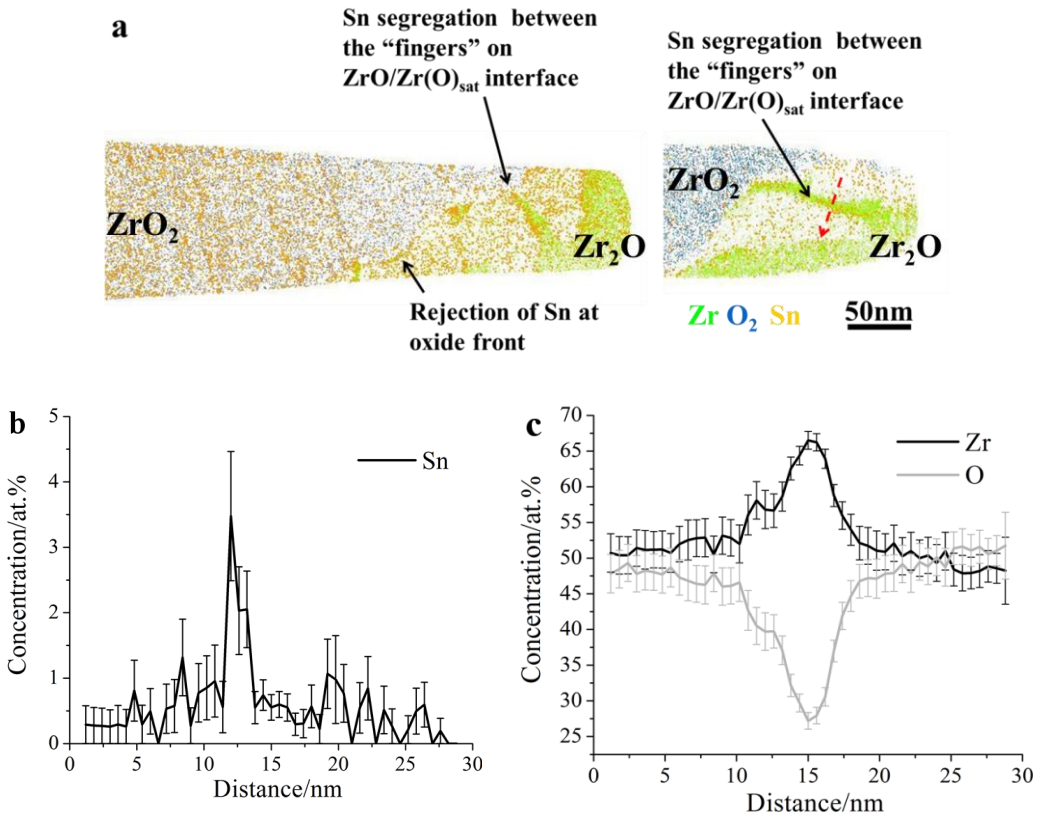

Figure 7.4: Zircaloy-4 near oxide region: (a) 10 nm slices taken from two distinct APT reconstructions showing distribution of Sn; (b) and (c) concentration profiles measured by placing a 10 nm cylinder along the red arrow indicated in (a).

Fe and Sn were also observed to segregate to grain boundaries beneath the ZrO suboxide layer. A slice of the dataset containing grain boundaries is shown in Figure 7.5(a), along with a concentration profile (Figure 7.5(b)). The local concentration of Fe (segregation factor) was quite high compared to the overall Fe content within the alloy (0.2 at. %). The enrichment of Fe and Sn was around similar level to the segregation level on grain boundaries far away from oxide scale, indicating the presence of oxygen did not significantly affect grain boundary chemistry. No increased oxygen level was observed at the grain boundary.

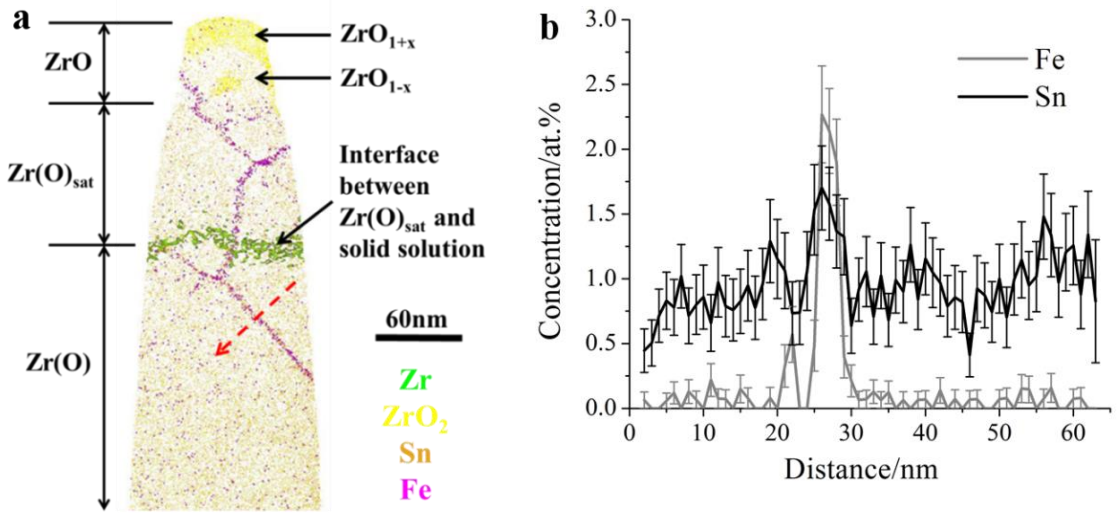

Figure 7.5: Zircaloy-4 near oxide region: (a) 10 nm slice from an APT reconstruction showing the segregation of Fe and Sn at the grain boundaries in the $Zr(O)_{sat}$ and solid solution; (b) concentration profile measured by placing a 10 nm cylinder across the grain boundary along the red dashed arrow indicated in (a).

7.2.3 Zr-Fe-Cr

The Fe distribution near oxide front in the Zr-Fe-Cr alloy was comparable with that in pure Zr and Zircaloy-4. Fe-decorated dislocations were observed in all of the APT datasets examined. Some datasets, as illustrated in Figure 7.6, even exhibited signs of dislocations piling up to form a low angle sub grain boundaries. The overall Fe concentration within the suboxides and solid solution regions of the Zr-Fe-Cr alloy was more than twice of the Fe level in the same region of pure Zr.

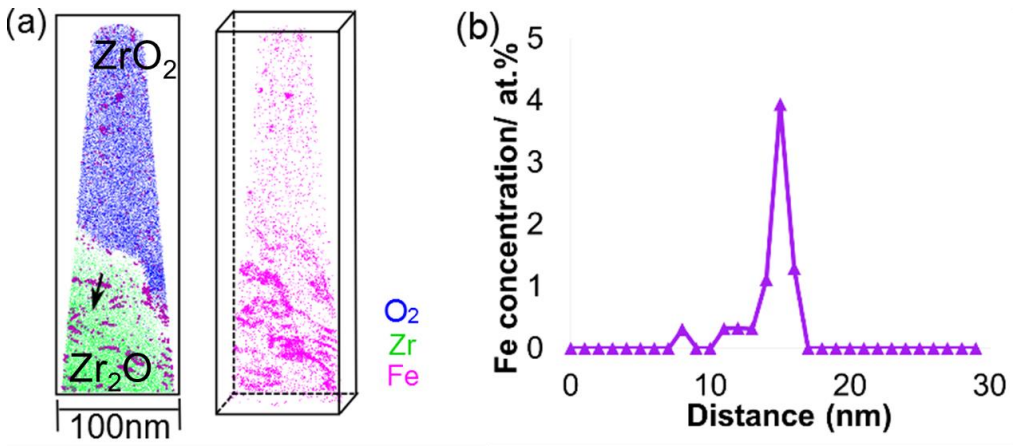

Figure 7.6: Zr-Fe-Cr near oxide region: (a) 10 nm slice (left) and 3D Fe map (right) of a representative APT dataset illustrating the Fe distribution; (c) Fe concentration profile measured by placing a 10 nm cylinder across the dislocation along the arrow indicated in (a).

Grain boundaries with Fe segregation were also observed in $Zr(O)_{sat}$ phase and solid solution (Figure 7.7). The Fe segregation to one of the boundaries was still seen segregated into the ZrO phase (Figure 7.7(a)). No increased oxygen level was observed at grain boundary.

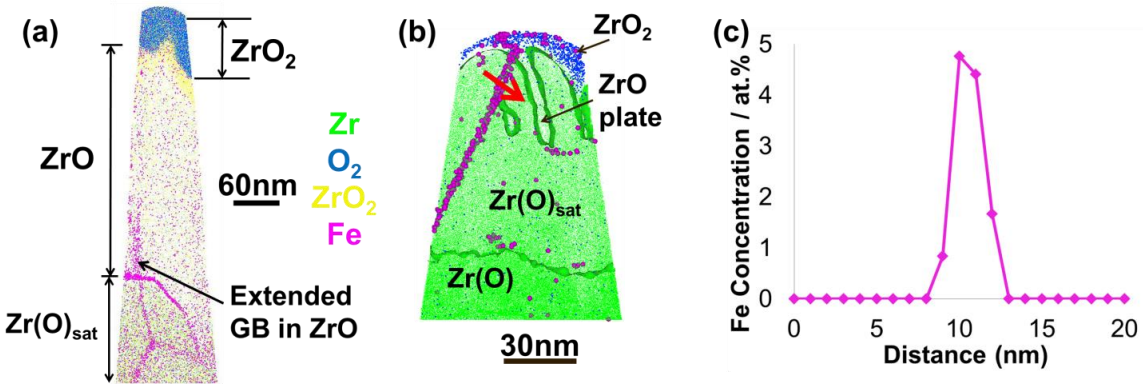

Figure 7.7: Zr-Fe-Cr near oxide region: (a)-(b) 10 nm slices of two representative APT datasets illustrating the Fe segregation on grain boundaries; (c) Fe concentration profile measured by placing a 10 nm cylinder across the grain boundary along the red arrow in (b).

7.3 Solute Distribution within ZrO_2 Oxide

7.3.1 Pure Zr

Fe clusters were occasionally detected on planar and linear features within ZrO_2 in pure Zr. The Fe concentration in ZrO_2 phase of pure Zr and Zr-Fe-Cr is summarized in Table 7.1. The standard deviation of measured Fe concentration in the oxide of pure Zr was large due to the large variation among datasets that were taken from different regions in pure Zr. As seen in Figure 7.8, the Fe concentration measured from the APT reconstruction shown in Figure 7.8(a) had a peak value of 0.59 at.%; whereas the Fe concentration in the clusters in Figure 7.8(b) reached almost 20 at.%. Note that the measured concentration was affected by ion trajectory aberrations from the difference in evaporation fields between matrix and clusters so the concentration profile in Figure 7.8(c) could only provide a qualitative demonstration of the huge variations between the two datasets.

In all of the APT datasets we examined, higher Fe concentration was associated with the presence of a metal grain boundary underneath the ZrO_2 phase. As seen in Table 7.1, the measured Fe concentration in the ZrO_2 phase was about ten times higher if the measurement was conducted in vicinity of a metal grain boundary. However, we need to note here that the correlation between high Fe concentration and the presence of a grain boundary in pure Zr might be only coincidence due to limited sampling.

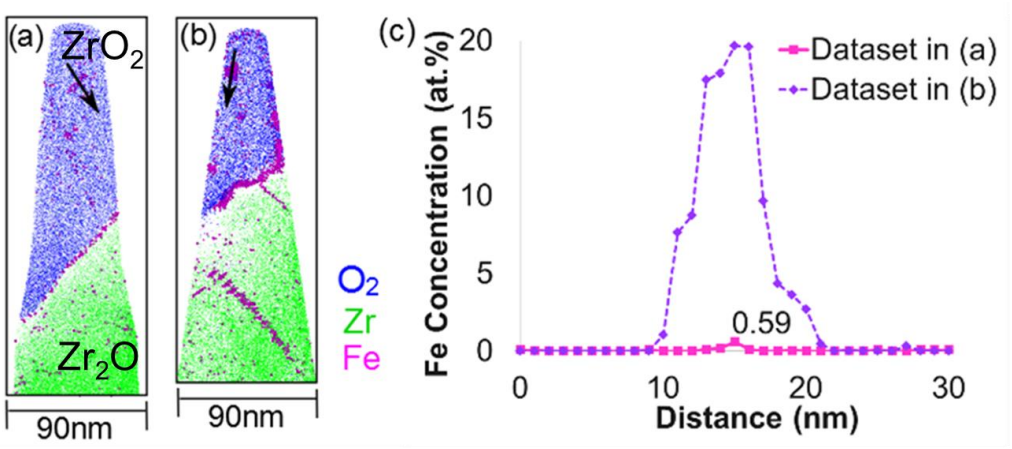

Figure 7.8: Pure Zr oxide: (a) and (b) are 10 nm slices from two representative APT datasets showing the Fe distribution in the ZrO_2 layer; (c) Fe concentration profile measured by placing 10 nm cylinders across the Fe clusters as indicated by the black arrows in (a) and (b).

7.3.2 Zircaloy-4

Sn exhibited inhomogeneous distribution within the ZrO_2 oxide layer in Zircaloy-4. In pre-transition Zircaloy-4, segregation/clustering of Sn was not significant and only slight signs of clustering can be observed in Figure 7.9(a). A large portion of Sn was still in the matrix of ZrO_2. In the dataset that taken from transition stage, clustering of Sn appeared to be more visible, which was associated with a decreased Sn concentration in the ZrO_2 matrix. However, the trend observed here might only be a coincidence due to limited sampling. The planar type features to which Sn segregated had a spacing similar to the measured columnar oxide grain width in these samples, about 30-50 nm, indicating a possible segregation of Sn to oxide grain boundaries.

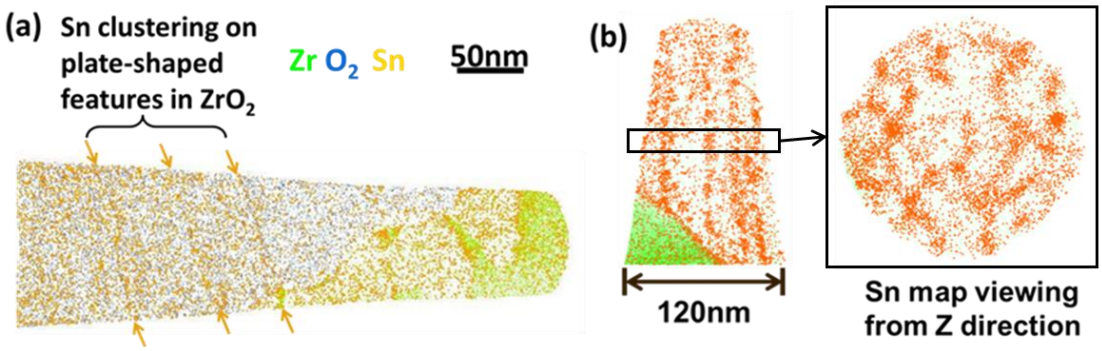

Figure 7.9: Zircaloy-4 oxide: 10 nm slices of two distinct APT reconstructions showing distribution of Sn. The two reconstructions were taken from alloy samples that were archived at (a) pre-transition and (b) almost at the transition regime.

7.3.3 Zr-Fe-Cr

The Fe distribution within the ZrO_2 phase in the Zr-Fe-Cr alloy was qualitatively similar to pure Zr but exhibited less pronounced variations among datasets taken with or without a metal grain boundary present. As seen in Figure 7.10, the Fe concentrations measured from the two representative APT reconstructions were comparable regardless of whether or not metal grain boundary is present underneath the oxide. The overall Fe concentration in the ZrO_2 phase in the Zr-Fe-Cr alloy, as listed in Table 7.1, was about twice of the measured Fe concentration in ZrO_2 oxide formed on pure Zr.

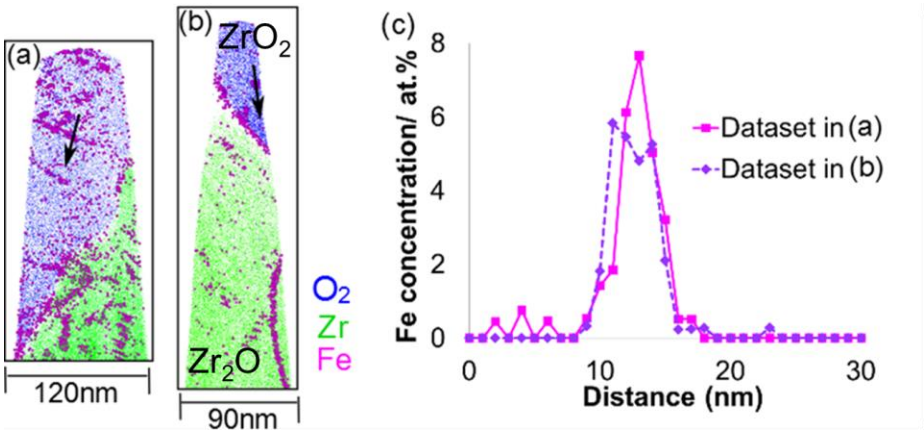

Figure 7.10: Zr-Fe-Cr oxide: (a) and (b) are 10 nm slices taken from two representative APT datasets selected to show the Fe distribution in the ZrO_2 layer; (c) Fe concentration profile measured by placing 10 nm cylinders across the Fe clusters as indicated by the black arrows in (a) and (b).

7.4 Grain Boundary Chemistry

7.4.1 Quantification of Grain Boundary Segregation

It was hypothesized that differences in grain boundary chemistry could explain the different stability of oxide layers formed on pure Zr and the Zr-Fe-Cr alloy. However, we observed comparable amounts of Fe segregations at grain boundaries in pure Zr and the Zr-Fe-Cr alloy, which excluded the possibility that grain boundary chemistry alone determined the oxide growth stability. To ensure the statistical reliability, interfacial excesses for grain boundaries in all collected datasets were calculated to compare Fe segregation in pure Zr and the Zr-Fe-Cr alloy.

The interfacial excess Γ_s was calculated following the equation [193]:

$$\Gamma_s = \frac{\sum_{n=1}^{N}(C_n - C_0)}{A(1-C_0)} \qquad \text{Equation 7.1}$$

where the sum is over all of grain boundary atoms under consideration, C_n is the concentration of the nth atom (i.e. 1 if the nth atom is solute s, and 0 otherwise), C_0 is the concentration of solute s in the matrix and A is area of the grain boundary. The interface excess values varied from dataset to dataset but showed no significant difference between pure Zr and the Zr-Fe-Cr alloy as shown in Table 7.2.

Table 7.2: Average of measured interfacial excesses (atom/nm^2). The uncertainty is the standard deviation over the number of analyses indicated in ().

	Pure Zr	Zr-Fe-Cr Alloy
Zr(O)	3.9 ± 1.9 (5)	2.7 (1)
$Zr(O)_{sat}$	5.7 ± 1.1 (2)	5.7 ± 0.7 (2)

7.4.2 Oxygen Ingress along Grain Boundaries

Fe distribution along grain boundaries in the oxide phases were different from dataset to dataset, resulting in different oxygen ingress along the grain boundaries in the metal. Three different cases are illustrated in Figure 7.11. In the first case found in pure Zr, the oxygen concentration increased at the grain boundary, from ~20 at. % to ~50 at. %, leading to the formation of the ZrO phase. The Fe segregation along the grain boundary extended from the

metal into the oxide (Figure 7.11(h)). From the SEM image (Figure 7.11(d)), a vertical crack formed on the top of the oxide layer, pointing at a direction parallel with the grain boundary. It was also accompanied by a steep oxide advance along the grain boundary. In the second case also found in pure Zr, the Fe segregation visible along the metal grain boundary was interrupted at the oxide/metal interface. This can be interpreted as either the grain boundary did not extend into the oxide phase or that the boundary did extend but was not decorated by Fe. A crack and faster oxide growth along the grain boundary were also observed, but the crack propagation direction was not along the grain boundary plane and there was no steep oxide advance along the grain boundary (Figure 7.11(e), (h)). In the third case found in the Zr-Fe-Cr alloy (Figure 7.11(c)), Fe segregation was at same level compared to the two datasets discussed previously. However, neither faster oxide advance along the grain boundary (Figure 7.11(h)) nor cracking in the oxide was evident (Figure 7.11(f)).

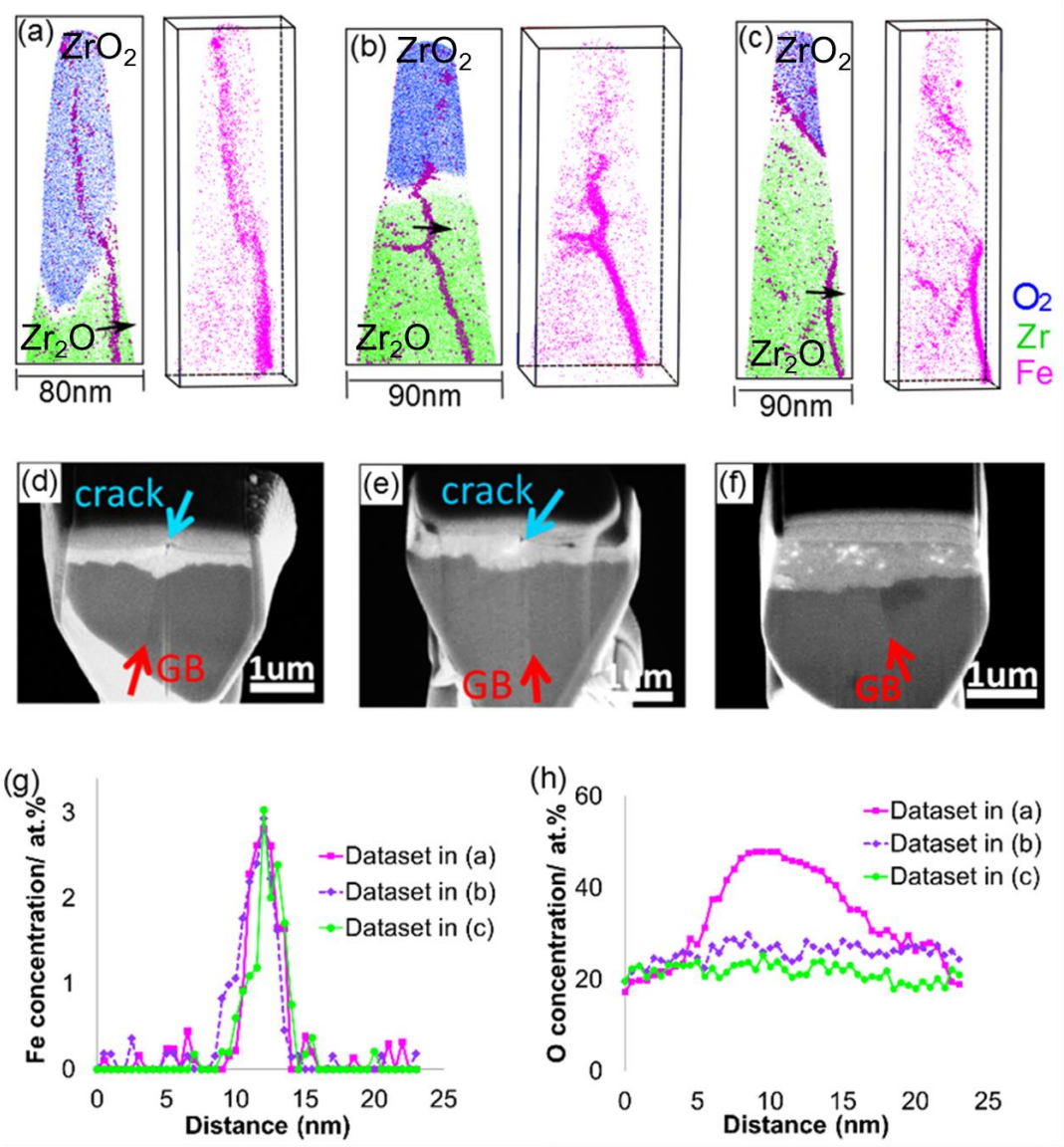

Figure 7.11: (a)-(c) 10 nm slices (left) and 3D Fe maps (right) taken from three representative APT reconstructions from (a,b) pure Zr and (c) the Zr-Fe-Cr alloy; (d)-(f) The SEM images of non-sharpened APT needles that correspond to the reconstructions in (a)-(c); (g)-(h): concentration profiles measured by placing 10 nm cylinders across the grain boundaries along the arrows indicated in the respective dataset.

7.5 Discussion

7.5.1 Cr Distribution

The solubility of Cr in Zr is very low leading to the formation of second phase particles (C14 $Zr(Fe,Cr)_2$) [19, 188]. In the present study, there was no indication of Cr segregation neither to grain boundaries nor to dislocations in any of the three alloys. The absence of Cr enrichment on the grain boundaries disagreed with the simulation by Christensen et al. [194]. The lack of Cr enrichment was initially speculated to be due to the fact that Cr mobility is lower than that of Fe [195, 196]. However, using the activation energy and D_0 values from Ref. [197], the diffusion coefficients of Cr and Fe in Zr at 360 °C were calculated to be 1.17×10^{-8} cm^2/s and 0.024 cm^2/s. The diffusion distance ($\sim2\sqrt{Dt}$) for Cr and Fe after 500 days was then ~ 0.9 cm and ~ 415 cm. Even for the less mobile Cr, the time would be long enough for redistribution to occur. Therefore it was more likely that Cr was more thermodynamically stable in the form of second phase particle. Cr was occasionally observed in small clusters in the bulk metal and near the oxide interface in Zircaloy-4 and the Zr-Fe-Cr alloy. The presence of such clusters (around 3.5 nm in size) was also reported by Hudson [162]. No such clusters were observed in pure Zr, likely due to the extremely low Cr level. However, their presence cannot be excluded due to the limited sampling of APT. Yet no conclusion can be made on how Cr may affect the corrosion kinetics of Zr alloys.

7.5.2 Sn Distribution

Sn is a major alloying addition in Zircaloy-4 usually added to improve mechanical properties and creep resistance. Previous work on Zr-Sn-Nb alloys [162] suggested that Sn was incorporated into the oxide leading to a constant Sn/Zr ratio in both the oxide and the metal. The present study however found that, the Sn/Zr ratio in ZrO_2 was lower than that in the suboxides and the metal. This could be caused by rejection of Sn ahead of the oxide front. The rejection of Sn by the growth of ZrO_2 was demonstrated by the evidence of Sn being pinned on grain boundaries in ZrO_2 as well as segregation of Sn to ZrO_2/ZrO interface and ZrO/$Zr(O)_{sat}$ interface. The segregation of Sn into what appeared to be oxide grain boundaries could lend support to previously proposed ideas of changing oxide conductivity as a result of elemental segregation to oxide grain boundaries creating preferential paths for electron conduction [155]. Sn clustering and segregation in the bulk oxide was also reported in a more recent APT study [158], where Sn clusters were shown to continue growing to form larger metallic particles as the oxidation proceeds.

7.5.3 Fe Distribution

Similarly to Cr, Fe has very limited solubility in α-Zr leading to precipitation of second phase particles or segregation to dislocations and grain boundaries. Segregation of Fe to grain

boundaries was common to all three alloys both in the bulk region and in the $Zr(O)_{sat}$ and solid solution near the oxide scales. Segregation of Fe on grain boundaries was previously found in APT analyses of other Zr alloys [162]. Quantitative analysis shows that Fe segregation levels were comparable for both pure Zr and the Zr-Fe-Cr alloy while the oxygen ingress along grain boundaries was drastically different. Therefore it is reasonable to conclude that Fe segregation to the metal grain boundaries alone cannot explain the difference in the oxide stability between pure Zr and the Zr-Fe-Cr alloy. However, cracks and faster oxide advance along grain boundary seemed to correlate with a continuous Fe segregation that extended from metal to oxide, which indicated that differences in the structure and chemistry of the oxide scales were more likely to contribute to faster oxidation along metal grain boundaries and oxide growth instabilities than the underlying metal microstructure.

Within the solid solution region, Fe segregated to linear features, probably dislocations, as also found by Hudson [162]. Fe decorating dislocations was observed only in the $Zr(O)_{sat}$ layer and in the solid solution near the oxide/metal interface while it was absent in the metal away from oxide/metal interface. The presence of dislocations can be rationalized in terms of local strains induced by the growing oxide. The total amount of Fe segregated on dislocations in pure Zr was less than half of that in the Zr-Fe-Cr alloy. We therefore hypothesize that the Fe distribution at the oxide front may play a role in the phase and orientation selection of the new oxide grains nucleating at the ZrO_2/Zr(O) or ZrO_2 /$Zr(O)_{sat}$ interface. For example, in the

Zr-Fe-Cr alloy, the oxide grains may nucleate as tetragonal phase as higher amount of Fe was stabilizing the tetragonal phase. In pure Zr, there was not enough Fe at the oxide front and therefore tetragonal phase were less likely to form, leading to a different oxide texture evolution. Also, the dataset to dataset variation of Fe content in the solid solution of pure Zr may contribute to the differential grain to grain growth of oxide.

Fe incorporated into ZrO_2 formed clusters on the oxide grain boundaries. Previous studies by Mössbauer spectra demonstrated that Fe in ZrO_2 mainly exist as Fe^{2+} or in intermetallic compound [157-158]. The Fe clusters could serve as faster electron conduction path and therefore contributed to the higher oxidation rate in the Zr-Fe-Cr alloy before breakaway. The correlation between faster oxide ingress along grain boundary with continuous Fe segregation also supports that Fe within the oxide can enhance the oxidation.

7.6 Summary

The solute distributions near the oxide scale were examined in this chapter. The distribution of alloying elements was modified in the oxygen-rich region of the metal next to the oxide front. Segregation and clustering of Fe and Sn were observed at both ZrO_2/ZrO and ZrO/$Zr(O)_{sat}$ interfaces. Fe segregation to linear features (possibly dislocations) was present in the $Zr(O)_{sat}$ layer and in the solid solution near the oxide/metal interface. Fe-decorated

dislocations distributed more uniformly in the more stable Zr-Fe-Cr alloy. Comparable amount of Fe segregation was observed at the metal grain boundaries in pure Zr and the Zr-Fe-Cr alloy.

Within the oxide layer, clustering and segregation of Fe and Sn were observed on the oxide grain boundaries. In the oxide of pure Zr, higher Fe content was found when measurements were taken in the oxide that lied on top of metal grain boundaries; whereas the Fe clusters distributed more evenly in the oxide of the Zr-Fe-Cr alloy.

CHAPTER 8

Conclusion and Future Directions

8.1 Main Observations

In this thesis work, a multi-scale characterization approach was used to study the oxidation behavior of zirconium alloys and determine the microstructural contributions of the wide range of behaviors. A detailed analysis was conducted on the microstructures and chemistry of oxide and suboxide phases, metal/oxide interface, and solid solutions near the oxide front in alloy samples that had different compositions and different corrosion times. The observations regarding the microstructures and chemistry in pure Zr and the Zr-Fe-Cr alloy are illustrated in Figure 8.1. The findings are summarized as follows:

1. For all alloys, the same sequence of sub-oxide phases was observed ahead of the ZrO_2 oxide front, and it consisted of (i) a thin layer of equiatomic ZrO (occasionally slightly over and under stoichiometric but variation might come from evaporation artifact) (ii) saturated solid solution $Zr(O)_{sat}$ with a constant oxygen concentration

consistent with the Zr_2O stoichiometry, and (iii) a slowly decreasing oxygen profile into the metal.

2. The width of the intermediate oxide layers depended both on the alloy chemistry and on the stage of corrosion. The thicknesses of the suboxide phases seemed to inversely correlate to the oxidation rate.

3. Fast oxide growth and formation of oxide dendrites along the grain boundary were observed only in pure Zr even though the measured grain boundary chemistry showed no difference compared to that in the Zr-Fe-Cr alloy.

4. A fiber texture was observed in the oxide scale of the Zr-Fe-Cr alloy that also exhibited a stable oxide growth. In pure Zr, a greater degree of preferential orientation of oxide grains, with the (200) plane of the oxide grains lying close to the $(10\bar{1}1)$ plane of substrate metal, led to an oxide texture that deviated from the fiber texture.

5. The Sn/Zr ratio in ZrO_2 was lower than that in the suboxides and the metal. The rejection of Sn by the growth of ZrO_2 was demonstrated by the evidence of Sn segregation at grain boundaries in ZrO_2 and segregation of Sn to the ZrO_2/ZrO and the ZrO/$Zr(O)_{sat}$ interfaces.

6. Fe segregated to dislocations present in $Zr(O)_{sat}$ and in the solid solution region near the oxide front. In the Zr-Fe-Cr alloy, Fe-decorated dislocations were more uniformly

distributed compare to pure Zr, resulting in a higher overall Fe content in the region next to oxide front.

7. Fe clustering was observed on the ZrO_2 oxide grain boundaries. The Fe distribution within ZrO_2 oxide was more homogeneous in the Zr-Fe-Cr alloy; whereas in pure Zr, much higher Fe concentrations were detected in the vicinity of metal grain boundaries.

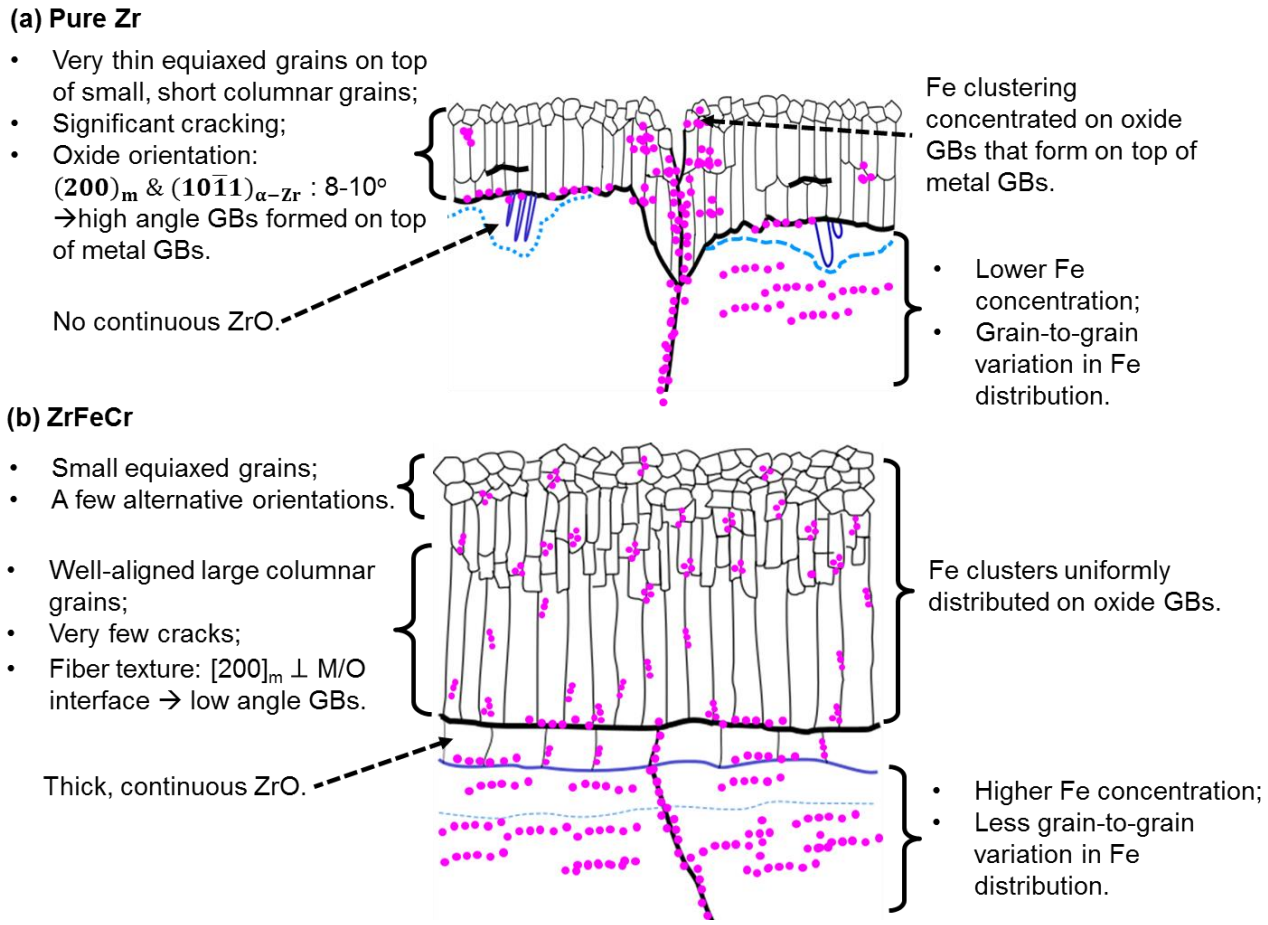

Figure 8.1: Schematic illustration of oxide structure and Fe distributions near oxide scale in (a) pure Zr and (b) Zr-Fe-Cr alloy. The pink dots represent the Fe atoms.

8.2 Microstructural Contributions

As described in previous chapters, complex oxide phase structures, morphologies, and grain textures were observed in the oxide scales formed on pure Zr and the Zr-Fe-Cr alloy, along with enhanced inhomogeneity of solute distributions compared to bulk metal. By comparing the microstructures and chemistry, we identified factors that could potentially impact the protective character of the oxide phases, and will now assess how these could potentially affect the stability of oxide growth.

Oxide texture

Pure Zr and the Zr-Fe-Cr alloy developed different oxide grain textures. The oxide grains in pure Zr nucleated in a specific orientation depending on the orientation of underlying metal. The orientation relationship seemed to be largely maintained as the oxide grew thicker. The greater degree of preferential orientation in the oxide layer, or in other word, less pronounced fiber texture, could contribute to higher stress built-up within the oxide (as evident by more cracking). In addition, as a result of the preferential orientation, the oxide grain boundaries formed above a metal grain were low angle grain boundaries while the oxide grain boundaries on top of a metal grain boundary were high angle grain boundaries. The formation of high angle oxide grain boundaries could cause the metal grain boundaries to be more susceptible to oxygen ingress and eventually lead to oxide dendrite formation.

In the Zr-Fe-Cr alloy, a few alternative orientations were spotted within the surface region where oxide grains were equiaxed. The oxide grains that formed 300 to 500 nm beneath the surface quickly developed a fiber texture, where the [200] direction of monoclinic ZrO_2 lied close to the oxide growth direction. Since the oxide grains were oriented in such way that oxide growth strain was minimized [165], less stress built-up and well-aligned large columnar grains were anticipated. Another benefit of forming the fiber texture may be that the oxide grain boundaries that formed above metal grain boundaries were low angle grain boundaries. Such boundaries were generally considered more cohesive and therefore more protective against the oxygen ingress [166].

Fe distribution

Fe enrichment was observed in the oxide and also in the oxygen rich region next to the oxide front. Quantitative measurements showed that the overall Fe content at the oxide front was higher in the Zr-Fe-Cr alloy where the fiber texture formed and the oxide growth was stable. It is therefore reasonable to hypothesize that the Fe enrichment at the oxide front played a role on the orientation selection of the new grains nucleating at the Zr or suboxide / ZrO_2 interface and therefore contributed to the formation of more beneficial fiber texture. On the other hand, Fe was found as clusters on oxide grain boundaries. Based on the datasets, Fe clustering seemed to be more homogenous within the oxide layer of the Zr-Fe-Cr alloy; whereas in the oxide of pure Zr, Fe enrichment was more concentrated in the region on top of metal grain

boundaries. Since Fe was incorporated into oxide layer at a lower valence (even as metallic) compare to Zr^{4+}, it generated extra oxygen vacancies and enhances electron transport and oxygen diffusion [192]. The observed Fe distribution was therefore consistent with preferential oxide growth along the grain boundary in pure Zr.

Suboxides

From the comparison of pure Zr and the Zr-Fe-Cr alloy, we observed that the scale of suboxides inversely correlated to oxidation rate. The question was how the observed intermediate phases could affect the corrosion behavior. The fact that some oxygen was used to form the layers, rather than forming stoichiometric ZrO_2 would cause a slight slowing down of oxide formation. However, this effect was considered small, since the total oxygen content in these layers was small compared to the overall oxygen content in the stoichiometric oxide. On the other hand, since the oxygen could harden the metal region next to the oxide front, the plasticity of the Zr matrix may be hampered, which might accelerate stress accumulation at oxide/metal interface. The suboxide layers were likely to be consequences rather than causes of the pre-transition corrosion behavior, but we cannot rule out the possibility that oxygen rich layers could also affect the orientation of newly formed ZrO_2 grains through changing the stress and chemistry at the oxide front.

Metal grain boundaries

Quantitative analysis showed that Fe segregation levels on the metal grain boundaries were comparable for both pure Zr and the Zr-Fe-Cr alloy. Fe segregation to the metal grain boundaries alone could not explain the difference in the oxide stability. Instead, the synergy between oxide texture and oxide chemistry was more likely to promote fast oxide growth along grain boundaries in pure Zr. Indeed, the spatial correlation between high angle oxide grain boundaries and metal grain boundaries might be the cause for oxygen ingress and a cause for oxide instability. It is worth noting here that the volume sampled by APT was extremely small. Though we tried our best to obtain APT specimens from different regions along the oxide/metal interface, there is still a chance that the data presented were not fully representative of the overall behavior.

8.3 Recommendations for Future Work

In this study, we hypothesized that Fe enrichment at the oxide front could affect the orientations of new oxide grains nucleating at the interface. Although the experimental observations supported this hypothesis, it remains unclear how Fe affected the crystallographic orientations of oxide grains. As discussed in section 7.5.3, one possibility is that Fe stabilizes the tetragonal ZrO_2 phase so oxide grains nucleated as the highly oriented

tetragonal phase and then transformed to well-aligned monoclinic ZrO_2. However, existing experimental techniques do not have the capability to provide a systematic mapping of tetragonal phase at high spatial resolution. To support the speculation made in this work, it is recommended to obtain a more fundamental understanding, possibly through theoretical simulation, on how stress and alloying elements can stabilize the tetragonal phase. The theoretical model should assess the likelihood of forming tetragonal ZrO_2 instead of monoclinic ZrO_2 on top of $Zr(O)_{sat}$ and whether stress or/and solutes can make the process more energetically favorable.

We investigated the evolution of suboxides (ZrO and $Zr(O)_{sat}$) at different stages of oxidation. We speculated that the thickening of the suboxides was a consequence rather than cause of the slower oxide growth based on the rationale that dissolved oxygen ahead of the oxide layer was to harden the matrix and make more difficult the creep accommodation of the lateral oxide growth strains during corrosion. To confirm the hypothesis, it would be interesting to explore the possible roles of the suboxide on the stress state of ZrO_2 through simulation since measuring the experimental techniques that can accurately measure stress distribution within the oxide layer is not readily available.

Lastly, this thesis work only covered the discussion of how solute Fe distributions correlated with different oxide microstructures and oxide growth behaviors. It would be worth studying the roles of other solutes such as Cr, Sn, and Nb that are used in commercial Zr-based alloys.

It would be more beneficial to first study simpler binary (Zr-Fe, Zr-Cr, Zr-Sn, Zr-Nb, etc.) and ternary alloys (Zr-Fe-Nb, Zr-Sn-Fe, Zr-Sn-Nb, etc.) that contain elements of interest to separately assess the effects of individual alloying elements. Also, since cladding materials will be exposed to irradiation in the reactor environment, it is important to investigate the response of alloying element distribution to the irradiation and how that change could further impact the corrosion process.

References

[1] Y. Dong, A. T. Motta, and E. A. Marquis, "Atom probe tomography study of alloying element distributions in Zr alloys and their oxides," *Journal of Nuclear Materials,* vol. 442, pp. 270-281, 2013.

[2] B. de Gabory, Y. Dong, A. T. Motta, and E. A. Marquis, "EELS and atom probe tomography study of the evolution of the metal/oxide interface during zirconium alloy oxidation," *Journal of Nuclear Materials,* vol. 462, pp. 304-309, 2015.

[3] C. Lemaignan and A. T. Motta, "Zirconium Alloys in Nuclear Applications," *presented at the Materials Science and Technology, A Comprehensive Treatment*, New York, 1994.

[4] E. Hillner, "Corrosion of Zirconium-base alloys: an Overview," presented at the Zirconium in the Nuclear Industry: 3rd International Symposium, 1977.

[5] T. Ahmed and L. H. Keys, "'The Breakaway Oxidation of Zirconium and Its Alloys: A Review," *Journal of the Less-Common Metals,* vol. 39, pp. 99-107, 1975.

[6] A. T. Motta, "Waterside Corrosion in Zirconium Alloys," *Journal of Metals,* vol. 63, pp. 59-63, 2011.

[7] S. Kass, "Aqueous corrosion of the zircaloys at low temperatures," *Journal of Nuclear Materials,* vol. 29, pp. 315-321, 1969.

[8] S. Kass, "The Development of the Zircaloys," *presented at the Symposium on Corrosion of Zirconium Alloys*, Philadelphia, USA, 1964.

[9] G. P. Sabol, "ZIRLO an Alloy Development Success," in *14th ASTM INternational Symposium on Zr in the Nuclear Industry*, Stockholm, pp. 3-24, 2005.

[10] G. L. Garner and J. P. Mardon, "Performance of Alloy M5 in a High Duty U.S. Reactor," *Nuclear Engineering International,* pp. 36, 2002.

[11] D. L. Douglass, *The Metallurgy of Zirconium*. Vienna: International Atomic Energy Agency Supplement, 1971.

[12] I. A. E. Agency, "Waterside Corrosion of Zirconium Alloys in Nuclear Power Plants," International Atomic Energy Agency, Vienna TECDOC996, 1998.

[13] B. Cox, "Some thoughts on the mechanisms of in-reactor corrosion of zirconium alloys," *Journal of Nuclear Materials,* vol. 336, pp. 331-368, 2005.

[14] J. P. Abriata, J. Garces, and R. Versaci, "The O-Zr (Oxygen-Zirconium) System," *Bulletin of Alloy Phase Diagrams,* vol. 7, pp. 116-124, 1986.

[15] J. P. Abriata, J. C. Bocich, and D. Arias, "The Sn−Zn (Tin-Zirconium) system," *Bulletin of Alloy Phase Diagrams,* vol. 4, pp. 147-154, 1983.

[16] D. Arias and J. P. Abriata, "The Cr-Zr (Chromium-Zirconium) System," *Bulletin of Alloy Phase Diagrams,* vol. 7, pp. 237-244, 1986.

[17] D. Arias and J. P. Abriata, "The Fe−Zr (Iron-Zirconium) system," *Bulletin of Alloy Phase Diagrams,* vol. 9, pp. 597-604, 1988.

[18] P. Nash and C. S. Jayanth, "The Ni−Zr (Nickel-Zirconium) system," *Bulletin of Alloy Phase Diagrams,* vol. 5, pp. 144-148, 1984.

[19] D. Charquet, R. Hahn, E. Ortlieb, J.-P. Gros, and J.-F. Wadier, "Solubility Limits and Formation of Intermetallic Precilitates in ZrSnFeCr Alloys," in *Zirconium in the Nuclear Industry: 8th International Symposium*, pp. 405-422, 1989.

[20] J. P. Abriata and J. C. Bolcich, "The Nb-Zr (Niobium-Zirconium) System," *Bulletin of Alloy Phase Diagrams,* vol. 3, pp. 34-44, 1982.

[21] P. Bossis, D. Pecheur, K. Hanifi, J. Thomazet, and M. Blat, "Comparison of the High Burnup Corrosion on M5 and Low Sn Zircaloy-4," *Journal of ASTM International,* vol. 3, JAI12404, 2006.

[22] R. A. Holt, "The beta to alpha phase transformation in zircaloy-4," *Journal of Nuclear Materials,* vol. 35, pp. 322-334, 1970.

[23] G. Ökvist and K. Källström, "The effect of zirconium carbide on the β → α transformation structur in zircaloy," *Journal of Nuclear Materials,* vol. 35, pp. 316-321, 1970.

[24] D. Charquet and E. Alheritiere, "Influence of Impurities and Temperature on the Microstructure of Zircaloy-2 and Zircaloy-4 after the Beta- Alpha Phase Transformation," *Zirconium in the Nuclear Industry: 7th International Symposium*, Philadelphia, USA, 1987.

[25] L. J. Chai, B. F. Luan, S. S. Gao, J. W. Chen, and Q. Liu, "Study of precipitate evolution and recrystallization of β-quenched Zr–Sn–Nb–Fe–Cr–Cu alloy during aging," *Journal of Nuclear Materials,* vol. 427, pp. 274-281, 2012.

[26] K. Loucif, R. Borrelly, and P. Merle, "Microstructural Evolution of β-quenched Zircaloy-4 During Aging between 100 and 750°C," *Journal of Nuclear Materials,* vol. 210, pp. 84-96, 1994.

[27] C. D. Williams and R. W. Gilbert, "Tempered structures of a Zr-2.5 wt % Nb alloy," *Journal of Nuclear Materials,* vol. 18, pp. 161-166, 966.

[28] D. O. Northwood, X. Y. Meng, and B. D. Warr, "Microstructure of Zr-2.5Nb Alloy Pressure Tubing," in *9th International Symposium on Zr in the Nuclear Industry*, pp. 156-176, 1991.

[29] S. A. Aldridge and B. A. Cheadle, "Age hardening of Zr-2.5 wt % Nb slowly cooled from the (α +β) phase field," *Journal of Nuclear Materials,* vol. 42, pp. 32-42, 1972.

[30] E. Steinberg, H. G. Weidinger, and A. Schaa, "Analytical Approaches and Experimental Verification to Describe the Influence of Cold work and Heat Treatment on the Mechanical Properties of Zircaloy Cladding Tubes," *Zirconium in the Nuclear Industry: 6th International Symposium*, Philadelphia, 1982.

[31] J.-C. Tedenac and P. Perrot, "Iron-Niobium-Zirconium in Iron Systems: Phase Diagrams, Crystallographic and Thermodynamic Data", *Landolt-Börnstein - Group IV Physical Chemistry*, vol. 11D5, pp. 101-116, 2009.

[32] P. Barberis, D. Charquet, and V. Rebeyrolle, "Ternary Zr-Nb-Fe(O) System: Phase Diagram at 853 K and Corrosion Behaviour in the Domain Nb<0.8%," *Journal of Nuclear Materials*, vol. 326, pp. 163-174, 2004.

[33] P. Chemelle, D. B. Knorr, J. B. V. D. Sande, and R. M. Pelloux, "Morphology and Composition of Second Phase Particles in Zircaloy-2," *Journal of Nuclear Materials*, vol. 113, pp. 28-64, 1983.

[34] V. Kraševec, "Transmission Electron Microscopy Study of Second Phase Particles in Zircaloy-2," *Journal of Nuclear Materials*, vol. 98, pp. 235-237, 1981.

[35] E. Vitikainen and P. Nenonen, "Transmission Electron Microscopy Studies on Intermetallics in Some Zirconium Alloys," *Journal of Nuclear Materials*, vol. 78, pp. 362-373, 1978.

[36] X. Y. Meng and D. O. Northwood, "Intermetallic Precipitates in Zircaloy-4," *Journal of Nuclear Materials*, vol. 132, pp. 80-87, 1985.

[37] H. G. Kim, S. Y. Park, M. H. Lee, Y. H. Jeong, and S. D. Kim, "Corrosion and microstructural characteristics of Zr–Nb alloys with different Nb contents," *Journal of Nuclear Materials*, vol. 373, pp. 429-432, 2008.

[38] W. Liu, Q. Li, B. Zhou, Q. Yan, and M. Yao, "Effect of heat treatment on the microstructure and corrosion resistance of a Zr–Sn–Nb–Fe–Cr alloy," *Journal of Nuclear Materials*, vol. 341, pp. 97-102, 2005.

[39] Y. Z. Liu, W. J. Zhao, Q. Peng, H. M. Jiang, and X. T. Zu, "Study of microstructure of Zr–Sn–Nb–Fe–Cr alloy in the temperature range of 750–820 °C," *Materials Chemistry and Physics*, vol. 107, pp. 534-540, 2008.

[40] P. Barberis, N. Dupin, C. Lemaignan, A. Pasturel, and J. M. Grange, "Microstructure and Phase Control in Zr-Fe-Cr-Ni Alloys: Thermodynamic and Kinetic Aspects," *Journal of ASTM International*, vol. 2, JAI12771, 2005.

[41] H. G. Weidinger, H. Ruhmann, G. Cheliotis, M. Maguire, and T.-L. Yau, "Corrosion-Electrochemical Properties of Zirconium Intermetallics," in *9th International Symposium on Zr in the Nuclear Industry*, pp. 499-535, 1991.

[42] R. Arroyave, L. Kaufman, and T. W. Eagar, "Thermodynamic modeling of the Zr-O system," *Calphad*, vol. 26, pp. 95-118, 2002.

[43] B. Puchala and A. Van der Ven, "Thermodynamics of the Zr-O system from first-principles calculations," *Physical Review B*, vol. 88, p. 094108, 2013.

[44] B. Paul Burton, A. van de Walle, and H. T. Stokes, "First Principles Phase Diagram Calculations for the Octahedral-Interstitial System ZrOX, $0 \leqslant X \leqslant 1/2$," *Journal of the Physical Society of Japan*, vol. 81, p. 014004, 2011.

[45] H. Anada and K. Takeda, "Microstructure of Oxides on Zircaloy-4, 1.0 Nb Zircaloy-4, and Zircaloy-2 Formed in 10.3 Mpa Steam at 673 K," in *Zirconium in the Nuclear Industry, Eleventh International Symposium*, pp. 35, 1996.

[46] X. Guo, "Hydrothermal degradation mechanism of tetragonal Zirconia," *Journal of Materials Science*, vol. 36, pp. 3737-3744, 2001.

[47] J. Godlewski, "How the Tetragonal Zirconia is Stabilized in the Oxide Scale that is Formed on a Zirconium Alloy Corroded at 400 C in steam," in *10th Int.Symp. on Zr in the Nuclear Industry*, pp. 663-686, 1994.

[48] P. Barberis, "Zirconia Powders and Zircaloy Oxide Film: Tetragonal Phase Evolution During 400 C Autoclave Tests," *Journal of Nuclear Materials*, vol. 226, pp. 34-43, 1995.

[49] R. C. Garvie, "The Occurence of Metastable Tetragonal Zirconia as a Crystalline Size Effect," *The Journal of Physical Chemistry*, vol. 69, pp. 1238-1243, 1965.

[50] R. C. Garvie, "Stabilization of the Tetragonal Structure in Zirconia Microcrystals," *The Journal of Physical Chemistry*, vol. 82, pp. 218-224, 1978.

[51] G. Lucazeau, P. Bouvier, and J. Godlewski, "A Raman study of the nanocrystallite size effect on the pressure-temperature phase diagram of zirconia grown by zirconium-based alloys oxidation," *Journal of Nuclear Materials*, vol. 300, pp. 118-126, 2002.

[52] M. Preuss, P. Frankel, S. Lozano-Perez, D. Hudson, E. Polatidis, N. Ni, *et al.*, "Studies Regarding Corrosion Mechanisms in Zirconium Alloys," *Journal of ASTM International*, vol. 8, JAI103246, 2011.

[53] F. Garzarolli, H. Seidel, R. Tricot, and J. P. Gros, "Oxide Growth Mechanism on Zirconium Alloys," in *9th International Symposium on Zirconium in the Nuclear Industry*, Kobe, Japan, pp. 395-415, 1991.

[54] M. Oskarsson, E. Ahlberg, U. Andersson, and K. Pettersson, "Characterisation of pre-transition oxides on Zircaloys," *Journal of Nuclear Materials*, vol. 297, pp. 77-88, 2001.

[55] J. L. Bechade, R. Dralet, P. Goudeau, and P. Yvon, "Studies of Zirconium alloy oxide layers using synchrotron radiation," *Materials Science Forum*, vol. 347-349, pp. 471-478, 2000.

[56] A. Yilmazbayhan, A. T. Motta, R. J. Comstock, G. P. Sabol, B. Lai, and Z. Cai, "Structure of Zirconium Alloy Oxides formed in pure water studied with Synchrotron radiation and optical microscopy: relation to corrosion rate," *Journal of Nuclear Materials*, vol. 324, pp. 6-22, 2004.

[57] N. Petigny, P. Barberis, C. Lemaignan, C. Valot, and M. Lallemant, "In situ XRD analysis of the oxide layers formed by oxidation at 743 K on Zircaloy-4 and Zr-1NbO," *Journal of Nuclear Materials*, vol. 280, pp. 318-330, 2000.

[58] J. Godlewski, P. Bouvier, G. Lucazeau, and L. Fayette, "Stress distribution measured by Raman spectroscopy in zirconia films formed by oxidation of Zr-based alloys," *ASTM Special Technical Publication*, pp. 877-900, 2000.

[59] H. Arashi and M. Ishigame, "Raman Spectroscopic Studies of the Polymorhism in ZrO2 at High Pressures," *Physical Status Solidi*, vol. A. 71, p. 313, 1982.

[60] S. Davison, R. Kershaw, K. Dwight, and A. Wold, "Preparation and Chracterization of Cubic ZrO_2 Stabilized by Fe(III) and Fe(II)," *Journal of Solid State Chemistry*, vol. 73, pp. 47-51, 1988.

[61] H.-J. Beie, A. Mitwalsky, F. Garzarolli, H. Ruhmann, and H.-J. Sell, "Examinations of the Corosion Mechanism in Zirconium alloys," in *10th International Symposium on Zr in the Nuclear Industry*, Baltimore, pp. 615-643, 1993.

[62] J.-Y. Park, S. J. Yoo, B.-K. Choi, and Y. H. Jeong, "Oxide microstructures of advanced Zr alloys corroded in 360 °C water loop," *Journal of Alloys and Compounds*, vol. 437, pp. 274-279, 2007.

[63] A. Yilmazbayhan, E. Breval, A. Motta, and R. Comstock, "Transmission Electron Microscopy Examination of Oxide Layers Formed in Zr Alloys," *Journal of Nuclear Materials*, vol. 349, pp. 265-281, 2006.

[64] G. P. Sabol, S. G. McDonald, and G. P. Airey, "Microstructure of Oxide Films Formed on Zirconium-Based Alloys," in *Zirconium in Nuclear Applications*, pp. 435, 1974.

[65] B. Wadman, Z. Lai, H. O. Andren, A. L. Nystrom, P. Rudling, and H. Pettersson, "Microstructure of Oxide layers formed during autoclave testing of Zr alloys," in *10th International Symposium on Zr in the Nuclear Industry*, Baltimore, pp. 579-598, 1994.

[66] R. A. Ploc, "Electron diffraction analysis of ZrO2 on α-Zr," *Journal of Nuclear Materials*, vol. 113, pp. 75-80, 1983.

[67] H.-G. Kim, J.-Y. Park, B.-K. Choi, and Y.-H. Jeong, "Evaluation of pre-transition oxide on Zr–0.4 Nb alloy by using the HVEM," *Journal of Nuclear Materials*, vol. 374, pp. 204-210, 2008.

[68] D. Pecheur, J. Godlewski, P. Billot, and J. Thomazet, "Microstructure of Oxide Films formed during the waterside corrosion of the Zircaloy cladding in Lithiated environment," in *11th International Symposium on Zr in the Nuclear Industry*, Garmisch-Partenkirchen, pp. 94-113, 1995.

[69] W. Gong, H. Zhang, Y. Qiao, H. Tian, X. Ni, Z. Li, *et al.*, "Grain morphology and crystal structure of pre-transition oxides formed on Zircaloy-4," *Corrosion Science*, vol. 74, pp. 323-331, 2013.

[70] N. Ni, D. Hudson, J. Wei, P. Wang, S. Lozano-Perez, G. D. W. Smith, "How the crystallography and nanoscale chemistry of the metal/oxide interface develops during

the aqueous oxidation of zirconium cladding alloys," *Acta Materialia,* vol. 60, pp. 7132-7149, 2012.

[71] J. Lin, H. Li, J. A. Szpunar, R. Bordoni, A. M. Olmedo, M. Villegas, "Analysis of zirconium oxide formed during oxidation at 623 K on Zr–2.5Nb and Zircaloy-4," *Materials Science and Engineering: A,* vol. 381, pp. 104-112, 2004.

[72] A. Garner, M. Preuss, and P. Frankel, "A method for accurate texture determination of thin oxide films by glancing-angle laboratory X-ray diffraction," *Journal of Applied Crystallography,* vol. 47, pp. 575-583, 2014.

[73] A. T. Motta, M. J. Gomes-da-Silva, A. Yilmazbayhan, R. J. Comstock, Z. Cai, and B. Lai, "Microstructural Characterization of Oxides Formed on Model Zr Alloys Using Synchrotron Radiation," *Journal of ASTM International,* vol. 5, JAI10125, 2008.

[74] H. Li, M. G. Glavicic, and J. A. Szpunar, "A model of texture formation in ZrO_2 films," *Materials Science and Engineering: A,* vol. 366, pp. 164-174, 2004.

[75] B. Cox, "Processes Occurring During the Breakdown of Oxide Films on Zirconium Alloys," *Journal of Nuclear Materials,* vol. 29, pp. 50-66, 1969.

[76] O. Gebhardt, A. Herman, G. Bart, H. Blank, F. Garzarolli, and L. Ray, "Investigation of In-pile grown corrosion films on zirconium based alloys," in *11th International Symposium on Zr in the Nuclear Industry,* Garmisch-Partenkrichen, pp. 218-241, 1995.

[77] T. Arima, T. Masuzumi, H. Furuya, K. Idemitsu, and Y. Inagaki, "The oxidation kinetics and the structure of the oxide film on Zircaloy before and after the kinetic transition," *Journal of Nuclear Materials,* vol. 294, pp. 148-153, 2001.

[78] B. Hutchinson and B. Lehtinen, "A theory of the resistance of Zircaloy to uniform corrosion," *Journal of Nuclear Materials,* vol. 217, pp. 243-249, 1994.

[79] J. P. Pemsler, "The Kinetics and Mechanism of Oxide Film Growth of Zirconium," *Electrochemical Technology,* vol. 4, pp. 128-131, 1966.

[80] P. T. Moseley and B. Hudson, "Phases involved in the corrosion of zircaloy by hot water (350° C)," *Journal of Nuclear Materials,* vol. 99, pp. 340-344, 1981/09/01 1981.

[81] B. Hutchinson, B. Lehtinen, M. Limbach, and M. Dahlback, "A study of the structure and chemistry in zircaloy-2 and the resulting oxide after high temperature corrosion," *Zirconium in the Nuclear Industry: 15th International Symposium,* STP48141S, pp. 269-284, 2009.

[82] C. Bisor-Melloul, M. Tupin, P.Bossis, J.Chene, J.L.Bechade, and A.T.Motta, "Understanding of Hydriding Mechanisms during Corrosion in PWR Simulated Conditions and Influence of Zirconium Hydrides on Corrosion," *Revue Génerale Nucléaire,* vol. 2, 2011.

[83] P. Bossis, G. Lelievre, P. Barberis, X. Iltis, and F. Lefebvre, "Multi-Scale Characterization of the Metal-Oxide Interface of Zirconium Alloys,," in *Twelfth International Symposium on Zirconium in the Nuclear Industry*, pp. 918, 2000.

[84] M. Y. Yao, B. X. Zhou, Q. Li, W. Q. Liu, X. Geng, and Y. P. Lu, "A superior corrosion behavior of Zircaloy-4 in lithiated water at 360 °C and18.6MPa by β-quenching," *Journal of Nuclear Materials*, vol. 374, pp. 197-203, 2008.

[85] G. Wikmark, P. Rudling, B. Lehtinen, B. Hutchinson, A. Oscarsson, and E. Ahlberg, "The Importance of Oxide Morphology for the Oxidation Rate of Zirconium Alloys," *Zirconium in the Nuclear Industry: Eleventh International Symposium*, West Conshohocken, STP16167S, pp. 55-73, 1996.

[86] Y. H. Jeong, J. H. Baek, S. J. Kim, H. G. Kim, and H. Ruhmann, "Corrosion characteristics and oxide microstructures of Zircaloy-4 in aqueous alkali hydroxide solutions," *Journal of Nuclear Materials*, vol. 270, pp. 322-333, 1999.

[87] Y. Ding and D. O. Northwood, "A study of the interphase structure at the oxide-metal interface in the corrosion of zirconium-based alloys," *Corrosion Science*, vol. 36, pp. 259-282, 1994.

[88] P. Rudling, M. Mikes-Lindbäck, B. Lethinen, H. Andrén, and K. Stiller, "Corrosion Performance of New Zircaloy-2-Based Alloys," *Zirconium in the Nuclear Industry: Tenth International Symposium*, STP15211S, pp. 599-614, 1994.

[89] H. Anada, B. J. Herb, K. Nomoto, S. Hagi, R. A. Graham, and T. Kuroda, "Effect of Annealing Temperature on Corrosion Behavior and ZrO_2 microstructure of Zircaloy-4 Cladding tube," in *11th ASTM Symposium on Zr in the Nuclear Industry*, pp. 74-93, 1996.

[90] T. Kubo, "Irradiation growth in zirconium alloys under high fluences," *Res Mechanica*, vol. 29, pp. 289-312, 1990.

[91] D. Pecheur, "Oxidation of B-Nb and $Zr(Fe,V)_2$ precipitates in oxide films formed on advanced Zr-based alloys," *Journal of Nuclear Materials*, vol. 278, pp. 195-201, 2000.

[92] D. Pecheur, F. Lefebvre, A. T. Motta, C. Lemaignan, and D. Charquet, "Oxidation of Intermetallic Precipitates in Zircaloy-4: Impact of Irradiation," in *10th International Symposium on Zirconium in the Nuclear Industry*, pp. 687-705, 1994.

[93] D. Pecheur, F. Lefebvre, A. T. Motta, C. Lemaignan, and J.-F. Wadier, "Precipitate Evolution in the Zircaloy-4 Oxide Layer," *Journal of Nuclear Materials*, vol. 189, pp. 2318-2332, 1992.

[94] J. H. Baek and Y. H. Jeong, "Depletion of Fe and Cr within Precipitates During Zircaloy-4 Oxidation," *Journal of Nuclear Materials*, vol. 304, pp. 107-116, 2002.

[95] B. Cox and H. I. Sheikh, "Redistribution of the Alloying Elements during Zircaloy-2 Oxidation," *Journal of Nuclear Materials*, vol. 249, pp. 17-32, 1997.

[96] P. B. Bozzano, C. Ramos, F. Saporiti, P. A. Vázquez, R. A. Versaci, and C. Saragovi, "Oxidation of the hexagonal $Zr(Cr_{0.4}Fe_{0.6})_2$ Laves phase," *Journal of Nuclear Materials*, vol. 328, pp. 225-231, 2004.

[97] Y. Hatano and M. Sugisaki, "Auger Electron Spectroscopy Study of Oxidation Behavior of Iron and Chromium in $Zr(Fe,Cr)_2$ Precipitate in Zircaloy-4," *Journal of Nuclear Science and Technology,* vol. 34, pp. 264-268, 1997.

[98] C. Li, R. Zuo, Z. Li, S. Ying, and B. Shen, "Transmission electron microscopy investigation of $Zr_2(Fe,Ni)$ particles incorporated in the oxide film formed on a Zirconium alloy," *Thin Solid Films,* vol. 461, pp. 272-276, 2004.

[99] Y. Hatano and M. Sugisaki, "Oxidation Behavior of Iron and Nickel in $Zr_2(Fe, Ni)$ Precipitates in Zircaloy-2," *Journal of Nuclear Science and Technology,* vol. 33, pp. 829-833, 1996.

[100] Y. P. Lin and O. T. Woo, "Oxidation of beta-Zr and related phases in Zr-Nb alloys: an electron microscopy investigation," *Journal of Nuclear Materials,* vol. 277, pp. 11-27, 2000.

[101] P. Bossis, J. Thomazet, and F. Lefebvre, "Study of Mechanisms Controlling the Oxide Growth Under Irradiation: Characterization of Irradiated Zircaloy-4 and Zr-1Nb-O Oxide Scales," in *Zirconium in the Nuclear Industry: Thirteenth International Symposium*, pp. 190-221, 2001.

[102] C. Lemaignan, "Corrosion of Zirconium Alloy Components in Light Water Reactors," *ASM Handbook,* 2006.

[103] D. Franklin, "Zirconium Alloy Corrosion: A Review based on an International Atomic Energy Agency Meeting," in *9th International Symposium on Zr in the Nuclear Industry,* pp. 3-32, 1993.

[104] R. J. Hussey and W. W. Smeltzer, "The Oxidation Kinetics of Zirconium in the Temperature Range 400-600 ^{o}C," *Journal of Electrochemical Society,* vol. 111, pp. 564-568, 1965.

[105] H. A. Porte, J. G. Schnizlein, R. C. Vogel, and D. F. Fischer, "Oxidation of Zirconium and Zirconium Alloys," *Journal of the Electrochemical Society,* vol. 107, pp. 506-515, 1960.

[106] J. K. Dawson, G. Long, W. E. Seddon, and J. F. White, "The Kinetics and Mechanism of the Oxidation of Zircaloy-2 at 350-500 °C," *Journal of Nuclear Materials,* vol. 25, pp. 179-200, 1968.

[107] W. W. Smeltzer, R. R. Haering, and J. S. Kirkaldy, "Oxidation of metals by short circuit and lattice diffusion of oxygen," *Acta Metallurgica,* vol. 9, pp. 880-885, 1961.

[108] H. I. Yoo, B. J. Koo, J. O. Hong, I. S. Hwang, and Y. H. Jeong, "A working hypothesis on oxidation kinetics of Zircaloy," *Journal of Nuclear Materials,* vol. 299, pp. 235-241, 2001.

[109] M. Tupin, M. Pijolat, F. Valdivieso, M. Soustelle, A. Frichet, and P. Barberis, "Differences in reactivity of oxide growth during the oxidation of Zircaloy-4 in water

vapour before and after the kinetic transition," *Journal of Nuclear Materials,* vol. 317, pp. 130-144, 2003.

[110] E. A. García, "Dynamical diffusion model to simulate the oxide crystallization and grain growth during oxidation of zirconium at 573 and 623 K," *Journal of Nuclear Materials,* vol. 224, pp. 299-304, 1995.

[111] E. A. García and J. Kovacs, "Diffusion model for the oxidation of zirconium at 573 and 623 K," *Journal of Nuclear Materials,* vol. 210, pp. 78-83, 1994.

[112] G. P. Sabol and S. B. Dalgaard, "The Origin of the Cubic Rate law in Zirconium Alloy Oxidation," *Journal of the Electrochemical Society,* vol. 122, p. 316, 1975.

[113] F. Nagase, T. Otomo, and H. Uetsuka, "Oxidation Kinetics of Low-Sn Zircaloy-4 at the Temperature Range from 773 to 1,573K," *Journal of Nuclear Science and Technology,* vol. 40, pp. 213-219, 2003.

[114] A. J. G. Maroto, R. Bordoni, M. Villegas, A. M. Olmedo, M. A. Blesa, A. Iglesias, *et al.*, "Growth and characterization of oxide layers on zirconium alloys," *Journal of Nuclear Materials,* vol. 229, pp. 79-92, 1996.

[115] G. P. Sabol, R. J. Comstock, R. A. Weiner, P. Larouere, and R. N. Stanutz, "In-Reactor Corrosion Performance of ZIRLO and Zircaloy-4," in *10th ASTM International Symposium on Zr in the Nuclear Industry*, Baltimore, pp. 724-744, 1994.

[116] B. Griggs, H. P. Maffei, and D. W. Shannon, "Multiple Rate Transitions in the Aqueous Corrosion of Zircaloy," *Journal of the Electrochemical Society,* vol. 109, pp. 665-668, 1962.

[117] J. S. Bryner, "The Cyclic Nature of Corrosion of Zircaloy-4 in 633 K Water," *Journal of Nuclear Materials,* vol. 82, pp. 84-101, 1979.

[118] G. P. Sabol, G. R. Kilp, M. G. Balfour, and E. Roberts, "Development of a Cladding Alloy for High Burnup," in *Eighth International Symposium on Zirconium in the Nuclear Industry*, San Diego, pp. 227-244, 1989.

[119] A. V. Nikulina, "Zirconium-niobium alloys for core elements of pressurized water reactors," *Metallurgy Science and Heat Treatment* vol. 1467, pp. 287-292, 2003.

[120] A. V. Nikulina, et. al., "Zirconium Alloy E635 as a Material for Fuel Rod Cladding and Other Components of VVER and RBMK Cores,, *Zirconium in the Nuclear Industry: Eleventh International Symposium*, STP16201S, pp. 785-804, 1996.

[121] J. H. Baek, K. B. Park, and Y. H. Jeong, "Oxidation kinetics of Zircaloy-4 and Zr–1Nb–1Sn–0.1Fe at temperatures of 700-1200°C," *Journal of Nuclear Materials,* vol. 335, pp. 443-456, 2004.

[122] J.-Y. Park, B.-K. Choi, S. J. Yoo, and Y. H. Jeong, "Corrosion behavior and oxide properties of Zr–1.1wt. %-0.05wt.%Cu Alloy," *Journal of Nuclear Materials,* vol. 359, pp. 59-68, 2006.

[123] J. H. Baek and Y. H. Jeong, "Steam oxidation of Zr–1.5Nb–0.4Sn–0.2Fe–0.1Cr and Zircaloy-4 at 900–1200 °C," *Journal of Nuclear Materials,* vol. 361, pp. 30-40, 2007.
[124] D. H. Bradhurst and P. M. Heuer, "The Influence of Oxide Stress on the Breakaway oxidation of Zircaloy-2," *Journal of Nuclear Materials,* vol. 37, p. 35-47, 1970.
[125] D. H. Bradhurst and P. M. Heuer, "Reply to Comments by B. Cox on "The Influence of Oxide Stress on the Breakaway Oxidation of Zircaloy-2", *Journal of Nuclear Materials*, vol. 41, pp. 101-105, 1971.
[126] B. Cox, "Comments on the Paper 'The Influence of Oxide Stress on the Breakaway Oxidation of Zircaloy-2' by D. H. Bradhurst and P. M. Heuer," *Journal of Nuclear Materials*, vol. 41, pp. 96-100, 1971.
[127] J. R. Moon and D. G. Lee, "Cracking in oxides on Zr alloys," *Corrosion Science,* vol. 10, pp. 85-89, 1970.
[128] B. Cox, "Pore Structure in Oxide Films on Irradiated and Unirradiated Zirconium Alloys," *Journal of Nuclear Materials,* vol. 148, pp. 332-343, 1987.
[129] B. Cox and Y. Yamaguchi, "The Development of Porosity in Thick Zirconia Films," *Journal of Nuclear Materials*, vol. 210, pp. 303-317, 1994.
[130] P. Bossis, F. Lefebvre, P. Barberis, and A. Galerie, "Corrosion of Zirconium Alloys: Link Between the Metal/Oxide Interface Roughness, the Degradation of the Protective Oxide Layer and the Corrosion Kinetics," *Materials Science Forum,* vol. 369-372, pp. 255-262, 2001.
[131] J. Lin, H. Li, C. Nam, and J. A. Szpunar, "Analysis on volume fraction and crystal orientation relationship of monoclinic and tetragonal oxide grown on Zr–2.5Nb alloy," *Journal of Nuclear Materials*, vol. 334, pp. 200-206, 2004.
[132] M. G. Glavicic, J. A. Szpunar, and Y. P. Lin, "A method for the quantitative phase analysis of ZrO2 films grown on Zr-2.5% Nb pressure tubes," *Journal of Nuclear Materials*, vol. 245, pp. 147-151, 1997.
[133] S. Abolhassani, R. Restani, T. Reback, F. Groeschel, W. Hofflener, G. Bart, *et al.*, "TEM examinations of the Metal-Oxide Interface of Zirconium Based Alloys Irradiated in a Pressurized Water reactor," *Journal of ASTM International,* Vol. 2, pp. 1-25, 2005.
[134] J. Hu, A. Garner, N. Ni, A. Gholinia, R. Nicholls, S. Lozano-Perez, *et al.*, "Identifying suboxide grains at the metal–oxide interface of a corroded Zr–1.0%Nb alloy using (S)TEM, transmission-EBSD and EELS," *Micron,* vol. 69, pp. 35-42, 2015.
[135] B. de Gabory, A. T. Motta, and K. Wang, "Transmission electron microscopy characterization of Zircaloy-4 and ZIRLO™ oxide layers," *Journal of Nuclear Materials*, vol. 456, pp. 272-280, 2015.
[136] F. Garzarolli and R. Holzer, "Waterside Corrosion Performance of Light Water Power reactor Fuel," *Journal of the British Nuclear Society,* vol. 31, pp. 65-85, 1992.

[137] F. Garzarolli, Y. Broy, and R. A. Buch, "Comparison of the long-time Corrosion Behavior of Certain Zr-Alloys in PWR, BWR and Laboratory Tests," *Zirconium in the Nuclear Industry: Eleventh International Symposium*, pp. 850-864, 1995.

[138] L. F. P. V. Swam and S. H. Shann, "The Corrosion of Zircaloy-4 Fuel Cladding in Pressurized Water Reactor," *Zirconium in the Nuclear Industry, Eleventh International Symposium*, pp. 8550-8864, 1995.

[139] J. P. Mardon, D. Charquet, and J. Senevat, "Optimization of PWR behavior of Stress-relieved Zircaloy-4 Cladding Tubes by Imporving the Manufacturing and Inspection Process," *Zirconium in the Nuclear Industry, Tenth International Symposium*, pp. 328-346, 1994.

[140] P. Tejland, "Microstructure Investigation of the Oxidation Process in Zircaloy-2 -The Effect of Intermetallic Particle Size," Doctor of Philosophy, Department of Applied Physics, Chalmers University of Technology, Sweden, 2012.

[141] P. Tejland, M. Thuvander, Andr, eacute, H. n, S. Ciurea, "Detailed Analysis of the Microstructure of the Metal/Oxide Interface Region in Zircaloy-2 after Autoclave Corrosion Testing," *Journal of ASTM International*, Vol. 8, pp. 1-16, 2011.

[142] P. Tejland, H.-O. Andrén, G. Sundell, M. Thuvander, B. Josefsson, L. Hallstadius, "Oxidation mechanism in Zircaloy-2 - the effect of SPP size distribution," *Zirconium in the Nuclear Industry: 17th International Symposium*, STP154320130052, pp. 373-403, 2014.

[143] C. T. Wang, C. M. Eucken, and R. A. Graham, "Investigation of Nodular Corrosion Mechanism for Zircaloy Products," *Zirconium in the Nuclear Industry: 9th International Symposium*, pp. 319-345, 1991.

[144] B. Cheng and R. B. Adamson, "Mechanistic Studies of Zircaloy Nodular Corrsion," in *Zirconium in the Nuclear Industry: 7th International Symposium*, pp. 387-416, 1987.

[145] Y. H. Jeong, K. S. Rheem, C. S. Choi, and Y. S. Kim, "Effect of Beta Heat Treatment on Microstructure and Nodular Corrosion of Zircaloy-4," *Journal of Nuclear Science and Technology*, vol. 30, pp. 154-163, 1993.

[146] P. J. Shirvington, "A mechanism for in-reactor oxidation of zirconium alloys from oxide electrical characteristics," *Journal of Nuclear Materials*, vol. 52, pp. 13-23, 1974.

[147] K. Takeda and H. Anada, "Mechanism of Corrosion Degradation in Sn," in *12th International Symposium on Zr in the Nuclear Industry*, pp. 592-608, 2000.

[148] J. Wei, P. Frankel, E. Polatidis, M. Blat, A. Ambard, R. J. Comstock, *et al.*, "The effect of Sn on autoclave corrosion performance and corrosion mechanisms in Zr–Sn–Nb alloys," *Acta Materialia*, vol. 61, pp. 4200-4214, 2013.

[149] A. Garner, J. Hu, A. Harte, P. Frankel, C. Grovenor, S. Lozano-Perez, *et al.*, "The effect of Sn concentration on oxide texture and microstructure formation in zirconium alloys," *Acta Materialia*, vol. 99, pp. 259-272, 2015.
[150] J. H. Harding, "The effect of alloying elements on Zircaloy corrosion," *Journal of Nuclear Materials*, vol. 202, pp. 216-221, 1993.
[151] D. Charquet, "Improvement of the Uniform Corrosion Resistance of Zircaloy-4 in the Absense of Irradiation," *Journal of Nuclear Materials*, vol. 160, pp. 186-195, 1988.
[152] S. L. Wadekar, "Correlation of Microstructure and Mechanical Properties of Zr-Sn Alloys," *Zirconium in the Nuclear Industry: Ninth International Symposium*, pp. 140-154, 1990.
[153] H. J. Sell, S. Trapp-Pritsching, and F. Garzarolli, "Effects of Alloying Elements and Impurities on in-BWR Corrosion of Zirconium Alloys," *Zirconium in the Nuclear Industry: Fourteenth International Symposium*, pp. 1-14, 2004.
[154] D. Pecheur, V. P. Filippov, A. B. Bateev, and J. J. Ivanov, "Mossbauer Investigations of the Chemical States of Tin and Iron Atoms in Zirconium Alloy Oxide Film," in *13th ASTM Symposium on Zr in the Nuclear Industry*, pp. 135-153, 2002.
[155] K. Takeda and H. Anada, "Mechanism of Corrosion Degradation due to Tin," presented at the 12th International Symposium: Zirconium in Nuclear Industry, 2000.
[156] D. Foord, "The microstructural characterisation of factors which determine the degradation behaviour of Zircaloy-4," in *Microscopy of Oxidation-3*, pp. 488-499, 1997.
[157] H. Anada, K. Takeda, S. Nasu, Y. Kobayashi, and T. Nakamichi, "Chemical State Analysis of Sn and Fe in ZrO2 by Mossbauer Spectroscopy," in *13th International Symposium on Zr in the Nuclear Industry*, Annecy, pp. 154-168, 2002.
[158] G. Sundell, M. Thuvander, and H. O. Andrén, "Tin clustering and precipitation in the oxide during autoclave corrosion of Zircaloy-2," *Journal of Nuclear Materials*, vol. 456, pp. 409-414, 2015.
[159] R. Borrelly, P. Merle, and L. Adami, "Study of the Solubility of Iron in Zirconium by Thermoelectric Power Measurements," *Journal of Nuclear Materials*, vol. 170, pp. 147-156, 1990.
[160] C. Li, B. Zhou, W. Zhao, P. Li, and Q. Peng, "Determination of Fe and Cr Content in α-Zr Solid Solution of Zircaloy-4 with Heat-Treated States," *Journal of Nuclear Materials*, vol. 304, pp. 134-138, 2002.
[161] A. Yilmazbayhan, O. Delaire, A. T. Motta, R. C. Birtcher, J. M. Maser, and B. Lai, "Determination of the alloying content in the matrix of Zr alloys using synchrotron radiation microprobe X-ray fluorescence," *Journal of Nuclear Materials*, vol. 21, pp. 221-232, 2003.

[162] D. Hudson, "Zirconium Oxidation on the Atomic Scale," Ph.D., Department of Materials, University of Oxford, 2010.
[163] D. Hudson and G. D. W. Smith, " Initial observation of grain boundary solute segregation in a zirconium alloy (ZIRLO) by three-dimensional atom probe," *Scripta Materialia* vol. 61, pp. 411-414, 2009.
[164] G. Sundell, M. Thuvander, and H. O. Andrén, "Enrichment of Fe and Ni at metal and oxide grain boundaries in corroded Zircaloy-2," *Corrosion Science,* vol. 65, pp. 10-12, 2012.
[165] H. Li, H. M. Glavicic, and J. A. Spuznar, "A Model of Texture formation in ZrO_2 Films," *Materials Science and Engineering,* vol. A366, pp. 164-174, 2004.
[166] A. Garner, A. Gholinia, P. Frankel, M. Gass, I. MacLaren, and M. Preuss, "The microstructure and microtexture of zirconium oxide films studied by transmission electron backscatter diffraction and automated crystal orientation mapping with transmission electron microscopy," *Acta Materialia,* vol. 80, pp. 159-171, 2014.
[167] N. Ni, S. Lozano-Perez, J. Sykes, and C. Grovenor, "Quantitative EELS analysis of zirconium alloy metal/oxide interfaces," *Ultramicroscopy,* vol. 111, pp. 123-130, 2011.
[168] P. Tejland, H.-O. Andrén, G. Sundell, M. Thuvander, B. Josefsson, L. Hallstadius, "Oxidation mechanism in Zircaloy-2 - the effect of SPP size distribution," *Zirconium in the Nuclear Industry: 17th International Symposium,* pp. 373-403, 2014.
[169] A. T. Motta, M. J. G. Da Silva, A. Yilmazbayhan, R. J. Comstock, Z. Cai, and B. Lai, "Microstructural characterization of oxides formed on model Zr alloys using synchrotron radiation," Journal of ASTM International, Vol. 5, pp.1-20, 2008.
[170] A. Yilmazbayhan, "Microstructural Basis of Uniform Corrosion in Zr Alloys," Ph.D., Nuclear Engineering, Penn State University, 2004.
[171] A. Yilmazbayhan, A. T. Motta, H.G.Kim, Y. H. Jeong, J. Y. Park, and R. Comstock, "Characterization of oxides formed on model Zr alloys in 360 °C water using synchrotron radiation," in *12th International Conference on Environmental Degradation of Materials in Nuclear Power Systems -Water Reactors*, Snowbird, Utah, pp. 201-210, 2005.
[172] M. J. G. d. Silva, "Influence of Oxide Microstructure on Corrosion Behavior of Zirconium-based Model Alloys," Doctor of Philosophy, Department of Mechanical and Nuclear Engineering, The Pennsylvania State University, 2007.
[173] N. Yao, "Introduction to the focused ion beam system," in *Focused Ion Beam Systems: Basics and Applications*, Cambridge University Press, pp. 1-30, 2007.
[174] L. A. Giannuzzi and F. A. Stevie, "A review of focused ion beam milling techniques for TEM specimen preparation," *Micron,* vol. 30, pp. 197-204, 1999.

[175] K. Thompson, D. Lawrence, D. J. Larson, J. D. Olson, T. F. Kelly, and B. Gorman, "In situ site-specific specimen preparation for atom probe tomography," *Ultramicroscopy,* vol. 107, pp. 131-139, 2007.
[176] J. B. Bindell, "Scanning Electron Microscopy," in *Encyclopedia of Materials Chracterization*, Boston: Manning Publications Co., pp. 70-84, 1992.
[177] J. I. Goldstein, D. E. Newbury, P. Echlin, D. C. Joy, C. E. Lyman, E. Lifshin, *et al.*, "The SEM and Its Modes of Operation," in *Scanning Electron Microscopy and X-ray Microanalysis: Third Edition*, ed Boston, MA: Springer US, pp. 21-60, 2003.
[178] T. F. Kelly and M. K. Miller, "Atom probe tomography," *Review of Scientific Instruments,* vol. 78, pp. 031101, 2007.
[179] D. N. Seidman and K. Stiller, "An Atom-Probe Tomography Primer," *MRS Bulletin,* vol. 34, pp. 717-724, 2009.
[180] E. A. Marquis and J. M. Hyde, "Applications of atom-probe tomography to the characterisation of solute behaviours," *Materials Science and Engineering: R: Reports,* vol. 69, pp. 37-62, 2010.
[181] E. W. Müller, "Field Desorption," *Physical Review,* vol. 102, pp. 618-624, 1956.
[182] M. K. Miller, *Atom Probe Field Ion Microscopy*. Oxford: Oxford University Press, 1996.
[183] B. Gault, F. Danoix, K. Hoummada, D. Mangelinck, and H. Leitner, "Impact of directional walk on atom probe microanalysis," *Ultramicroscopy,* vol. 113, pp. 182-191, 2012.
[184] D. R. Kingham, "The post-ionization of field evaporated ions: A theoretical explanation of multiple charge states," *Surface Science,* vol. 116, pp. 273-301, 1982.
[185] B. P. Geiser, T. F. Kelly, D. J. Larson, J. Schneir, and J. P. Roberts, "Spatial Distribution Maps for Atom Probe Tomography," *Microscopy and Microanalysis,* vol. 13, pp. 437-447, 2007.
[186] B. Gault, M. P. Moody, J. M. Cairney, and S. P. Ringer, "Atom probe crystallography," *Materials Today,* vol. 15, pp. 378-386, 2012.
[187] D. Charquet, R. Hahn, E. Ortlieb, J.-P. Gros, and J.-F. Wadier, "Solubility Limits and Formation of Intermetallic Precilitates in ZrSnFeCr Alloys," in *Zirconium in the Nuclear Industry: 8th International Symposium,* pp. 405-422, 1989.
[188] D. Charquet and E. Alheritiere, "Second Phase Particles and Matrix Properties on Zircaloys," in *Workshop on Second-Phase particles in Zircaloy*, Erlangen, Germany, pp. 5-11, 1985.
[189] J. Godlewski, J. P. Gros, M. Lambertin, J. F. Wadier, and H. Weidinger, "Raman Spectroscopy Study of the Tetragonal-to-Monoclinic transition in Zirconium oxide scales and determination of overall oxygen diffusion by nuclear microanalysis of ^{18}O," in *9th International Symposium on Zr in the Nuclear Industry*, pp. 416-436, 1991.

[190] N. B. Pilling and R. E. Bedworth, "The Oxidation of Metals at High Temperatures," *Journal of International Metals,* vol. 29, pp. 529-591, 1923.
[191] H. G. Kim, T. H. Kim, and Y. H. Jeong, "Oxidation characteristics of basal plane and prism plane in HCP Zr," *Journal of Nuclear Materials,* vol. 306, pp. 44-53, 2002.
[192] D. Pecheur, V. Filippov, A. B. Bateev, and J. J. Ivanov, "Mossbauer Investigations of the Chemical States of Sn and Fe Atoms in Zirconium Alloy Oxide Film," in *13th ASTM International Symposium on Zr in the Nuclear Industry*, pp. 135-153, 2003.
[193] O. C. Hellman and D. N. Seidman, "Measurement of the Gibbsian interfacial excess of solute at an interface of arbitrary geometry using three-dimensional atom probe microscopy," *Materials Science and Engineering A,* vol. 327, pp. 24-28, 2002.
[194] M. Christensen, T. M. Angeliu, J. D. Ballard, J. Vollmer, R. Najafabadi, and E. Wimmer, "Effect of impurity and alloying elements on Zr grain boundary strength from first-principles computations," *Journal of Nuclear Materials,* vol. 404, pp. 121-127, 2010.
[195] G. M. Hood, "Point Defect Diffusion in alpha-Zr," *Journal of Nuclear Materials,* vol. 159, pp. 149-175, 1988.
[196] G. M. Hood and R. J. Schultz, "Diffusion of 3D Transition Elements in α-Zr and Zirconium Alloys," in *Zirconium in the Nuclear Industry: 8th International Symposium,* pp. 435-450, 1989.
[197] B. M. Pande, M. C. Naik, and R. P. Agarwala, "Diffusion of chromium and iron in Zircaloy-2," *Journal of Nuclear Materials,* vol. 28, pp. 324-332, 1968.